STRUCTURAL ASSESSMENT OF ENDODONTIC INSTRUMENTS

by

Eyüp Can Kökan

B.S., Mechanical Engineer, Istanbul Technical University, 2011

M.S., Computational Mechanics, Technical University of Munich, 2013

Submitted to the Institute for Graduate Studies in
Science and Engineering in partial fulfillment of
the requirements for the degree of
Doctor of Philosophy

Graduate Program in Mechanical Engineering

Boğaziçi University

2024

ACKNOWLEDGEMENTS

I would like to express my deepest gratitude to my thesis supervisor, Prof. Şebnem Özüpek, whose guidance, support, and insightful feedback have been invaluable throughout the course of this research. Her expertise and dedication have significantly contributed to the successful completion of this thesis.

I am also profoundly grateful to my thesis co-supervisor, Dr. Evgeny Podnos, for his continuous encouragement and insightful suggestions. His knowledge and experience have been instrumental in shaping the direction and outcome of this study.

Special thanks go to Prof. Nuri Ersoy for his fruitful discussions on the fatigue behavior of NiTi materials and general FEA aspects. His input has greatly enhanced the depth and quality of this research.

I am particularly indebted to Prof. Raif Erişen, who not only conceived the idea for this study but also provided valuable information on root canal treatment methods, and critical insights into the flaws of current instruments and techniques. His contributions have been foundational to the practical aspects of this research.

My sincere appreciation goes to Asst. Prof. Turgut Yağmur Yalçın, who facilitated the acquisition of the required 3D models of endodontic files and molar tooth. His support has been crucial in the development of the simulation models used in this research.

I would like to thank Dr. Alper Can Topuz for his valuable perspectives on endodontic treatment and current methodologies. His practical insights have greatly enriched this work.

Finally, I am deeply thankful to my parents and my fiancée, Mine Karakaya, for their unwavering support and encouragement throughout this journey. Their love and understanding have been my foundation and motivation during the challenging times of my research.

Thank you all for your invaluable contributions and support.

ABSTRACT

STRUCTURAL ASSESSMENT OF ENDODONTIC INSTRUMENTS

This thesis presents a comprehensive computational methodology based on Finite Element Analysis (FEA) for the structural assessment of rotary endodontic files made from conventional austenitic NiTi alloys. The primary objective is to understand and accurately capture the mechanical behavior and failure modes of these instruments under various operational conditions. The study focuses on the torsional and bending stiffness characteristics of endodontic files and their fatigue behavior during root canal procedures.

Methodology development involved simulating bending and torsional tests as per ISO 3630-1 standards, as well as cyclic fatigue tests using a selected simulated canal configuration. The root canal treatment procedure was also simulated for a molar tooth with significant root canal curvature to understand the influence of a realistic canal geometry on the fatigue behavior of endodontic files. Utilization of the dissipated energy method for fatigue life estimation of NiTi endodontic files is one of the contributions of this work.

The ProTaper Universal file set was chosen for methodology development due to the availability of extensive data. The endodontic files and molar tooth geometries were acquired through three dimensional scanning, and geometry data for physical tests were retrieved from the literature. The study showed reasonable correlation between simulation results and physical test data for ISO 3630-1 and cyclic fatigue simulations. Pecking and reciprocating motions were found to increase the fatigue life of endodontic files.

ÖZET

DÖNER KANAL ALETLERİNİN YAPISAL DEĞERLENDİRMESİ

Bu çalışma kapsamında geleneksel östenitik NiTi alaşımlarından yapılmış döner endodontik eğelerin yapısal değerlendirmesi için bir hesaplama yöntemi geliştirilmiştir. Ana hedef, bu aletlerin çeşitli kullanım koşulları altında mekanik davranışını ve arıza davranışlarını anlamak ve doğru bir şekilde temsil etmektir. Çalışma, endodontik eğelerin burulma ve eğilme özelliklerine ve kanal tedavisine bağlı yorulma davranışlarına odaklanmaktadır.

Geliştirilen yöntem, ISO 3630-1 standartlarına uygun olarak eğilme ve burulma testlerinin yanı sıra, bir yapay diş kökü kanalı düzeneği kullanarak yorulma testlerinin benzetimini içermektedir. Ayrıca, gerçekçi bir kanal geometrisinin endodontik eğelerin yorulma davranışı üzerindeki etkisini anlamak amacıyla, diş kökü kanal eğriliği yüksek olan bir azı dişi için de kanal tedavisi benzetimi yapılmıştır. NiTi endodontik eğelerin yorulma ömrünün tahmininde, yüklemeye bağlı enerji kaybının kullanımı, bu çalışmanın katkılarından biridir.

Geliştirilen hesaplamalı yöntemde yaygın kullanımı ve literatürde yer alan test verilerinin uygunluğu nedeniyle ProTaper Universal eğe seti seçilmiştir. Endodontik eğeler ve azı dişi geometrileri üç boyutlu tarama ile elde edilmiş olup, fiziksel testlerin geometri verileri literatürden alınmıştır. Çalışmada, ISO 3630-1 ve döngüsel yüklemeler için benzetim sonuçları ile fiziksel test verileri arasında kabul edilebilir bir korelasyon gözlemlenmiştir. Ayrıca fırçalama ve resiprokal hareketlerinin endodontik eğelerin yorulma ömrünü artırdığı saptanmıştır.

TABLE OF CONTENTS

LIST OF FIGURES

LIST OF TABLES

LIST OF SYMBOLS

A_F^0	Temperature at the end of reverse martensitic transformation at zero stress
A_S^0	Temperature at the beginning of reverse martensitic transformation at zero stress
C^{AS}	Slope of the stress-temperature line for austenite to single-variant martensite transformation
C^{SA}	Slope of the stress-temperature line for single-variant martensite to austenite transformation
F^{AS}	Function describing austenite to single-variant martensite transformation
F^{SA}	Function describing single-variant martensite to austenite transformation
F^{SS}	Function describing single-variant martensite reorientation
F_f^{AS}	Final transformation function for austenite to single-variant martensite
F_f^{SA}	Final transformation function for single-variant martensite to austenite
F_s^{AS}	Initial transformation function for austenite to single-variant martensite
F_s^{SA}	Initial transformation function for single-variant martensite to austenite
F_s^{SS}	Initial transformation function for single-variant martensite reorientation
H^{AS}	Phase transformation activation condition for austenite to single-variant martensite

H^{SA}	Phase transformation activation condition for single-variant martensite to austenite
H^{SS}	Phase transformation activation condition for single-variant martensite reorientation
M_F^0	Temperature at the end of forward martensitic transformation at zero stress
M_S^0	Temperature at the beginning of forward martensitic transformation at zero stress
R_f^{AS}	Final transformation stress for austenite to single-variant martensite transformation
R_f^{SA}	Final transformation stress for single-variant martensite to austenite transformation
R_s^{AS}	Initial transformation stress for austenite to single-variant martensite transformation
R_s^{SA}	Initial transformation stress for single-variant martensite to austenite transformation
R_s^{SS}	Initial transformation stress for single-variant martensite reorientation
T	Temperature
T_f^{AS}	Final temperature for austenite to single-variant martensite transformation at zero stress
T_s^{AS}	Initial temperature for austenite to single-variant martensite transformation at zero stress
$\boldsymbol{u}$	Scaled transformation strain
$\mathbf{M}^{AS}$	Transformation direction tensor for austenite to single-variant martensite
$\mathbf{M}^{SS}$	Transformation direction tensor for single-variant martensite reorientation

$\mathbf{N}^{AS}$	Normalized transformation direction for austenite to single-variant martensite
$\mathbf{N}^{SA}$	Normalized transformation direction for single-variant martensite to austenite
$\mathbf{N}^{SS}$	Normalized transformation direction for single-variant martensite reorientation
$\dot{\boldsymbol{u}}^{AS}$	Rate of scaled transformation strain for austenite to single-variant martensite
$\dot{\boldsymbol{u}}^{SA}$	Rate of scaled transformation strain for single-variant martensite to austenite
$\dot{\boldsymbol{u}}^{SS}$	Rate of scaled transformation strain for single-variant martensite reorientation
$\dot{\xi}_S^{AS}$	Rate of single-variant martensite formation
$\dot{\xi}_S^{SA}$	Rate of single-variant martensite to austenite transformation
ϵ	Total strain
ϵ^e	Elastic strain
ϵ_L	Maximum residual strain
$\boldsymbol{\epsilon}$	Total strain in the three-dimensional state
$\boldsymbol{\epsilon}^{tr}$	Transformation strain
σ	Uniaxial stress
$\boldsymbol{\tau}$	Stress in the three-dimensional state
ξ_A	Austenite fraction
ξ_S	Single-variant martensite fraction

LIST OF ACRONYMS/ABBREVIATIONS

3D	Three Dimensional
BMP	Bitmap
FEA	Finite Element Analysis
ISO	International Organization for Standardization
MicroCT	Micro Computed Tomography
NiTi	Nickel-Titanium
PDL	Periodontal Ligament
SMA	Shape Memory Alloy
STL	Stereolithography
TIFF	Tagged Image File Format

1. INTRODUCTION

1.1. Problem Definition

Root canal treatment is a procedure used when the inside of the tooth is infected. Tooth anatomy consists of different parts such as bone like structures, blood vessels, canals and ligaments as seen in Figure 1.1.

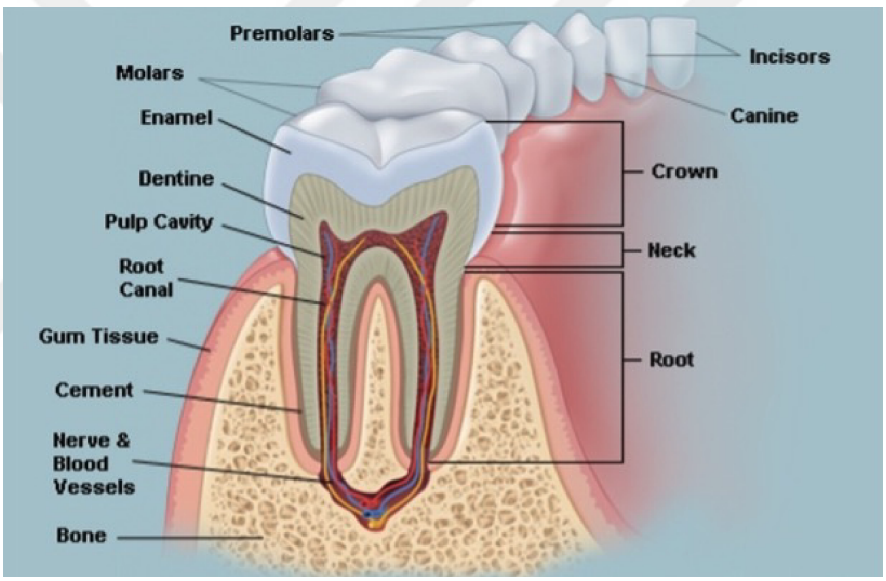

Figure 1.1. Anatomy of teeth [1].

Root canal treatment starts with removing part of the tooth crown and accessing the root canal. After that infected pulp and nerve in the root of the tooth are removed and replaced with gutta-percha and adhesive cement. Lastly crown is replaced with a biocompatible material to restore the tooth's function.

Endodontic instruments are used for the removal of the infected pulp and nerve and shaping of the root canal. These instruments need to be flexible since the root canal has curved path. Another important issue is that the dentine part of the teeth should not be damaged by the endodontic files. As a consequence, materials of endodontic

instruments are changed considerably in the past years in order to handle such a sensitive procedure.

Starting in the 1950s, stainless steel, despite its high stiffness, was the most popular material for endodontic files due to its resistance to corrosion and favorable fracture properties. In the mid-1990s, NiTi (Nickel-Titanium) endodontic instruments were introduced for use in root canal procedures. The introduction of NiTi, which is two to three times more flexible than stainless steel, sparked significant interest in research and development within endodontics [2].

Superelasticity and shape memory effects are pivotal in the application of endodontic instruments during root canal procedures. These instruments are required to withstand high stresses and large strains, around 10 percent, for brief durations. Superelasticity allows NiTi endodontic files to withstand large deformations during root canal procedures and revert to their original shape afterward [3]. Additionally, the shape memory property is beneficial for reverting to a predetermined shape at body temperature, facilitating access to highly curved root canals [4]. However, NiTi endodontic files have a shorter fatigue life and higher failure rates compared to steel ones. Failure of endodontic files during the root canal procedure poses a difficulty in removal of the failed piece from the root canal, hence the majority of manufacturers advocate for a single-use policy for their endodontic files [5]. Recently, despite the prevalent use of conventional alloy-based endodontic file sets, significant advancements have been made in the development of endodontic file sets that incorporate a blend of different metallic phases or undergo heat treatment. For example, M-Wire endodontic files, which include small amounts of R-phase and martensite, offer improved flexibility and fatigue resistance compared to conventional NiTi files. These innovations aim to not only enhance durability but also improve flexibility, offering significant advancements in the performance and reliability of endodontic instruments [6].

Despite advances, the reusability and failure of NiTi endodontic files remain problematic, making this an important area of discussion, especially for endodontic files

made from conventional NiTi alloys. Consequently, this study focuses on improving the understanding of endodontic files' mechanical behavior and their failure during root canal procedures. To understand the risk of file and tooth fractures, the study develops a computational model to predict failure modes and the fatigue behavior of endodontic files. Key objectives include selecting an appropriate constitutive model, developing a finite element analysis methodology that aligns with standardized bending and torsion tests under ISO 3630-1 standards, as well as cyclic fatigue tests. Additionally, the objectives involve simulating root canal procedures using actual tooth geometry and conducting a sensitivity analysis to tooth material properties. The research predominantly addresses endodontic files made from conventional NiTi alloys and utilizes the ProTaper Universal file set within the Abaqus software framework, capitalizing on Abaqus built-in constitutive models without the need for custom subroutines.

1.2. Root Canal Treatment Procedure

Root canal treatment incorporates various steps as mentioned in the previous section which are depicted in Figure 1.2 and can be summarized as [7];

(i) Removing part of the tooth crown to access the root canal
(ii) Removing the infected pulp and nerve in the root of the tooth
(iii) Root canal preparation
(iv) Filling the root canal with gutta-percha and adhesive cement
(v) Replacing the crown with biocompatible material

Endodontic files are used for removing infected pulp and nerves from a tooth's root and for preparing the root canal. This process involves enlarging the canal by removing dentin tissue, creating space for disinfection solutions, and facilitating the placement of a filling. The mechanical shaping of the root canal, performed using endodontic files, is a central focus of this thesis and will be elaborated in detail in Chapter 3.

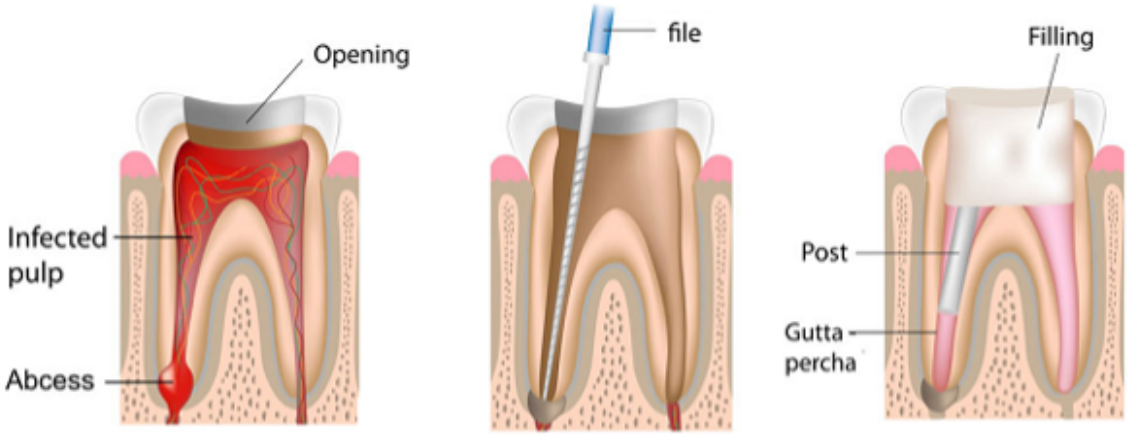

Figure 1.2. Root canal treatment steps [7].

1.3. General Aspects of Rotary Endodontic Files

In the field of endodontics, the design of root canal preparation instruments is influenced by principles similar to those used in creating drills and reamers for woodworking and metalworking. These instruments not only remove infected tissue but also excise a portion of the dentin tissue to shape the canal. Typically, an endodontic instrument consists of a handle section, a shaft section, and a working section (blade) [8]. This configuration is illustrated in Figure 1.3, which presents the main sections of ProTaper Universal F2 endodontic file.

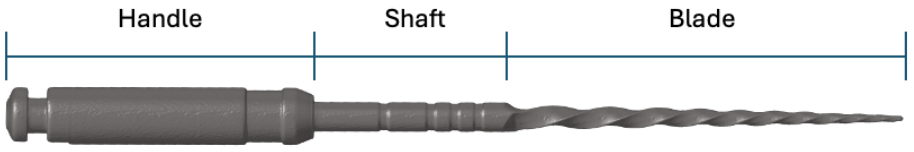

Figure 1.3. ProTaper Universal F2 endodontic instrument main sections.

An endodontic file set comprises several files, each with a distinct blade design tailored to operate at the different lengths of the root canal. Dentists utilize these

endodontic files in a specific sequence, following the operational procedures and also the guidelines recommended by the manufacturer. The non-heat-treated ProTaper Universal endodontic file set consists of shaping files Sx, S1, and S2, and finishing files F1, F2, and F3 [9]. The heat-treated MTwo endodontic file set includes files with specifications 10/.04, 15/.05, 20/.06, 25/.06, 30/.05, and 35/.04 [10]. Additionally, the heat-treated ProTaper Next endodontic file set comprises files X1, X2, X3, X4, and X5 [11]. These file sets are illustrated in Figure 1.4.

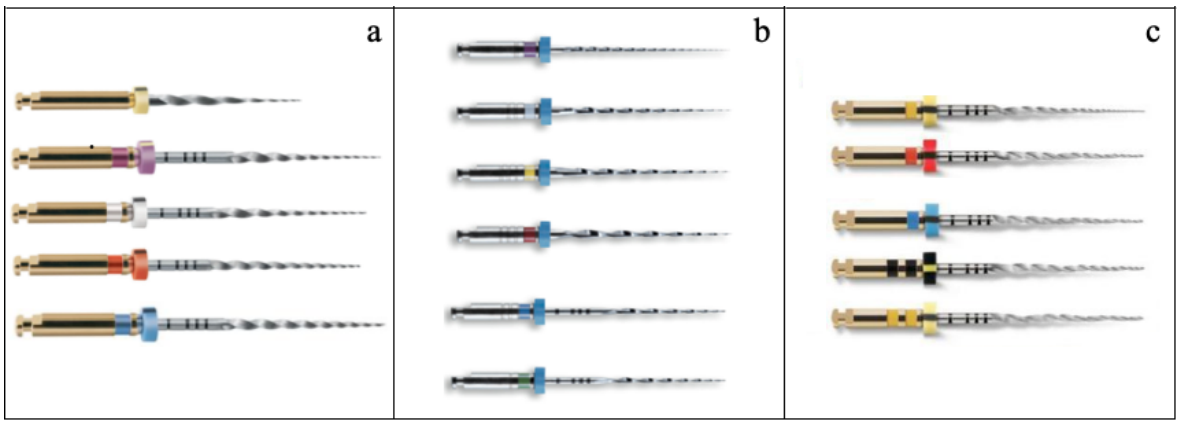

Figure 1.4. File Sets [12]: a) ProTaper Universal, b) MTwo, c) Protaper Next.

Endodontic files are subjected to significant loads during use, primarily enduring torsional loadings due to resistance from dentin removal. Additionally, they experience cyclic bending loads as they rotate within the canal during the procedure. These loadings can lead to torsional failure, typically when the endodontic file tip becomes lodged in the dentin tissue and the stresses surpass the material's elastic response range. Another common issue is fatigue failure, primarily resulting from cyclic bending loads induced by the curvature of the root canal. Understanding these stresses is essential for optimizing file design and material selection to enhance performance and prevent failures, thereby improving the safety and efficiency of root canal treatments [13].

1.4. Structural Evaluation of Endodontic Files

Given the susceptibility of Ni-Ti endodontic files to structural failure during root canal procedures, a variety of testing methodologies have been developed. Physical tests focus on bending and torsional stiffness, adhering to ISO 3630-1 standard protocols [14]. Torsion tests assess fracture resistance and torsional stiffness, which is the resistance of an endodontic file to twisting when subjected to an external load or force, using a torque testing apparatus where the file is twisted until it fractures. Bending tests measure bending stiffness which is the resistance of an endodontic to bending when subjected to an external load or force, with an apparatus that applies torque to an endodontic file by its handle. Additionally, cyclic fatigue tests, which lack a universal standard, evaluate the fatigue life of files by rotating them in simulated canals until failure [15]. These tests help compare different file types and treatment conditions to determine their durability and performance under similar root canal treatment operation conditions. A detailed description of these methods is presented in Chapter 4 of this work.

Furthermore, computational approaches have been developed to simulate these physical tests, in order to reduce the testing costs and efforts. Examination of the Finite Element simulations of physical tests reported in the literature demonstrates that numerous studies concentrate on modeling of ISO 3630-1 bending and torsion test scenarios. On the other hand, there are limited amount of studies focusing on the cyclic fatigue behaviour of endodontic files operated in simulated root canals.

Considering the simulation of bending and torsion, there are various studies in the literature which try to create the computational models of ISO bending and torsion tests, which also evaluate the structural stiffness and characteristics of various file sets.

Arruda et al. [16] compared three different nickel-titanium rotary files using experimental methods and finite element analysis. Torsional stiffness and flexibility in bending were investigated experimentally according to ISO 3630-1. The tests were

simulated in Abaqus employing a superelastic material model for NiTi. The same material model parameters were used for all endodontic files. Analysis and experimental displacement-moment and rotation-torque curves were found to be in agreement with the test data for torsion and bending loading. Torsional stiffness values differed considerably among endodontic files due to geometric differences. Camara et al. [17] compared the flexibility and mechanical response of ProTaper and ProTaper Universal files, whereas El-Anwar et al. [18], performed finite element analysis of continuously rotating endodontic files (GTX and ProTaper) with reciprocating WaveOne file to evaluate the effects of design and material on the instrument's lifespan. The analysis showed endodontic files manufactured from M-Wire NiTi alloy to be slightly more resistant to failure than the endodontic files manufactured from conventional NiTi alloy under normal conditions, though both materials performed similarly in severe locking conditions. Larger cross-sectional areas improved failure resistance, and the cross-sectional shape and cutting angles impacted cutting efficiency. This suggests M-Wire instruments may offer longer lifespans than conventional NiTi instruments under similar conditions. Prados-Privado et al. [19] conducted a finite element analysis to compare the bending and torsional properties of four different NiTi endodontic files, specifically focusing on their performance under ISO 3630-1 specified conditions. The analysis revealed significant differences in stress levels and flexibility among the files, demonstrating that thermal treatment can enhance file flexibility and resistance during root canal preparation. Maximum von Mises stress locations predicted by the analysis are in accordance with cyclic fatigue failure areas. Martins et al. [20] utilized finite element modeling to examine the impact of cross-sectional eccentricity on NiTi endodontic files, specifically analyzing ProTaper Next X1 and X2 instruments. By comparing these with concentrically cross-sectioned models under ISO 3630-1 flexion and torsion conditions, findings revealed that eccentric files have less flexibility but exhibit a beneficial change in stress distribution, leading to lower maximum stress under bending, without significant torsional differences. The benefits of eccentricity lie not in increased flexibility but in enhanced root canal shaping efficiency, reduced stress, and potentially longer fatigue life. Bonessio et al. [21] compared torsional behavior of instruments made of M-Wire and conventional NiTi. The geometry of the files was obtained with micro-computed

tomography and transformed into three-dimensional volume. Both materials were represented as plastic with hardening model. Finite element analysis results were validated against in vitro tests. The predictions agreed well with tests up to fracture. M-Wire files showed higher flexibility at small deflections, however insignificant difference was predicted in large deflections. The study also showed the effect of the alloy properties on the performance of the files, in particular torque angle at fracture. Chevalier et al. [22] studied the effects of different loading paths on the mechanical behavior of NiTi endodontic instruments. In a three-dimensional finite element analysis, NiTi was modeled with linear elastic, elastoplastic and superelastic material models. Loading conditions consisted of bending, torsion and non-proportional bending-torsion. In conclusion, the importance of an adequate material model accounting for superelasticity of endodontic instruments used for canal treatment was pointed out. Arbab-Chirani et al. [23] compared the torsional and bending behavior of five different endodontic files. Three-dimensional finite element model of the files with superelastic material model was constructed. Handles of the files were fixed. Bending case was simulated with 3.8mm tip deflection and torsion case was created with 22° tip rotation. The bending simulations predicted the maximal equivalent stress level to be in the curved part of each instrument. Under torsion, the maximal equivalent stress was predicted to be at the tip of the instruments.

The literature features numerous studies on rotary endodontic files' structural assessment through finite element analysis. While these studies often detail simulated loading and fixation conditions, they generally lack in-depth descriptions of boundary conditions, load application, and crucial details about the geometry and finite element mesh for both the files and testing apparatus. There is also a noticeable gap in exploring alternative modeling approaches, indicating a need for more comprehensive methodological transparency and innovation.

Regarding the simulation of fatigue response, within the literature, studies focusing on the finite element modeling of cyclic fatigue are scarce. Lee et al. [24] conducted cyclic fatigue tests on ProTaper Universal endodontic instruments and performed sim-

plified finite element simulations. This study compares the failure locations of the files in the tests with the peak stress locations derived from the finite element analysis. Similarly, Kim et al. [25] simulated the mechanical behavior of three different NiTi endodontic files during their insertion into the root canal. Three-dimensional finite element models of the files and the root canal were created using data from the manufacturers. The files were modeled with a superelastic material model, although details of the root canal modeling were omitted. The endodontic files were rotated at 240 rpm while moving inside the root canal before being withdrawn. The study compared predictions of maximum Von Mises stress during operation and residual stresses upon withdrawal for different files; however, it did not emphasize fatigue life assessment. Scattina et al. [26] devised a testing apparatus, conducted durability tests on ProTaper Next files, and developed a numerical model that related calculated principal stresses to the measured fatigue life of the file set.

In summary, while these studies demonstrate a correlation between simulation results and test data regarding the fatigue behavior of endodontic files, they fail to provide comprehensive modeling details for the test apparatus, file fixation conditions, simulation settings, and contact definitions. It is also worth noting that a proper low-cycle evaluation approach needs to be selected for representing the fatigue behaviour of endodontic files.

1.5. Objectives of the Study

Endodontic files are simultaneously subjected to cyclic torsion and bending during the root canal procedure. During the operation, files need to reach the lower part of the root canal which requires the instrument to bend. Removal of infected tissue is achieved by rotation of the instruments resulting in cyclic torsional loads on the file.

The fracture of endodontic files is primarily attributed to cyclic loading. Misapplications during root canal treatment can also lead to file fractures. Compared to steel files, NiTi files have a shorter fatigue life and are limited in their reusability, which

is a significant drawback. Additionally, tooth fractures may occur during root canal procedures when the file comes into contact with dentin, with the forces exerted by the endodontic file causing these damages. Moreover, understanding the mechanical response of these files during treatment is crucial for selecting the appropriate endodontic file for a specific root canal curvature and operational technique. As a result, various structural assessment physical test methodologies have been developed to understand the mechanical limits and responses of these instruments better. Significant efforts have been made to measure and comprehend the structural stiffness and failure behavior of different endodontic file sets. The bending and torsional stiffness of these instruments are evaluated using standardized tests, as defined by ISO 3630-1. For measuring the cyclic fatigue durability of endodontic files, there are several approaches, typically involving the introduction of the endodontic instrument into a simulated root canal and subjecting it to rotation until failure occurs.

In addition to these efforts, there has also been a significant effort on decreasing testing and reducing costs through the development of simulation methods replicating physical tests. Nevertheless, a thorough computational analysis of the files during root canal treatment is not available, especially, considering the fatigue behaviour of endodontic instruments. The main goal of this study is to develop a computational procedure to identify possible failure modes and predict the fatigue behaviour of endodontic files by simulating their mechanical behavior and interaction with the tooth during the root canal procedure.

Particular objectives of the thesis can be summarized as;

(i) Selection and calibration of a constitutive model suitable for modeling the mechanical behavior of endodontic files during root canal procedures.
(ii) Development of a finite element analysis methodology for endodontic files based on the procedures specified in ISO 3630-1
(iii) Development of a finite element analysis methodology for endodontic files based on a selected cyclic fatigue test systems

(iv) Development of a finite element analysis methodology of the root canal procedure considering a real molar tooth geometry

(v) Identification of a low-cycle fatigue approach for evaluating the fatigue behavior of endodontic instruments

(vi) Finite element simulations of endodontic files for cyclic fatigue assessment by considering the cyclic fatigue test systems and real molar tooth model for selected operational techniques

(vii) Sensitivity analysis of developed models with respect to file geometry and material model parameters.

The development of the methodology primarily focuses on endodontic files made from conventional NiTi alloys, which are more susceptible to cyclic failure despite being commonly used for root canal treatments. The finite element analysis methodology proposed within this work is specifically developed with the ProTaper Universal file set in mind. This set is chosen because it is widely used for root canal treatments, and ample data about it is available in the literature.

The thesis is structured as follows: Chapter 2 presents the design parameters, classifications based on alloy composition, and failure modes of endodontic files. Chapter 3 discusses the operational techniques for shaping the root canal. In Chapter 4, structural assessment methods for endodontic files are detailed, explaining the systems and methodologies involved. Chapter 5 introduces the built-in Shape Memory Alloy (SMA) constitutive model incorporated into Abaqus software and elaborates on its implementation. Chapter 6 focuses on Finite Element Modeling and Simulation of the ISO 3630-1 physical tests, the Gambarini cyclic fatigue test configuration, and the FEA modeling of a real molar tooth with its relevant tissue structure. Chapter 7 presents all the results with detailed discussions. The final chapter summarizes the outcomes of the current work and suggests possible future research directions.

2. NICKEL TITANIUM ENDODONTIC FILES

In this section, we provide a detailed analysis of rotary endodontic instruments, focusing on their design parameters and the general classification based on the materials used in their construction. Additionally, we explore the various failure modes of endodontic files, discussing how different design and material choices impact their performance and durability in clinical settings. This comprehensive overview aims to enhance understanding of the critical factors influencing the efficacy and reliability of these essential dental tools.

2.1. Design

The design of endodontic files is determined by the target section and length of the root canal to be treated, as well as the canal morphology. Additionally, the design influences the bending and torsional stiffness of the file, as well as its fatigue life. Key design parameters, such as the tip, flute properties influenced by the taper, and cross-sectional features seen in Figure 2.1, play a pivotal role in the functionality and effectiveness of endodontic files in root canal therapy [27].

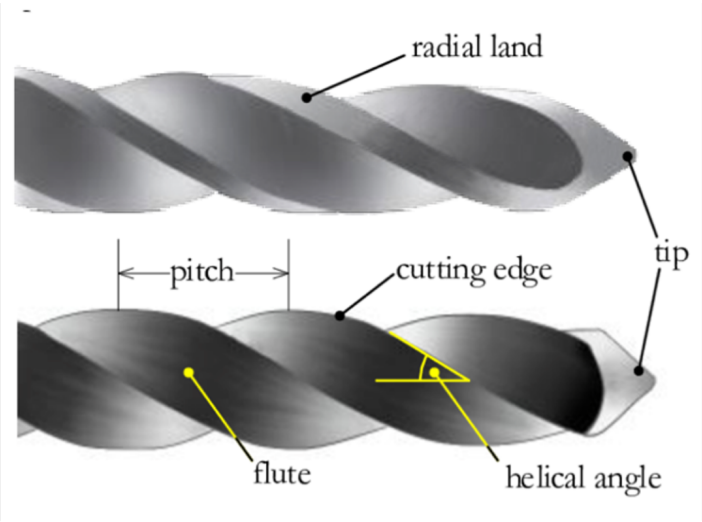

Figure 2.1. Endodontic file design parameters [28].

The evolution in the design of root canal preparation instruments reflects a continual effort to optimize clinical outcomes. By enhancing the control, efficiency, and safety of these tools, endodontic therapy aims to achieve thorough cleaning and shaping of the root canal system, minimizing the risk of procedural errors and improving the prognosis of endodontically treated teeth.

2.1.1. Tip Design

The design of the instrument tip is crucial for two primary functions: guiding the file through the complex anatomy of the root canal and facilitating penetration into deeper sections of the canal. The efficiency and safety of rotary instruments are significantly influenced by their tip designs. Improper use based on a misunderstanding of these designs can lead to complications such as canal transportation or even file breakage due to excessive torsion. The cutting capability of a file tip is defined by its geometric features, including the angle and radius of its leading edge and how closely the flute approaches the tip. These characteristics directly impact the file's ability to cut and its likelihood to alter the canal's intended path [27].

2.1.2. Longitudinal and Cross-Sectional Design

The configuration of the flutes is a critical aspect of a file's design, primarily serving to efficiently remove soft tissue and dentin chips from the canal walls. Its effectiveness depends on several factors, including the depth, width, and the precision of the flute's surface finish. The interaction of the flute with the canal wall, especially at the leading (cutting) edge, is crucial for the instrument's ability to cut tissue and eject chips effectively. The flute's ability to remove tissue in principle is determined by the cross-section design parameter rake angle at the cutting edge which can be considered as positive (cutting) or negative (scraping) as illustrated in Figure 2.2 [27].

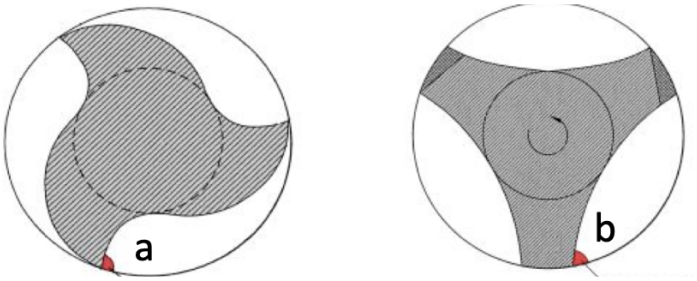

Figure 2.2. Cross section of endodontic files with (a) Positive (Cutting) and (b) Negative (Scraping) rake angle [12] .

Additionally, some files feature a radial land design element that increases the contact area with the canal wall, supports the cutting edge, limits the depth of cuts, and reduces the file's tendency to overly engage with the canal walls [29]. The cross-sectional design also affects the fatigue behavior of the file. Generally, a larger main diameter tends to decrease the fatigue life for a given cross-section design. However, this larger diameter also enhances the torsion and bending stiffness of the file, which increases the file's capacity to exert greater force on the canal surface [30].

2.1.3. Taper

The concept of taper in root canal instruments is fundamental, denoting the gradual increase in diameter from the file's tip to its handle as shown in Figure 2.3. This feature is quantified as the amount of diameter increase per millimeter, affecting the instrument's ability to shape the canal efficiently. Instruments may exhibit either a constant or variable taper, with recent innovations introducing variations in the helical angle, pitch, and taper along the length of the instrument. These design modifications, coupled with advancements in materials science and changes in operational parameters such as rotational speed, collectively influence the cutting behavior of the instruments [27]. It is important to note that the taper of the file impacts its fatigue resistance; a greater taper generally leads to a shorter fatigue life. Additionally, a larger taper reduces the flexibility of the instruments. It is crucial to remember that instruments

working closer to the apical section of the root canal require increased flexibility to properly enlarge the canal [30].

Figure 2.3. Endodontic file taper definition.

2.2. NiTi Material Properties

The mechanical response of NiTi files subjected to bending and torsion is primarily related to the evolution of material phases at the microscopic level, specifically the transition between martensite and austenite phases. Austenitic alloys, characterized by a face-centered cubic crystal structure, are soft and ductile at higher temperatures, allowing for easier manipulation. Martensitic alloys, on the other hand, exhibit a body-centered tetragonal crystal structure and are harder and more brittle at lower temperatures, providing increased rigidity, which is essential for precision in dental procedures. [31]. These microstructural changes manifest themselves at the macroscopic level through the constitutive behavior effects called the shape memory effect and superelasticity (pseudoelasticity) [32].

The shape memory effect allows materials to revert to their original shape when heated, following specific phase changes under thermomechanical stress. This process involves transitions between austenite and martensite phases depending on temperature variations and mechanical forces, resulting in the material "remembering" its shape at high temperatures. Superelasticity, also known as pseudoelasticity, enables materials to withstand and recover from significant deformations during cyclic loading at elevated temperatures through similar phase transformations [32].

2.3. Classification of Ni-Ti Rotary Instruments Based on Alloy Composition

The classification of nickel-titanium (NiTi) alloys used in endodontic instruments can be broadly divided into two categories based on their microstructure: Austenitic and Martensitic [3].

2.3.1. Austenitic Ni-Ti Alloys

Austenitic NiTi Alloys predominantly consist of the austenitic phase and are renowned for their superelastic properties, stemming from the stress-induced transformation to martensite. These alloys are typically classified into three categories [3].

Conventional austenitic alloys, in principle, do not undergo specialized heat treatment. They have the ability to revert to their original shape after deformation, making them well-suited for shaping straight or moderately curved root canals, as exemplified by the ProTaper Universal. This work primarily focuses on endodontic instruments manufactured from conventional austenitic alloys.

R-Phase austenitic alloys undergo specific thermal treatments to stabilize the R-Phase, a distorted phase that occurs prior to the transformation from the austenite phase to the martensite phase and has a lower elastic modulus compared to both austenite and martensite phases, within the austenitic matrix, offering a balance between flexibility and strength. These alloys exhibit superelasticity and are often used in instruments requiring enhanced flexibility, as demonstrated by WaveOne Gold.

M-Wire austenitic alloys includes small amounts of R-phase and martensite, offering improved flexibility and fatigue resistance compared to conventional NiTi.

2.3.2. Martenisitic Ni-Ti Alloys

Martenisitic NiTi Alloys are primarily martensitic and generally classified into four categories [3].

CM Wire is although martensitic, it also includes varying amounts of austenite and R-phase. These alloys show a controlled memory effect, are deformable (pseudo-plastic), and possess a shape-memory effect. Instruments made from CM Wire exhibit superior flexibility and cyclic fatigue resistance, making them ideal for navigating complex root canal anatomies.

Gold Heat-treated alloys undergo a heat treatment process that enhances their flexibility and cyclic fatigue resistance significantly. They are characterized by a superior flexibility and enhanced resistance to cyclic fatigue.

Blue Heat-treated are similar to the gold heat-treated alloys but designed to offer a greater angle of rotation at fracture and lower maximum torque, indicating a focus on maximizing the resistance to cyclic fatigue while maintaining sufficient flexibility.

MaxWire is a unique alloy that exhibits martensitic behavior at lower temperatures and transforms to austenitic at body temperature, enabling a shape-memory effect and superelasticity. This dual-phase behavior allows for exceptional adaptability within the root canal system.

2.4. Failure Modes of Rotary Endodontic Files

NiTi endodontic instruments encounter failures in clinical practice due to their fracture susceptibility. The primary modes of fracture in these instruments are torsional failure and cyclic fatigue, each with distinct mechanisms and implications for endodontic treatment [13].

2.4.1. Torsional Failure

Torsional failure occurs when a part of the instrument, typically the tip, becomes lodged within the root canal while the handpiece continues to rotate. This results in the application of torque that exceeds the instrument's elastic limit, leading to a fracture. Stresses resulting from torsion during the cutting actions within the canal, making torsional failure a significant risk during endodontic procedures. The assessment of an instrument's resistance to torsional failure involves measuring maximum torque and angle of rotation at the point of fracture [13].

2.4.2. Cyclic Fatigue

Cyclic Fatigue is another prevalent mode of failure that involves the initiation and propagation of microcracks along specific crystallographic planes or grain boundaries within the material. This process begins with the formation of microcracks that grow over time under the stress of repeated bending and unbending deformations, particularly in curved canals, until the instrument ultimately fractures. The resistance to cyclic fatigue is commonly evaluated by measuring the number of cycles until fracture occurs or by counting the number of cycles to fracture (NCF) [13].

3. ROOT CANAL PREPARATION PROCEDURE

During the root canal shaping and dental removal process, the choice of operational technique which is influenced by the canal morphology, significantly impacts the fatigue life of endodontic files, making it an important subject to consider in this work. This thesis focuses on investigating how different techniques affect the durability and fatigue behaviour of endodontic instruments, specifically the pecking motion and reciprocating motor motion which are detailed in Section 3.1.

In principle, there are three main aspects of the canal preparation process:

Considering the mechanical aspect of the canal shaping process, primary goal in root canal instrumentation is to evenly shape the original canals, ensuring all surfaces are prepared. Preparation should avoid errors like deviations and perforations, which, while not necessarily impacting treatment success, hinder complete disinfection. Preserving cervical and radicular dentin is also crucial to maintain root strength and avoid fractures. Anatomical studies have shown that pre-shaping dentin thickness can be as low as 1 mm, and canal straightening may further reduce this, particularly in curved areas. Although a specific minimum thickness for radicular walls has not been set, 0.3 mm is often considered critical. To prevent excessive removal and perforations, it is important to ensure careful access cavity preparation and appropriate enlargement of the canal's coronal third [27].

Biological aspect states that, canals should be uniformly tapered to aid obturation, but not necessarily for antimicrobial effectiveness. Yet, the shape of canal preparation is crucial for removing infected tissue and ensuring effective delivery of disinfectants. Traditionally, irrigants are passively introduced into canals using syringes and needles, with the fluid advancing only slightly beyond the needle's tip. Utilizing finer needles and enlarging the apical canal may enhance the depth of needle insertion, improving canal cleaning and disinfection. However, thoroughly cleansing the canal's

apical region remains challenging, particularly in narrow and curved canals [27].

Regarding the technical aspect of the shaping process, while aiming for a continuous taper that follows the root canal's original shape is standard, there is debate over the ideal final size and taper in root canal therapy. Some advocate for larger apical sizes (e.g., #50 or greater) with smaller tapers (.02 to .05) to enhance disinfection, while others see no significant difference between small and large final sizes. The introduction of a self-adjusting file, which doesn't conform to a specific size but is believed to improve cleaning through increased contact with the canal walls, especially in wider canals, adds to the diversity of approaches [27].

3.1. Root Canal Preparation Clinical Techniques

Root canal preparation involves assessing and enlarging canals to remove infection and ensure proper filling. Clinically determining apical diameters is challenging, with a preference debate existing between smaller and larger apical preparations for effective disinfection and irrigation. Maintaining the canal's original path is crucial for reaching bacteria in the apical third. Studies highlight that larger preparations facilitate better bacterial removal but may lead to preparation errors. Various studies have explored the impact of canal preparation size on bacterial elimination, with mixed results, suggesting that the extent of dentin removal might not always correlate with better outcomes. Root canal preparation strategies encompass various techniques, including the crown-down, step-back, and apical widening approaches, each designed to achieve specific objectives in cleaning, shaping, and disinfecting the canal. These techniques are further refined with the advent of NiTi rotary instruments, which offer enhanced flexibility and efficiency, particularly in negotiating complex canal anatomies.The use of dedicated NiTi instruments and proper access cavity preparation is highlighted for achieving ideal canal shapes and avoiding excessive dentin removal, which could compromise the tooth's structural integrity [27].

Considering the use of rotary NiTi instruments, where the endodontic file is rotated with the guidance of an electric motor, commonly used clinical techniques can be stated as follows:

3.1.1. Crown Down Technique

The crown-down technique has long been a foundational method in endodontics and remains in use due to its effectiveness. In this technique, the working length of the canal is determined after enlarging the coronal portion, followed by establishing an open glide path with specific files up to a predetermined size, depending on the unique anatomy of the canal. Preparation typically starts with instruments featuring a certain taper in descending diameters. For narrower or more complex canals, instruments with a slightly smaller taper are used next, also in descending diameters. Apical preparation may involve various shaping strategies or a step-back approach [33].

3.1.2. Single Length with Pecking Motion Technique

The approach to root canal preparation using specific NiTi rotary instruments differs by not following the traditional crown-down method. This process starts with inserting hand files of two sizes into the upper two-thirds of the canal to create a smooth path for the following instruments, which are designed to shape the canal sides gently. These shaping tools are used with care, along with irrigation, to avoid aggressive cutting and ensure the canal is correctly shaped . After shaping, irrigation helps remove debris, a step repeated until the desired canal depth is achieved. The next phase involves enlarging the canal's end section to ensure it's properly shaped for the final filling. The procedure uses a combination of specific motions to gently shape the canal without aggressive brushing [33].

The brushing motion, also known as pecking motion is a technique which is recommended for reducing the risk of failure of the endodontic file and reducing its screw-in tendency. The latter is defined as sticking of the file's cutting edge into the

dentin tissue during the root canal treatment due combined effect of the applied forces, root canal geometry, and endodontic file design [34]. The pecking motion technique is also known to increase the cutting efficacy of the single file systems [35].

The effect of pecking motion technique on the file durability and fatigue behaviour is thoroughly investigated in this work and the FE modeling aspects are presented in Chapter 6.

3.2. Working Modes of Rotary Instruments

The evolution of rotary instruments in endodontics has introduced various working modes to enhance root canal preparation. Initially, the centrifugal rotary motion, established in the early 1980s, became the standard due to its continuous 360-degree rotation. However, this method's tendency to cause instrument fractures prompted the exploration of alternative movements [33].

3.2.1. Reciprocal Movement

This movement was first introduced in the mid-20th century by utilizing ProTaper Universal F2 as the plot file, employing an alternating operation that provided a significant shift from traditional practices. This approach uses a single file in a back-and-forth motion, combining clockwise and anticlockwise rotations to complete a full cycle. The reciprocal movement is distinguished by its reduced stress on canal walls, decreasing the likelihood of instrument failure and requiring less effort in canal shaping [33].

This study thoroughly examines how the repicrocal movement affects the durability and fatigue behavior of endodontic files. Detailed information about the finite element modeling can be found in Chapter 6.

3.2.2. Combined Movement (Centrifugal Rotation + Reciprocal Movement)

Recent innovations have seen the development of systems that combine the advantages of both centrifugal rotation and reciprocal movement. These systems adaptively switch between rotational and reciprocal actions based on the resistance encountered within the canal. This dynamic approach aims to mitigate the risk of instrument breakage by adjusting to varying levels of canal resistance, enhancing the safety and efficiency of the procedure [33].

3.2.3. Eccentric Rotary Movement

Certain systems employ an eccentric or asymmetric rotation, characterized by their distinctive movement pattern within the canal. This design aims to improve the engagement with the canal walls, potentially offering a more effective cleaning and shaping process [33].

3.2.4. Translational Movement

A notably different approach involves a system that operates through vertical vibrations combined with an in-and-out pecking motion. This unique movement is designed to optimize the shaping process within a specific time frame, focusing on efficiency and thorough canal preparation.

These advancements signify a continuous effort to refine endodontic treatment, aiming to improve the efficiency of canal preparation, reduce the risk of procedural complications, and enhance overall treatment outcomes [33].

4. ENDODONTIC INSTRUMENTS STRUCTURAL ASSESSMENT METHODS

The literature survey presented in this Chpater focused mainly on the studies concerned with the mechanical behavior of NiTi endodontic files. These studies investigated static behavior, fatigue, and fracture of the files.

Test methodologies primarily concentrates on the standard ISO 3630-1 structural tests, in which the files undergo evaluation for their bending and torsional stiffness characteristics using specially designed test benches [14]. Cyclic fatigue tests are investigated as well, where the files are rotated until failure in simulated canals to assess their overall fatigue behavior.

4.1. ISO 3630-1 Standart

4.1.1. Torsion Tests

Torsion tests are employed to assess the fracture resistance of endodontic files when twisted and to evaluate their torsional stiffness, which is the ratio of applied torque to the resulting angle of twist, using a torque testing apparatus.

The apparatus shown in Figure 4.1 includes a chuck with jaws for clamping the file from its tip, a reversible geared motor for torque application, a torque measuring device and a chuck connected to motor where the handle section is mounted.

The file handle is placed and tightened into the chuck on the motor side leaving a maximum length of 1 mm to the working section of the file. The tip is placed into the jaws of chuck on the opposite side by 3 mm. The torque is applied from the motor and the file is twisted until it fractures. Meanwhile, the torque measuring device records the angular deflection and the torque applied on the instrument.

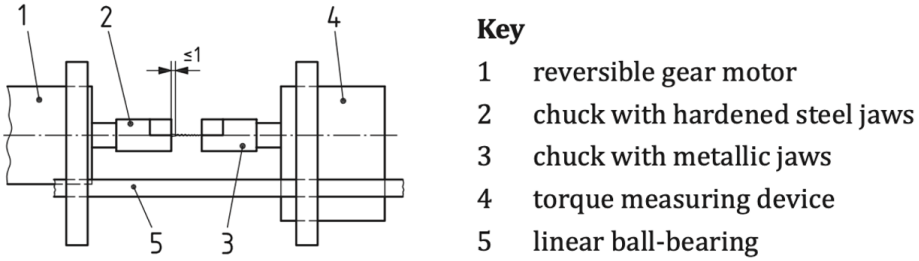

Figure 4.1. Torsion test apparatus [14].

4.1.2. Bending Tests

The bending test apparatus is utilized to measure the bending stiffness, which is the ratio of the bending moment applied to the resulting bending angle of an instrument. Similar to the torque test apparatus, the bending test apparatus includes a chuck with jaws for holding the file by its tip. Additionally, the system includes a catch pin which is connected to a gear motor and a torque measuring device which measures the torque applied by the motor as depicted in Figure 4.2.

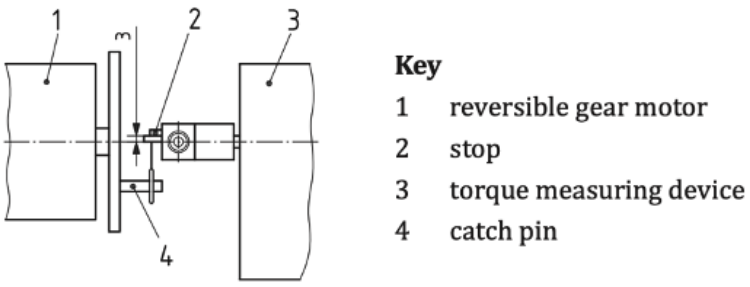

Figure 4.2. Bending test apparatus [14].

The file tip is placed into the jaws of the chuck by 3 mm and tightened. The handle is kept free. The motor is rotated such that the catch pin comes in contact with the file handle. After the contact, the torque is applied by the motor and the catch pin is rotated 45 degrees, subjecting the tested endodontic file to bending. The torque measurement device records the rotation and the applied torque.

4.2. Cyclic Fatigue Tests

Although a universal standard has yet to be established for testing and predicting the cyclic fatigue life of endodontic files, various test configurations and methodologies have been developed for such evaluations [15]. Gambarini et al. [36] described a cyclic fatigue test apparatus and a methodology wherein the endodontic instrument is inserted into a simulated root canal and rotated until failure. Subsequent studies have utilized Gambarini's methodology to explore the cyclic fatigue behavior of various endodontic file sets under different operational conditions. Fife et al. [37] investigated the impact of clinical use on the fatigue behavior of ProTaper endodontic files, whereas Whipple et al. [38] compared the fatigue resistance of ProTaper Universal and V-Taper files. In this study, Whipple also investigated the effects of different root canal treatment techniques in particular pecking motion effect, on the fatigue behavior of the same instrument. Another effort was performed by Rosa et al. [39] to examine the effect of temperature on cyclic fatigue of endodontic instruments. Additionally, Gambarini studied the influence of electromotor torque on the fatigue life of ProFile instruments [40]. Peng et al. [41] evaluated the effect of different curving angles and measured the fatigue life of ProTaper Universal and ProTaper Next endodontic file sets. Savio et al. [15] designed and built a cyclic fatigue test apparatus capable of performing predictive thermographic tests. Furthermore, Peters et al. [42] proposed a state-of-the-art test system for establishing a minimum quality standard based on testing conditions and material characteristics for endodontic files. The current study adopts the test apparatus configuration originally proposed by Gambarini, due to the availability of data and its common use in other studies as well.

The test apparatus propoposed by Gambarini et.al [36] utilized for the cyclic fatigue life assessment of the endodontic files contains artificial canals with various curvatures as shown in Figure 4.3. The endodontic file is inserted into these canals and rotated until failure. The cyclic fatigue behavior of the file is characterized in terms of the failure location and the number of rotations to fracture.

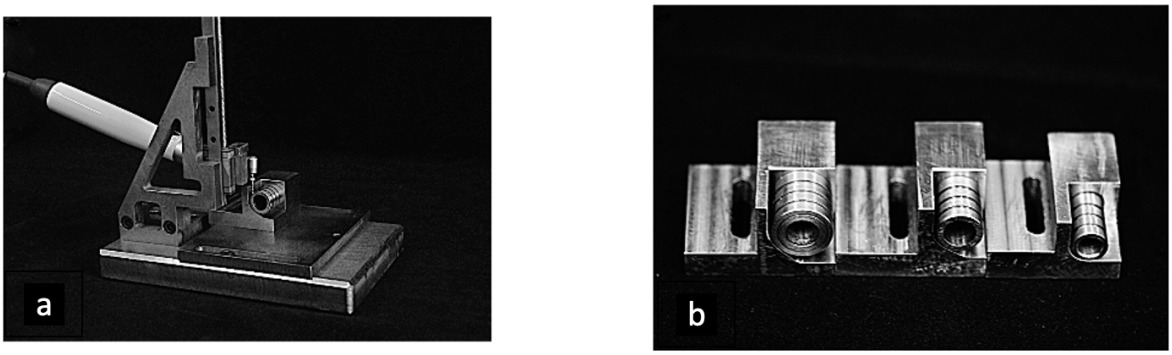

Figure 4.3. Test apparatus proposed by Gambarini [41] (a) Apparatus with the file inserted into the artificial canals (b) Photo of the apparatus in cross-section .

The apparatus is composed of two main components, a steel cylinder with grooves and canals and a steel jig. The 1 mm depth and 1.5 mm width canals are formed between the grooves of the cylinder. The radii of the cylinder and the jig determine the canal geometry while the angle (α) of the jig determines the canal curvature shown in Figure 4.4.

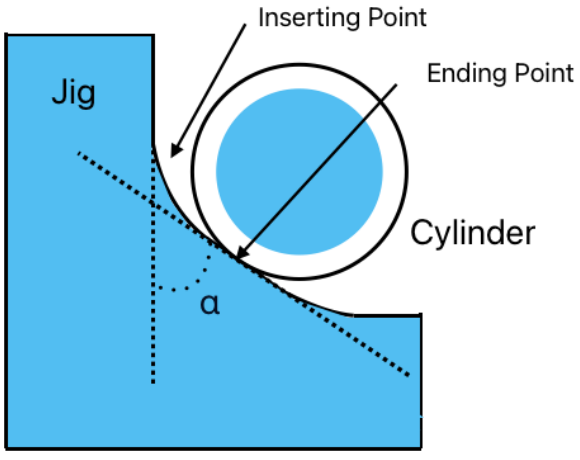

Figure 4.4. Test apparatus cross-section schematics.

The simulated canal commonly considered in the literature has 5 mm radius and 90 degrees curvature and is also used in this work. To create this canal geometry, a cylinder with 6 mm radius and 1 mm deep grooves and a jig with 6 mm radius are

utilized. After such configuration is arranged, the cylinder and the jig are positioned such that the file insertion location has 2 mm width, and the file end point has a 1 mm width. The jig surface is extended 13 mm straight vertically and horizontally before the curvature begins and after it ends as shown in Figure 4.5.

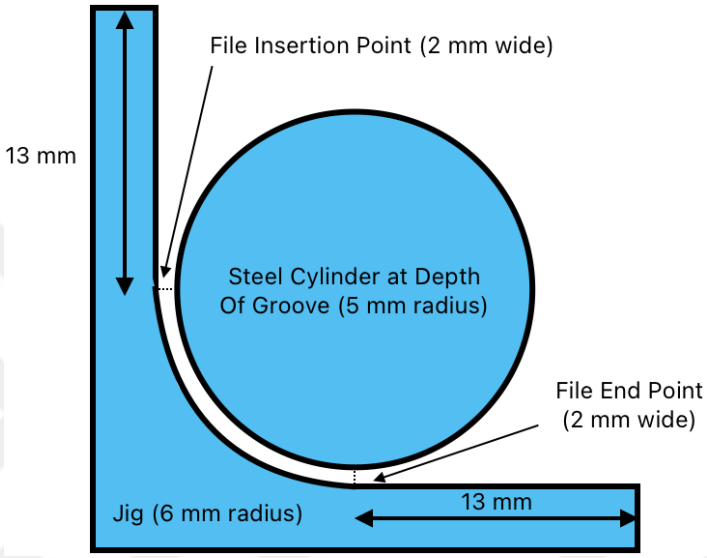

Figure 4.5. Simulated canal geometric parameters.

The handle of the file is attached to an electric motor and the file is inserted for 22 mm from the top of the jig. The file is positioned such that its middle section is in contact with the steel cylinder surface whereas the tip of the file is located around the file end point and in contact with the jig.

After the positioning, the endodontic file is rotated with the aid of the electric motor until failure. During the process, the file is constantly air cooled to maintain the room temperature and lubricated by oil to reduce friction [41].

5. ABAQUS IMPLEMENTATION OF SHAPE MEMORY ALLOY MATERIAL MODEL

The built-in Shape Memory Alloy (SMA) constitutive model incorporated into Abaqus software is based on the formulation proposed by Auricchio et al. [43, 44] taking into consideration of the super elasticty and shape memory effect. During the development of this formulation, they have considered NiTi alloys which are the most commonly utilized shape memory alloys in commercial applications and the formulation is based on phase transformations between two distinct phases: austenite, which is crystallographically more ordered, and martensite, which is less ordered. This formulation is centered around a flow rule that accounts for the transformation rates of the different phases and includes various simplifications for computational efficiency.

In this section, first, we provide general overview of the SMA material general behaviour and properties. Afterwards, we provide a detailed explanation of Auricchio's formulation, with a particular focus on the flow rule. Finally, we highlight the simplifications made in the model and discuss the strengths and weaknesses of its implementation in Abaqus. This section aims to give a comprehensive understanding of how the SMA behavior is modeled within Abaqus and how the model performs under different simulation scenarios.

5.1. Shape Memory Alloy Overview

Shape memory effect refers to material's capability of returning to its original shape after heating. Figure 5.1 shows a shape memory effect and the associated phase changes resulting from a thermomechanical loading path. In the figure, M_S^0, M_F^0, A_S^0, A_F^0 indicate the phase change temperatures corresponding to the beginning and to the end of martensitic transformations at stress free state. The thermomechanical loading path starts at temperature $T > A_F^0$ when the material is at a stress free state and is composed of only austenite phase. During cooling path (a) phase transformation occurs resulting

in the self-accommodating martensite which is variant with minimal internal stress at temperature $T < M_F^0$. During mechanical loading path (b), the self-accommodating martensite phase transforms into oriented state. Unloading of the material path (c) results in residual stresses. When oriented martensite is heated, a reverse transformation occurs, path (d). At temperature $T > A_F^0$ the material transforms into austenite phase and stress-free state is recovered. Therefore, shape memory effect is a thermal recovery where only the high-temperature shape is remembered by the material [32].

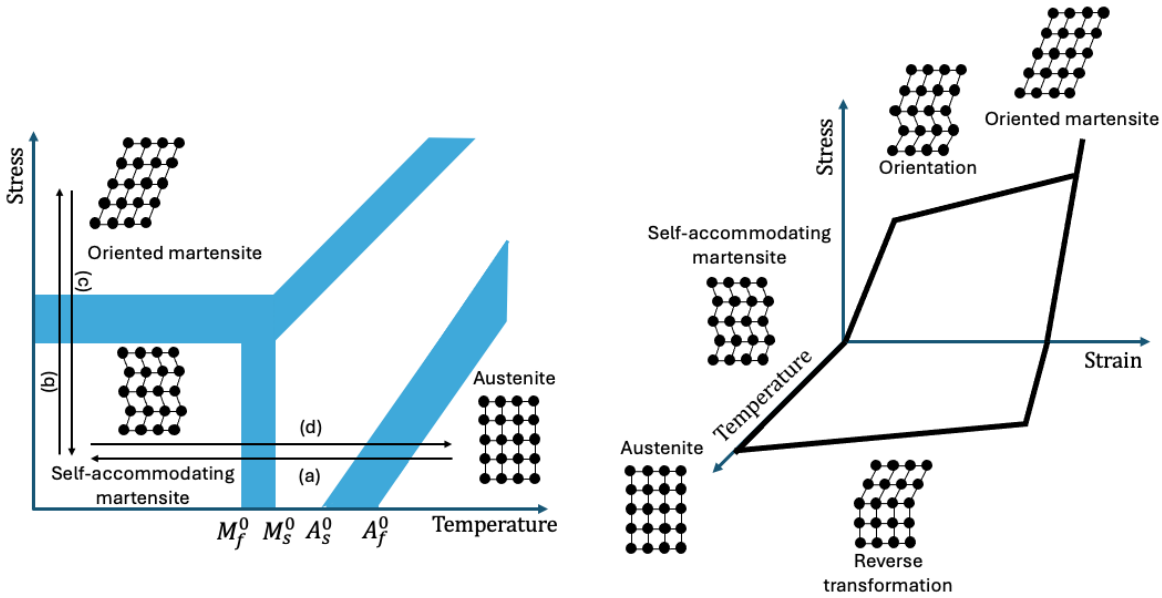

Figure 5.1. Stress-strain-temperature diagram showing shape memory response of NiTi.

Superelasticity or pseudoelasticity refers to the capability of recovering large deformations during loading-unloading cycles at sufficiently high temperatures. Figure 5.2 shows a superelastic tensile response and the associated phase changes resulting from a mechanical loading path. In the figure $\sigma_{ms}, \sigma_{mf}, \sigma_{as}, \sigma_{af}$ represent phase change stresses corresponding to the end of forward and reverse transformations at T_0, a temperature higher than A_F^0 where the superelastic effect usually occurs. During loading path (a) the behavior is elastic until the stress σ_{ms} is reached. At this stress level phase transformation from austenite to oriented martensite begins and reaches the saturation point at stress σ_{mf}. During unloading path (b) reverse transformation from martensite

to austenite occurs and it is completed when the stress is below σ_{as}. As the unloading continues, upon reaching a stress less than σ_{af}, the material recovers its initial shape. Therefore, superelasticity is a mechanical process allowing to recover large strains [32].

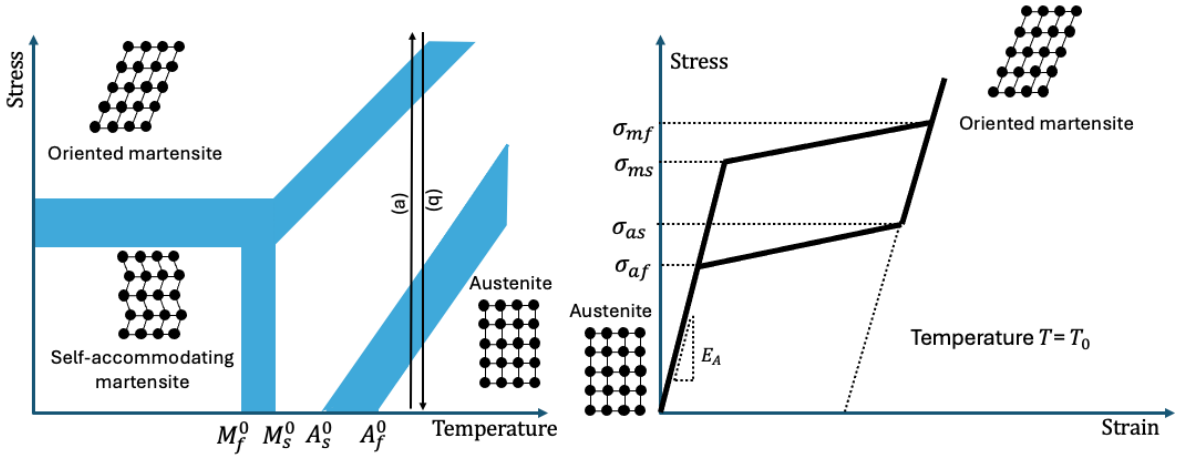

Figure 5.2. A loading program and the corresponding superelastic response of NiTi.

5.2. Shape Memory Alloy Constitutive Model

As stated in the beginning of this Chapter, the constitutive model proposed by Auricchio considers superelasticity and the shape memory effect, focusing on NiTi alloys commonly used in commercial applications. The model is based on phase transformations between austenite (stable at high temperatures and low stress) and martensite (stable at low temperatures) [43, 44].

The phenomenon of superelasticity in materials is largely explained by the transition between austenite and martensite phases. When a specimen, originally in its austenitic state (which remains stable above a designated temperature threshold, T_f^{SA}), is subjected to uniaxial tensile stress while the temperature is held constant, it behaves nonlinearly. This is attributed to the conversion of austenite into martensite induced by stress. Once the stress is removed and the temperature is maintained, the material transitions from martensite back to austenite. The process of applying and then removing stress leads to a closed hysteresis loop in the stress-strain curve, without leaving

any permanent deformation in the specimen, showcasing the superelastic characteristic of the material.

5.2.1. Requirements From the Constitutive Model

Auricchio states that, analysis of the movement and transformation within SMA structures points to the need for internal variables that accurately reflect the phases' presence, characteristics, proportions, and orientations. Moreover, an understanding of the transformation dynamics informs the essential aspects to be incorporated into the model, including:

- The ability to mimic hysteresis by capturing diverse starting and ending points for phase changes.
- The inclusion of stress and temperature as factors affecting phase-transition initiation.
- The acknowledgment of pressure's role in modifying phase-transition thresholds and behaviors.
- The facility to reverse phase transformations through proper thermomechanical cycles.

Given that experiments on various SMAs show their transformations to be unaffected by rate changes, the models were intended to have inelastic, rate-independent properties.

5.2.2. Simplifications

In order to manage the complexity of the problem, Auricchio introduced several simplifications [43, 44].

The primary simplification involves considering only a single variant of martensite in the development of the constitutive model, thereby disregarding the complex multi-

variant structure of the martensite phase. Additionally, the material is presumed to be isotropic, which reduces the model's complexity to consider only two phases: austenite (A) and single-variant martensite (B). This simplification, along with acknowledging the three-dimensional microbehavior of shape memory alloys—where the reorientation process of single-variant martensite is significant—means that, in the most comprehensive scenario, only three phase transformations need to be accounted for.

- Conversion of austenite into single-variant martensite (A→S)
- Conversion of single-variant martensite into austenite (S→A)
- Single-variant martensite reorientation (S→S)

The proposed models are rate-independent.

5.2.3. 1D Model

The super elastic effect is modeled for one-dimensional states of stress. The model considers the uniaxial stress σ and the relative temperature T as the control variables. For the internal variables, the single variant martensite fraction ξ_S and the austenite fraction ξ_A were chosen and the relation defined as

$$\xi_A + \xi_S = 1 \tag{5.1}$$

should be satisfied at any time. The relation,

$$\dot{\xi}_A + \dot{\xi}_S = 0, \tag{5.2}$$

for the rates could be derived.

5.2.3.1. Phase Transformations and Activation Conditions. In the uniaxial case, only two phase transformations were considered by Auricchio which are the conversion of austenite into single-variant martensite (A→S) and the conversion of single variant martensite into austenite (S→A) where the fraction changes of each process are set as,

$$\dot{\xi}_S \;=\; \dot{\xi}_S^{AS} + \dot{\xi}_S^{SA} = 0 \tag{5.3}$$

$$\dot{\xi}_A = \dot{\xi}_A^{AS} + \dot{\xi}_A^{SA} = 0, \tag{5.4}$$

where $\dot{\xi}_S^{AS}$ is defined as the rate of single-variant martensite formation and $\dot{\xi}_S^{SA}$ is defined as the rate of austenite formation.

Regarding the single-variant martensite production, the region could be described with,

$$F^{AS} = \sigma - C^{AS}T \tag{5.5}$$

$$F_s^{AS} = F^{AS} - R_f^{AS} \tag{5.6}$$

$$F_f^{AS} = F^{AS} - R_f^{AS}, \tag{5.7}$$

where, C^{AS}, T_s^{AS} and T_f^{AS} are material parameters representing the slope of the stress temperature lines which can be depicted as ($\partial\sigma/\partial T$ Loading), and the initial and final temperatures at which the transformation can occur under stress free state, respectively. The region within which the transformation may occur is delineated by

$$F_s^{AS} > 0,\ F_f^{AS} < 0 \rightarrow F_s^{AS} F_f^{AS} < 0, \tag{5.8}$$

and represented by Figure 5.3.

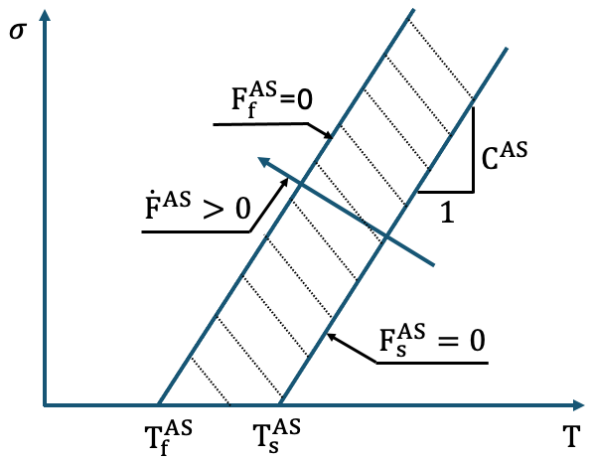

Figure 5.3. 1D model: production of single-variant martensite.

For triggering the formation of single-variant martensite requires either elevat-

ing the stress, lowering the temperature, or applying a suitable mix of these factors. Consequently, the condition, which is expressed as

$$\dot{F^{AS}} > 0, \tag{5.9}$$

is also required. Based on Equations (5.8) and (5.9), the fraction evolutionary equations with Macaulay brackets, are expressed as

$$\dot{\xi}_A^{AS} = K_1^{AS} \left\langle -F_s^{AS} F_f^{AS} \right\rangle \left\langle \dot{F}^{AS} \right\rangle \tag{5.10}$$

$$\dot{\xi}_S^{AS} = -\dot{\xi}_A^{SA}, \tag{5.11}$$

where K_1^{AS} is a scalar function of the control and internal variables.

Regarding the austenite production, the region could be described with,

$$F^{SA} = \sigma - C^{SA} T \tag{5.12}$$

$$F_s^{SA} = F^{SA} - R_f^{SA} \tag{5.13}$$

$$F_f^{SA} = F^{SA} - R_f^{SA}, \tag{5.14}$$

with

$$R_s^{SA} = F^{SA} - T_s^{SA} \tag{5.15}$$

$$R_f^{SA} = F^{SA} - T_f^{SA}, \tag{5.16}$$

where, C^{AS}, T_s^{AS} and T_f^{AS} denote material parameters that signify the slope of the stress-temperature lines which can be depicted as ($\partial\sigma/\partial T$ Loading), along with the initial and final temperatures at which transformation is possible without any stress. The area where this transformation can take place is defined by specific inequalities as

$$F_s^{SA} < 0,\ F_f^{SA} > 0 \rightarrow F_s^{SA} F_f^{SA} < 0, \tag{5.17}$$

and is illustrated in Figure 5.4.

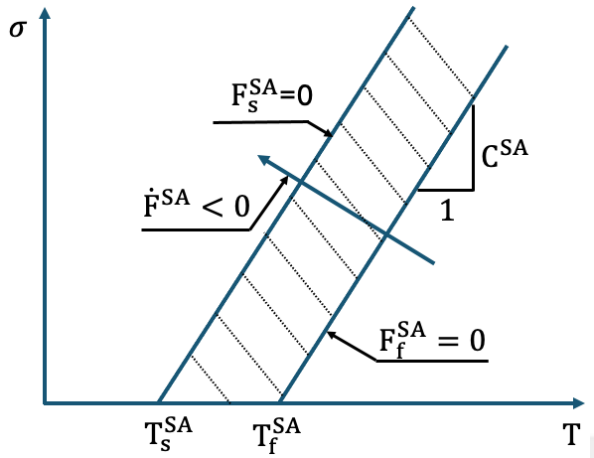

Figure 5.4. 1D model: production of austenite.

Additionally, initiating the transformation back to austenite necessitates either reducing the stress, raising the temperature, or a balanced combination of both. Thus, a specific criterion must be fulfilled to facilitate this transition, which is,

$$\dot{F}^{SA} < 0. \tag{5.18}$$

Drawing from equations 5.17 and 5.18, the evolutionary equations for the fraction are articulated as follows;

$$\dot{\xi}_S^{SA} = K_1^{SA} \left\langle -F_s^{SA} F_f^{SA} \right\rangle \left\langle \dot{F}^{SA} \right\rangle \tag{5.19}$$

$$\dot{\xi}_A^{SA} = -\dot{\xi}_S^{SA}, \tag{5.20}$$

where K_1^{SA} is a scalar function of the control and internal variables.

5.2.3.2. Flow Rule. For the 1D model, the flow rule is associated with the evolutionary rates of the phases. In the linear form, the evolutionary rates of the single-variant martensite was stated by Auricchio as;

$$\dot{\xi}_S = \dot{\xi}_S^{AS} + \dot{\xi}_S^{SA} = -H^{AS}(1-\xi_S)\frac{\dot{F}^{AS}}{F_f^{AS}} + H^{SA}\xi_S\frac{\dot{F}^{SA}}{F_f^{SA}}, \tag{5.21}$$

where the H^{AS} and H^{SA} are the phase transformation activation conditions defined

by;

$$H^{AS} = \begin{cases} 1 & \text{if } F_s^{AS} > 0, F_f^{AS} < 0, \dot{F}^{AS} > 0 \\ 0 & \text{otherwise} \end{cases} \tag{5.22}$$

$$H^{SA} = \begin{cases} 1 & \text{if } F_s^{SA} < 0, F_f^{SA} > 0, \dot{F}^{SA} < 0 \\ 0 & \text{otherwise} \end{cases}. \tag{5.23}$$

5.2.3.3. Kinematics and Constitutive Model. Total strain was decomposed as

$$\epsilon = \epsilon^e + \epsilon_L \xi_S. \tag{5.24}$$

where, ϵ^e is the elastic strain and ϵ_L is the maximum residual strain, meaning the maximum transformational strain which quantifies the greatest deformation achievable through a process of detwinning which is the process of reversing of the formation of twin boundaries within a crystalline structure of multi-variant martensite. Thus, it represents the extent of deformation possible by orienting all single-variant martensite in a single direction.

The stress was related with the elastic strain with

$$\sigma = E\epsilon^e = E(\epsilon - \epsilon_L \xi_S). \tag{5.25}$$

The single-variant martensite fraction is calculated from the evolutionary rates of the single-variant martensite fraction and integrated for achieving the accumulated stress data.

5.2.4. 3D Model

The superelastic effect is modeled for three-dimensional states of stress. This is the generalized version of the 1D model. The model considers the stress $\boldsymbol{\tau}$ and the relative temperature T as the control variables.

For the internal variables, the fraction of single-variant martensite, denoted as ξ_S, and the scaled transformation strain, $\boldsymbol{u}$, were selected. The latter is linearly related to the actual transformation strain according to,

$$\boldsymbol{\epsilon}^{tr} = \epsilon_L \boldsymbol{u}. \tag{5.26}$$

5.2.4.1. Phase Transformations and Activation Conditions. In the three-dimensional case, three phase transformations were considered by Auricchio: the conversion of austenite into single-variant martensite ($A \rightarrow S$), the conversion of single variant martensite into austenite ($S \rightarrow A$) and the reorientation of the single-variant martensite ($S \rightarrow S$) leading to the rate equations,

$$\dot{\boldsymbol{u}} = \dot{\boldsymbol{u}}^{AS} + \dot{\boldsymbol{u}}^{SA} + \dot{\boldsymbol{u}}^{SS} \tag{5.27}$$

$$\dot{\xi}_S = \dot{\xi}_S^{AS} + \dot{\xi}_S^{SA}. \tag{5.28}$$

Regarding the conversion of austenite into single-variant martensite, the region could be described with in the Drucker-Prager loading function form as,

$$F^{AS}(\boldsymbol{\tau}, T) = \|\boldsymbol{t}\| + 3\alpha p - C^{AS}T, \tag{5.29}$$

where $\boldsymbol{t}$ represents the deviatoric component of the stress, p denotes the pressure, C^{AS} and α are the material parameters.

The initial and the final transformation functions are described as,

$$F_s^A S = F^A S - R_f^A S \tag{5.30}$$

$$F_f^A S = F^A S - R_f^A S, \tag{5.31}$$

with;

$$R_s^{AS} = \sigma_s^{AS}\left(\sqrt{\frac{2}{3}} + \alpha\right) - C^{AS}T_s^{AS} \tag{5.32}$$

$$R_f^{AS} = \sigma_f^{AS}\left(\sqrt{\frac{2}{3}} + \alpha\right) - C^{AS}T_f^{AS}, \tag{5.33}$$

where, σ_s^{AS},σ_f^{AS}, T_s^{AS} and T_f^{AS} are material parameters. The criteria for transforming

austenite into single-variant martensite are outlined as,

$$F_s^{AS} > 0, \quad F_f^{AS} < 0, \quad \dot{F}^{AS} > 0. \tag{5.34}$$

Single-variant martensite reorientation process: For the non-proportional changes of stress, reorientation process of the martensite is defined with the equations,

$$F^{SS}(\boldsymbol{\tau}, T) = \|\boldsymbol{t}\| + 3\alpha p - C^{SS}T \tag{5.35}$$

$$F_s^{SS} = F^{SS} - R_f^{SS}, \tag{5.36}$$

with;

$$R_s^{SS} = \sigma_s^{SS}\left(\sqrt{\frac{2}{3}} + \alpha\right) - C^{SS}T_s^{SS}, \tag{5.37}$$

where, C^{SS}, σ_s^{SS}, T_s^{SS} are material parameters. The requirements for the transition from austenite to single-variant martensite are specified as,

$$F_s^{SS} > 0. \tag{5.38}$$

5.2.4.2. Flow Rule. For each transformation process, flow rule is associated with the single-variant martensite rate of fraction and formulated based on the transformation conditions of each process.

Considering the conversion of austenite into single-variant martensite the scaled transformation strain rate equation is depicted as,

$$\dot{\boldsymbol{u}}^{AS} = \dot{\xi}_S^{AS}\mathbf{N}^{AS}, \tag{5.39}$$

where,

$$\mathbf{N}^{AS} = \frac{\mathbf{M}^{AS}}{\|\mathbf{M}^{AS}\|} \tag{5.40}$$

$$\mathbf{M}^{AS} = \frac{\partial F^{AS}}{\partial \boldsymbol{\tau}} \tag{5.41}$$

and F^{AS} is calculated from Equation (5.29). Concerning the development of single-variant martensite, as discussed in Section 5.2.4.1, the equation is presented in a linear form as,

$$\dot{\xi}_S^{AS} = -H^{AS}(1-\xi_S)\frac{\dot{F}^{AS}}{F_f^{AS}}, \tag{5.42}$$

where the H^{AS} is the phase transformation activation condition defined by,

$$H^{AS} = \begin{cases} 1 & \text{if } F_s^{AS} > 0, F_f^{AS} < 0, \dot{F}^{AS} > 0 \\ 0 & \text{otherwise} \end{cases}. \tag{5.43}$$

For the conversion of single-variant martensite into austenite, the scaled transformation strain rate equation is depicted as,

$$\dot{\boldsymbol{u}}^{SA} = \dot{\xi}_S^{SA}\mathbf{N}^{SA}, \tag{5.44}$$

where,

$$\boldsymbol{N}^{SA} = \frac{\boldsymbol{u}}{\|\boldsymbol{u}\|}. \tag{5.45}$$

It should be noted that the transformation from martensite back to austenite is solely accompanied by a rescaling of the transformation strain. In reference to the evolution of single-variant martensite, outlined in Section 5.2.4.1, the relevant equation is formulated linearly as,

$$\dot{\xi}_S^{SA} = H^{SA}\xi_S\frac{\dot{F}^{SA}}{F_f^{SA}}. \tag{5.46}$$

where the H^{SA} is the phase transformation activation condition defined by;

$$H^{SA} = \begin{cases} 1 & \text{if } F_s^{SA} < 0, F_f^{SA} > 0, \dot{F}^{SA} < 0 \\ 0 & \text{otherwise} \end{cases}. \tag{5.47}$$

Regarding the single-variant martensite reorientation process, the scaled transformation strain rate equation is defined as,

$$\dot{\boldsymbol{u}}^{SS} = H^{SS}\xi_S\mathbf{N}^{SS}, \tag{5.48}$$

where,

$$\mathbf{N}^{SS} = \frac{\mathbf{M}^{SS}}{\|\mathbf{M}^{SS}\|} \tag{5.49}$$

$$\mathbf{M}^{SS} = \frac{\partial F^{SS}}{\partial \boldsymbol{\tau}}. \tag{5.50}$$

F^{SS} is calculated according to equation (5.35). H^{AS} is the phase transformation acti-

vation condition defined by;

$$H^{AS} = \begin{cases} 1 & \text{if } F_s^{SS} > 0 \\ 0 & \text{otherwise} \end{cases}. \tag{5.51}$$

5.2.4.3. Kinematics and Constitutive Model. Total strain was decomposed according to equation,

$$\boldsymbol{\epsilon} = \boldsymbol{\epsilon}^e + \boldsymbol{\epsilon}^{tr}, \tag{5.52}$$

where $\boldsymbol{\epsilon}^{tr}$ is the transformation strain. Recalling equation (5.26), which relates the actual transformation strain to the scaled transformation strain multiplied by maximum residual strain, general form of constitutive equation is defined for the three-dimensional case as,

$$\boldsymbol{\tau} = \mathbf{D}_e(\boldsymbol{\epsilon} - \boldsymbol{\epsilon}_L \boldsymbol{u}). \tag{5.53}$$

In their publication [43], Auricchio elaborates on the construction of the tangent matrix and integrates it with a return-mapping algorithm for the numerical solution, taking into account the transformation conditions and the equations for transformation strain for each phase as described in this Chapter. Further details are not included in this section since the focust of the thesis is not on the constitutive modeling.

5.3. Summary of Abaqus Implementation

The Abaqus software includes a Shape Memory Alloy (SMA) material model based on the work of Auricchio [45]. This model implements the transition between austenite and martensite phases, capturing the hysteresis effect inherent to SMAs. Also, the implementation is capable of representing of inner hysteretic loop of shape memory alloy, and can accurately capture maximum change in tensile strain which is necessary for an accurate prediction of fatigue life of SMA, which is essential for their application in various engineering designs [46].

The material parameters that are required by the model are related to the Shape Memory Alloy formulation presented by Auricchio and summarized in Table 5.1.

Table 5.1. Abaqus SMA module material parameter list [45].

Material Parameter	**Definition**
Austenite Elasticty	Austenite Elasticity Modulus
Austenite Poisson's Ratio	Full Austenite Poisson's Ratio
Martensite Elasticity	Martensite Elasticity Modulus
Martensite Poisson's Ratio	Full Martensite Poisson's Ratio
Transformation Strain	Strain during the transformation from full Austenite to full Martensite
$\partial\sigma/\partial T$ Loading	Slope of the stress-temperature line
Start of Transformation Loading	Stress value that the transformation starts under tensile loading
End of Transformation Loading	Stress value that the transformation ends under tensile loading
Reference Temperature	Material testing temperature
$\partial\sigma/\partial T$ Unloading	Slope of the stress-temperature line
Start of Transformation Unloading	Stress value that the transformation starts under tensile unloading
End of Transformation Unloading	Stress value that the transformation ends under tensile unloading
End of Martensitic Elastic Regime	Rupture Point of the material

It is important to recognize the limitations associated with employing the Abaqus built-in SMA model for this study. While suitable in simulating the hysteresis loop which is a fundamental aspect for comprehending SMA behavior and make it suitable for fatigue life evaluation, the model simplifies the material's response by treating tension and compression identically. This approximation might not always reflect reality, given that SMAs typically demonstrate distinct behaviors under tensile versus compressive loading. Hence, while the model effectively captures the essential dynamics of

SMA behavior for this study, it approach of treating tension and compression might not suffice for more complicated analyses [46].

Additionally, the model's ability to account for temperature variations, as per the Abaqus implementation of Auricchio's formulation, faces limitations due to lack of input data regarding the transformation initial and final temperatures. Even though it can accurately depict superelasticity, its capability to accurately represent the shape memory effect remains uncertain. This aspect highlights a potential area for improvement, suggesting that while the model is valuable for certain applications, its representation of temperature-dependent phenomena within SMAs could benefit from further refinement to enhance its overall applicability and accuracy in simulating the multifaceted behavior of SMAs.

6. FINITE ELEMENT ANALYSIS MODELING OF ENDODONTIC FILES STRUCTURAL TEST SYSTEMS

This chapter concentrates on the finite element modeling of the ISO 3630-1 physical tests, along with the Gambarini cyclic fatigue test configuration described in Chapter 2. Moreover, it conducts cyclic fatigue simulations using the geometry of an actual molar tooth to assess the impact of real canal geometry on the endodontic instrument and the stresses exerted on tooth tissue during root canal treatment. The primary objective is to develop a comprehensive FEA methodology for the structural evaluation of endodontic instruments, focusing on their torsional and bending response as well as their fatigue behavior. Due to the availability of data in the literature, ProTaper Universal file set manufactured from conventional NiTi alloy (without special heat treatment) is utilized for the methodology development.

Abaqus software is utilized to conduct FEA and, the built-in shape memory alloy (SMA) constitutive model presented in Chapter 5 is employed for NiTi alloy. The conventional NiTi alloy material parameters from the literature are utilized for the simulations and are discussed in the detail in this Chapter.

The process starts with creating the FEA mesh for the ProTaper Universal file set, the Gambarini test configuration, and a molar tooth. Since the geometry data for the endodontic files and the molar tooth were not directly accessible, 3D X-Ray scanning was undertaken [47], and the mesh was prepared using the geometry data obtained from this scanning. For the Gambarini test configuration, where geometry data is documented in literature, the geometry was developed based on these published dimensions.

The modeling of the tooth and its mechanical properties is thoroughly explained. This includes the composition of the molar tooth model, which consists of dentin, cementum, the periodontal ligament (PDL), and bone structures. A comprehensive

literature review was undertaken to analyze the mechanical response of each tissue type. This analysis led to the evaluation of mechanical characteristics and the identification of the linear strain-stress response region for each tissue. Following this, a material property matrix was developed to support the simulation of root canal treatments. The purpose of constructing such a stiffness matrix and conducting in-depth evaluations is to explore the need for non-linear material modeling for tissues. Additionally, it examines how variations in tissue stiffness affect the endodontic instrument and the impact of the resultant stresses on the tissues themselves.

Regarding the simulation set-up of the physical tests, comprehensive (high-definition) simulation approach for the bending and torsional tests defined in the ISO 3630-1 standard [14], as well as for the cyclic fatigue tests introduced by Gambarini et al. [36] (simulated canal) are developed. The boundary and contact conditions corresponding to test set-up are defined. To enhance computational efficiency and ensure convergence robustness, idealized versions of the simulation models that feature simplified depictions of the testing apparatus were also developed.

Various simulation setups have been developed to mimic different clinical techniques for cyclic tests, incorporating both simulated canals and actual molar teeth. These setups are characterized by specific boundary conditions and procedural steps. The influence of the pecking (brushing) motion on the fatigue behavior of endodontic files is investigated using both the simulated canal and real molar tooth models. Furthermore, the effect of reciprocating motion, powered by an electric motor, on file fatigue behavior is also analyzed using the real tooth model.

For assessing the fatigue behavior of endodontic files made from conventional NiTi alloys, a brief overview of low-cycle fatigue evaluation methods is provided from the literature. The hysteresis energy approach has been identified as a reliable parameter for quantifying the fatigue behavior of Nickel-Titanium endodontic files.

The model depictions and images presented in this section are specifically created for the ProTaper Universal F2 file. However, the same methodology can be applied to simulations involving other files and file sets made from conventional NiTi alloy material.

6.1. NiTi Material Parameters

Material properties of conventional endodontic files (those without special heat treatment) are considered for the simulations. In particular, properties measured by Arruda et al. [16] from tensile tests of 1 mm Nitinol wires are used. The mechanical parameters employed in this study were obtained from the stress-strain curves provided in the literature [16] and are presented in Table 6.1.

Table 6.1. Nitinol material model parameters from quasi static test [16].

Material Parameter	**Value**
Austenite Elasticty	42.530 MPa
Austenite Poisson's Ratio	0.33
Martensite Elasticity	12.828 MPa
Martensite Poisson's Ratio	0.33
Transformation Strain	10%
$\partial\sigma/\partial T$ Loading	6.7
Start of Transformation Loading	492 MPa
End of Transformation Loading	630 MPa
Reference Temperature	22°C
$\partial\sigma/\partial T$ Unloading	6.7
Start of Transformation Unloading	192 MPa
End of Transformation Unloading	97 MPa
End of Martensitic Elastic Regime	1200 MPa

Under cyclic loading, the hysteresis curve of NiTi material evolves and stabilizes as the number of cycles increases. Therefore, the stabilized response of NiTi material

and its impact on the fatigue behavior of endodontic files present an area for investigation. In this study, the cyclic response of conventional NiTi alloy, as reported by Gu et al. [48], is used to determine the material parameters for this investigation which are presented in Table 6.1.

Table 6.2. Nitinol material model parameters from cyclic tests [48].

Material Parameter	**Value**
Austenite Elasticty	40000 MPa
Austenite Poisson's Ratio	0.3
Martensite Elasticity	30000 MPa
Martensite Poisson's Ratio	0.3
Transformation Strain	7%
$\partial\sigma/\partial T$ Loading	6.7
Start of Transformation Loading	260 MPa
End of Transformation Loading	470 MPa
Reference Temperature	22°C
$\partial\sigma/\partial T$ Unloading	6.7
Start of Transformation Unloading	235 MPa
End of Transformation Unloading	90 MPa
End of Martensitic Elastic Regime	1200 MPa

6.2. Mechanical Properties of Tooth Tissues

This section encompasses a review of the literature on the mechanical properties of dentin, cementum, the periodontal ligament, and bone structures. Following the literature review, a simulation matrix is constructed, taking into account the linear mechanical response of each tissue to conduct a thorough investigation into the material data on the fatigue behavior of endodontic files. During this investigation, the linear stiffness region of each tissue is identified and corroborated with the simulation results.

6.2.1. Dentin

Dentin, the primary component of our teeth beneath the enamel, consists of a unique combination of minerals, collagen, and water. This composition does not render the dentin as hard as enamel but significantly tougher and more flexible. The dentin has a sophisticated structure characterized by tiny channels known as dentinal tubules, surrounded by a harder substance, influencing its mechanical response. Dentin also exhibits viscoelastic behaviour, allowing it to adapt under stress and gradually return to its original shape, which is vital for enduring daily activities like chewing [49].

Although dentin tissue shows viscoelastic behaviour under static loading conditions at low rates, the fast-loading response is indicated as elastic in the literature [49]. Furthermore, Chun et al. [50] conducted various tests on canine dentin samples and reported a linear stress-strain behavior. Hana et al. [51] conducted a study on dentin tissue, performing stress-strain tests across different locations and orientations within the dentin. Their investigation revealed a variation of approximately 35% in the measured values of Young's Modulus. Rundquist et al. [52] and Ichim et al. [53], in their studies on finite element simulations of dentin tissue, adopted a linear-elastic response assumption. This approach aligns with the test results discussed in this section.

The literature presents a wide range of values for Young's Modulus for the dentin tissue. Rundquist et al. [52] and Ichim et al. [53], used a value of 14.7 GPa for Young's Modulus and a Poisson's ratio of 0.31 for their finite element models of dentin tissue. Similarly, Cheng et al. [54,55] adopted a value of 20 GPa for Young's Modulus of dentin tissue in the FEA they conducted. In their physical testing, Chun et al. [50] reported a Young's Modulus of 10 GPa from tests conducted on dentin samples from canines. Similarly, Hana et al. [51] reported that Young's Modulus for dentin tissue tests varied between 13 and 16 GPa, which accounted for different orientations of the tissue.

Therefore, based on the data from the literature, this study has chosen to adopt a range of 10-20 GPa for Young's Modulus and Poisson's ratio of 0.31 for the dentin

tissue for simulations using a realistic tooth model.

6.2.2. Cementum

Cementum is a hardened layer enveloping the tooth's root, and it stands as one of the tooth's key elements. Primarily made up of hydroxyapatite, collagen, and water, cementum combines hardness with a bit of flexibility, setting it apart from bone in terms of structure and function. Its chief function is to secure the tooth to the jawbone via the periodontal ligament, ensuring that forces from chewing are effectively transferred from the tooth to the jaw without any harm [56]. Due to its thickness, the stress-strain testing on this tissue is limited and the accuracy is questionable.

Considering the Young's modulus of cementum, Delin et al. [57] reported 2.398 GPa of average value from the test results performed on 100 samples. Hao et al. [58] studied various sections of the dry cementum and reported a linear behaviour with Young's modulus between 11.1 and 26 GPa. Considering the Poisson's ratio of cementum, the data in the literature is limited however Kamposiora et al. [59] used a value of 0.35 in their structural simulations for investigating the cement microfractures based on finite element analysis.

Thus, drawing from literature data, this study opts for a Young's Modulus range of 2.398 to 26 GPa and a Poisson's ratio of 0.35 for dentin tissue in simulations employing a realistic tooth model.

6.2.3. Periodontal Ligament (PDL)

The Periodontal Ligament (PDL) is the soft tissue that connects the tooth to the jawbone, playing a key role in carrying chewing forces and allowing the tooth to move slightly. Characterized by its unique, non-linear, and time-dependent response to physiological loads, the PDL can withstand considerable strains [60].

Despite the nonlinear characteristics of the Periodontal Ligament (PDL), this study focuses on the linear portion of the tissue's stress-strain response. It is assumed that the stresses fall within this linear range due to the forces applied by endodontic instruments during root canal treatments. This assumption will be validated through simulations using a real molar tooth model.

In the context of the Periodontal Ligament's (PDL) linear elastic material properties, Cheng et al. [54, 55] reported Young's modulus of 5 MPa, a finding that aligns with measurements obtained by Pini et al. [61] through tensile testing on bovine PDL tissues. Furthermore, Cheng et al. [54, 55] suggested a Poisson's ratio of 0.49 for the PDL.

Therefore, this study adopts a Young's Modulus of 5 MPa and a Poisson's ratio of 0.49 for the PDL tissue in simulations using a realistic tooth model.

6.2.4. Bone

Bone is characterized by anisotropic and viscoelastic properties, which are shaped by factors such as hydration, age, and environmental stress, leading to variations in its stiffness and strength. The scientific literature features a range of constitutive models designed to capture bone's mechanical behavior accurately, ranging from simple linear elastic models to more sophisticated ones. These models highlight bone's capacity to adapt, emphasizing the crucial role of the interplay between mechanical forces and biological responses, especially in the field of dentistry. It is noted that moisture level is a primary determinant of bone's response as either linear or nonlinear. For the purposes of this study, bone tissue is assumed to exhibit linear elastic and isotropic behavior, based on the stress levels typically encountered during endodontic treatment [62].

In their research, Cheng et al. [54, 55] suggested Young's Modulus of 14 GPa and Poisson's ratio of 0.15 for alveolar bone, which they employed in their study of root canal stresses across different canal preparation techniques through finite element

analysis. This study similarly adopts these values for the simulation of a real molar tooth model.

6.2.5. Material Property Matrix

Table 6.3 has been constructed to account for variations in Young's Modulus of each tissue, under the assumption of a linear elastic material response shown in Table 6.3. This matrix is applied in the simulation models of a real molar tooth. Through these models, the study examines how variations in the Young's Modulus of each tissue affect the outcomes related to the file as well as the stress data on the molar tooth, as detailed in Section 7.4. This analysis aids in determining which tissues is required to be included in the model and the level of material detail necessary for accurate root canal treatment simulations. In order to understand the rigid behaviour of the tissue, material matrix also includes the ''Stiff" material response of each tissue which is provided by introducing comparably larger Young's modulus : 2.100.000 MPa.

Table 6.3. Material properties for different tissues in the simulation models.

Simulation Model Name	Material Properties (MPa)			
	Dentin	Cementum	PDL	Bone
Dentin 1	20000	Stiff	Stiff	Stiff
Dentin 2	1500	Stiff	Stiff	Stiff
Dentin 3	10000	Stiff	Stiff	Stiff
Stiff	Stiff	Stiff	Stiff	Stiff
Cemnt. 1	15000	1287	Stiff	Stiff
Cemnt. 2	15000	15000	Stiff	Stiff
PDL 1	Stiff	Stiff	50	Stiff
PDL 2	15000	18500	50	Stiff
F. Flex	15000	18500	50	14000

6.3. Finite Element Model Development

In this section, details are provided on meshing and the development of high-definition simulation models for ISO 3630-1 test configurations described in Section 4.1, along with configurations for cyclic fatigue simulations (simulated canal and real molar tooth). Additionally, simplifications for the test configurations are proposed. First, the mesh development details are presented, followed by an overview of the model development approach.

6.3.1. Geometry and Mesh Development

6.3.1.1. Gambarini Test Apparatus. The finite element model of the apparatus was defined based on the geometry provided in the literature [36] and meshed with first-order brick elements. The jig and the cylinder were modeled as separate components. They were assembled to create canal geometry as illustrated in Figure 6.1. Linear elastic steel material properties with Young's modulus of 210 GPa and Poisson's Ratio of 0.3 were assigned to both components.

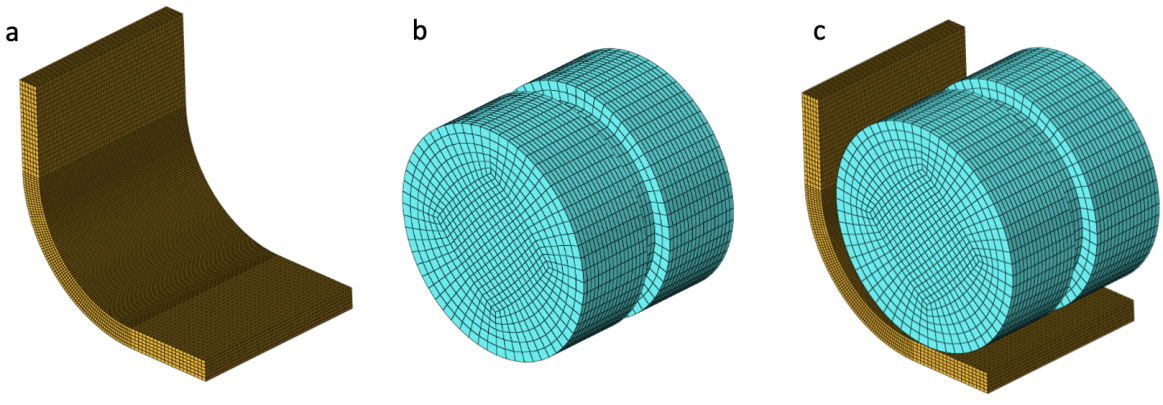

Figure 6.1. Solid FEA model of Gambarini test apparatus; a)Jig, b)Cylinder, c)Assembled model.

6.3.1.2. Rotary Endodontic Files. The process of acquiring the endodontic file's geometry began with a 3D scan of the file within a Micro Computed Tomography (MicroCT)

scanner Skyscan 1275, accompanied by the utilization of 3D reconstruction software NRecon [47]. The scanner generated images of the endodontic file's geometry in TIFF format, and subsequently, the NRecon software was employed to transform these TIFF images into BMP format. The next stage involved the utilization of open-source software 3D Slicer [63], to combine the BMP images into a single STL geometry data file, which defined the resultant 3D surface illustrated in Figure 6.2.

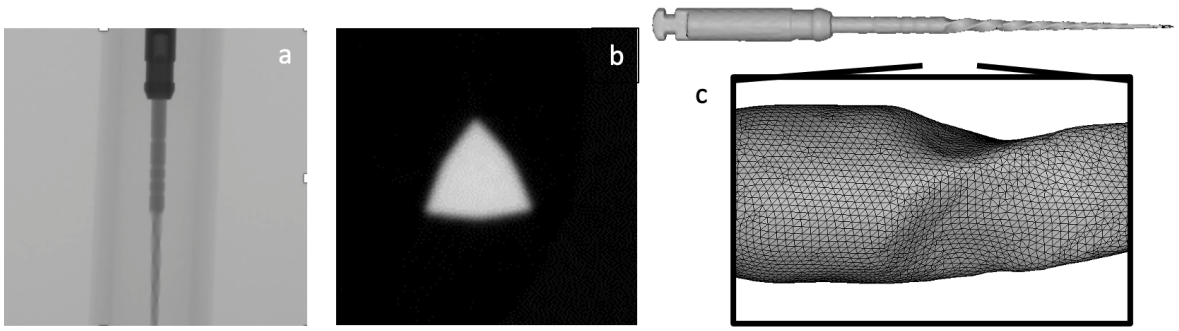

Figure 6.2. PTU F2 file geometry scanning steps: a) An illustration of geometry stored as TIFF image; b) An illustration of geometry stored as BMP image; c) STL triangulated surface geometry stored as a single STL geometry .

The final STL file contained the 3D surface of the endodontic file, defined by triangular elements. Once the STL geometry file was generated, it was imported into finite element pre-processor software and subjected to the following examination:

- Identification of free surface edges arising from potential imperfections in the scanning process.
- Assessment of geometric details that could be omitted from the analysis to reduce the model's size therefore to reduce the analysis time.

After the geometry was reviewed and corrected, AutoDesk Fusion 360 [64] was employed to derive surface data from the STL geometry file. In the final phase, the resultant surface geometry of the endodontic file was partitioned into 40 segments by

parallel planes perpendicular to the endodontic file's axis, and the cross sections were defined. Finally, a 2D surface mesh was constructed on each cross section and swept along the endodontic file's axis to form first order hexahedron solid elements depicted in Figure 6.3.

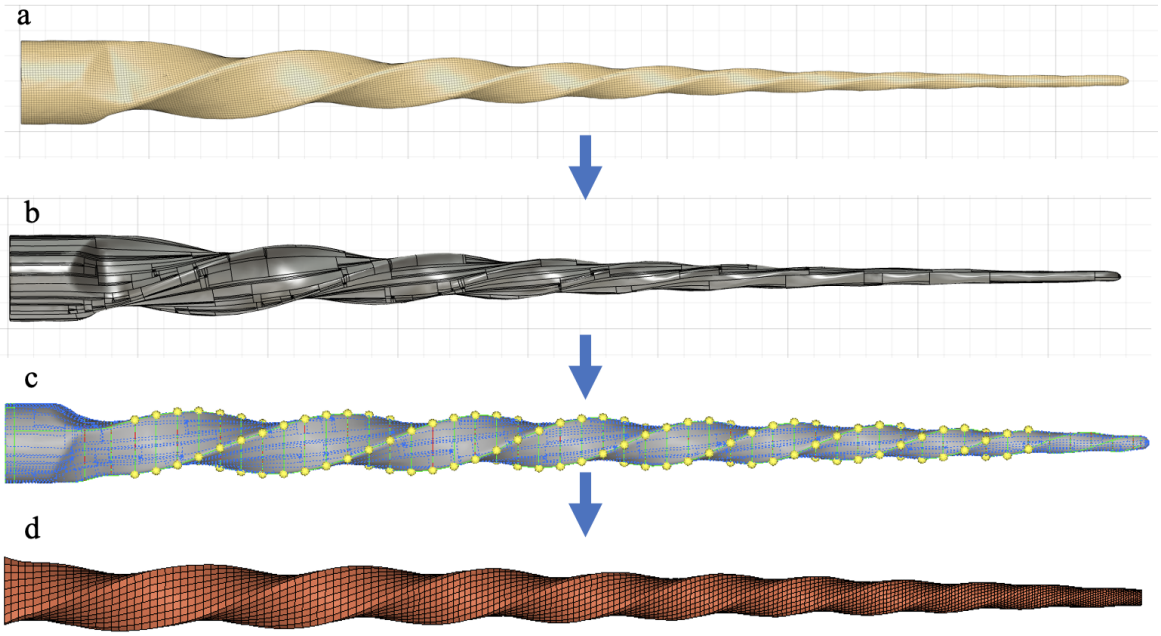

Figure 6.3. PTU F2 file geometry processing stages: a) STL representation; b) Surface geometry defined by AutoDesk Fusion 360; c) 3D surface partitioned by parallel planes; d) Final 3D Solid Mesh .

6.3.1.3. Molar Tooth. The mesh development procedure for the molar tooth, similar to that used for the endodontic files, started with the scanning process. A molar tooth characterized by a significant canal curvature was deliberately chosen and scanned using the Skyscan 1275 where the process steps are illustrated in Figure 6.4. It's worth noting that the scanner's resolution of 4 μm/px was found to be more than adequate for capturing the intricate details of the root canal.

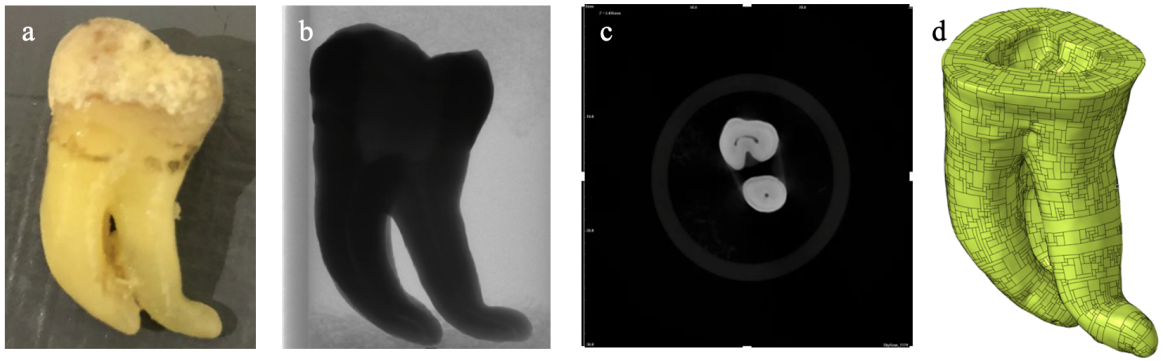

Figure 6.4. Tooth scanning steps a) Scanned molar tooth, b) TIFF image sample, c) BMAP image sample, d) Surface data.

In order to develop a finite element model of the root canal, the 3D surface created from data obtained with 3D-scanning of the molar required further processing. First, the outer surface of the molar and the surfaces of the root canal were separated, and redundant surface edges and not relevant features were deleted, in order to control the mesh quality as shown in Figure 6.5.

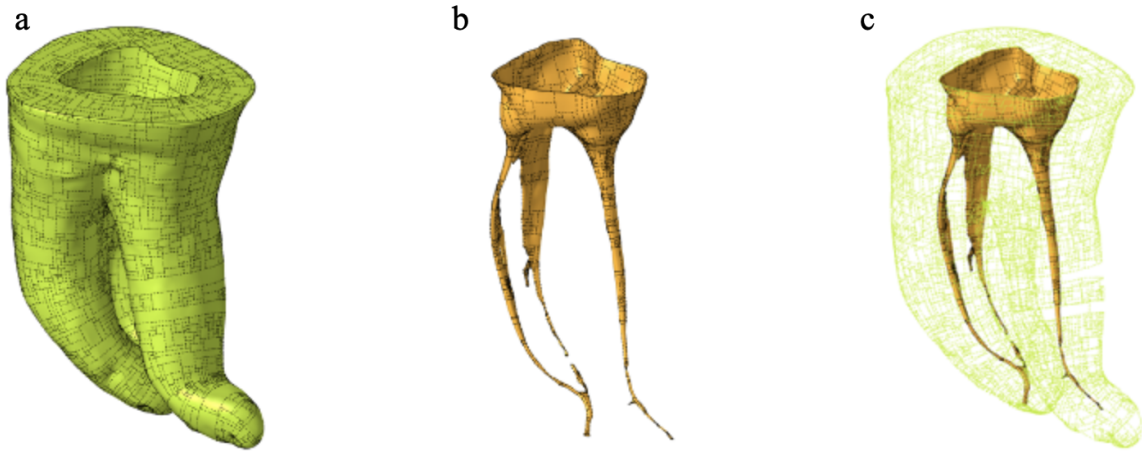

Figure 6.5. Tooth geometry processing; a) Outer surface, b) Canal geometry, c) Combined view.

Since the scanned molar had not been subjected to root canal treatment, further processing of the geometry was required. Among the three scanned molar root canals, the one with the maximal curvature was selected. In order to simulate a root canal subjected to an endodontic procedure, the selected root canal was reconstructed by increasing its diameter to 1.2 mm at the coronal section and tapering it down to 1 mm at the apical section, while maintaining the original curvature and path as illustrated in Figure 6.6. These diameters were selected based on the studies performed by Martos et al. [65] and Razumova et al. [66]. The final geometry of the reconstructed root canal was used in the simulation.

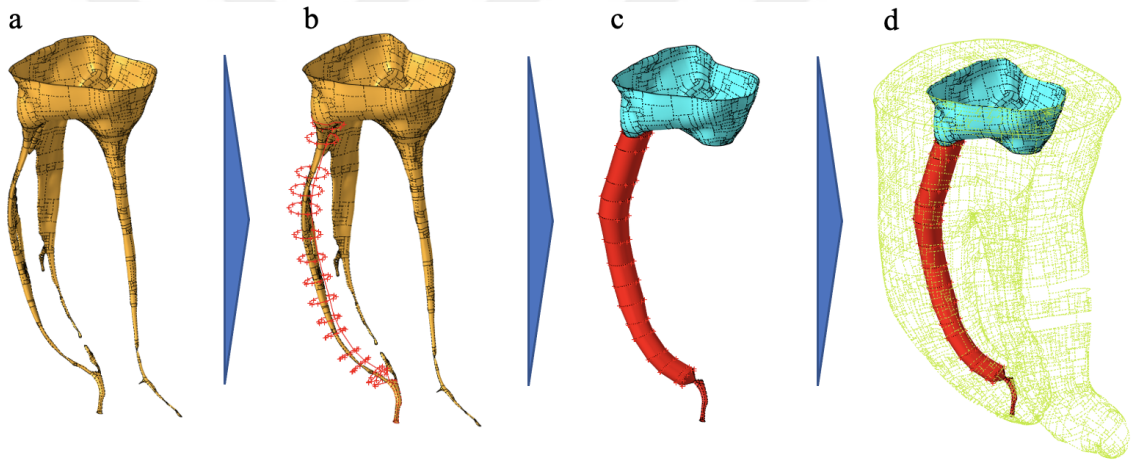

Figure 6.6. Canal geometry reconstruction steps; a) Original geometry, b) Path and curvature identification, c) Surface construction, d) Combined view.

Finite element mesh was created for the final geometry. Since the geometry included only the dentin section, cementum, and PerioDontal Ligament (PDL) layers were introduced based on the average thickness data from the literature. Cementum thickness was defined as 50 microns according to [67], and PDL thickness was defined as 250 microns according to [68]. The tetrahedron elements were utilized for dentin, PDL, and bone, whereas the cementum was represented with the second order triangular shell elements as depicted in Figure 6.7.

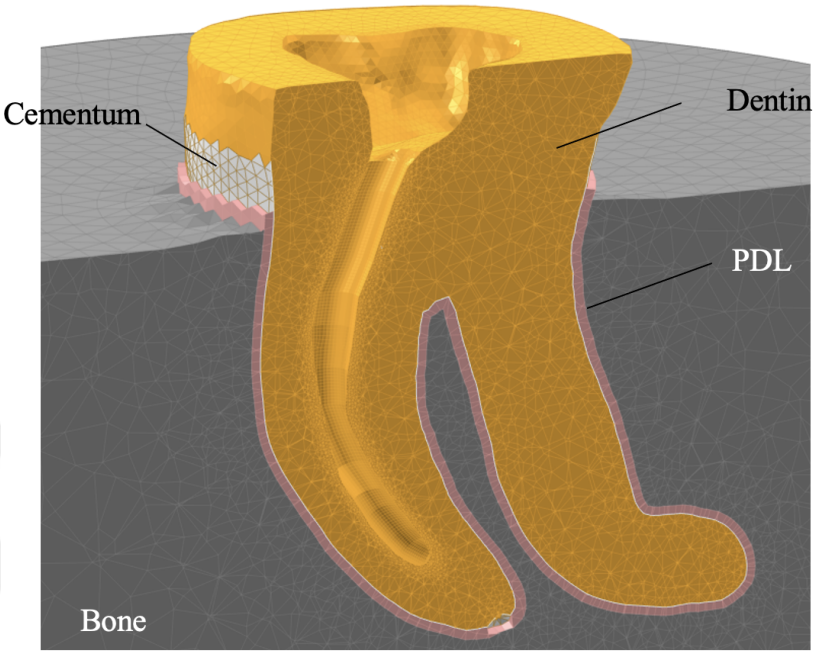

Figure 6.7. Finite element mesh for the tooth.

6.3.2. Loading, Boundary and Contact Conditions

Two models were constructed for the test configurations described in Chapter 4: a high-definition model and an idealized model. The high-definition model provides a comprehensive and detailed representation of the test configuration, while the idealized model offers a simplified representation, where loading and fixation conditions are streamlined to reduce computational and modeling time.

6.3.2.1. ISO 3630-1 Bending Test. A high-definition bending test simulation shown in Figure 6.8 incorporates the file as well as the catch pin. The idealized version of the model is depicted in Figure 6.9 where the catch-pin is simulated by force boundary conditions. The catch pin is meshed with first order 3D brick elements. Contact is defined between the pin and the file handle as hard contact in the normal direction and frictionless in the tangential direction.

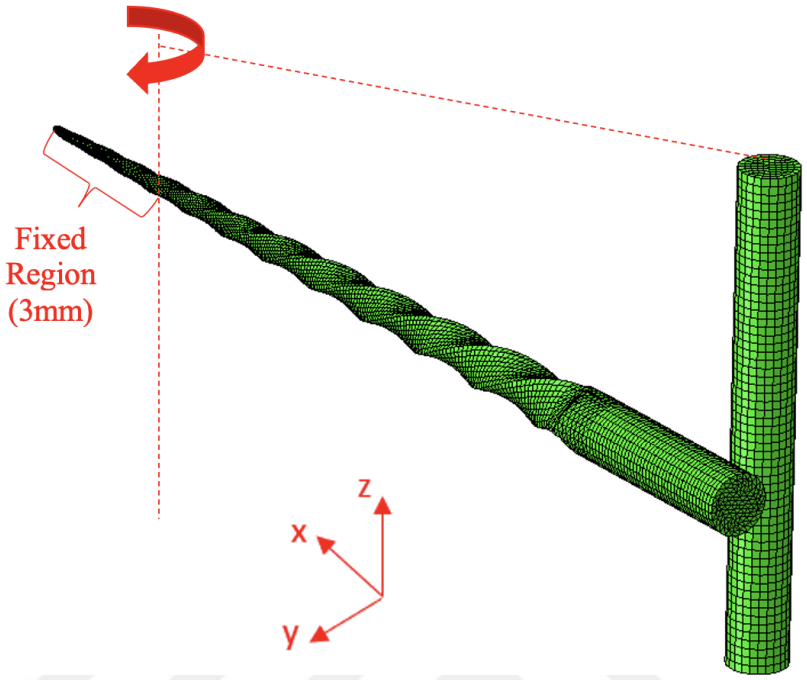

Figure 6.8. Bending test high definition model.

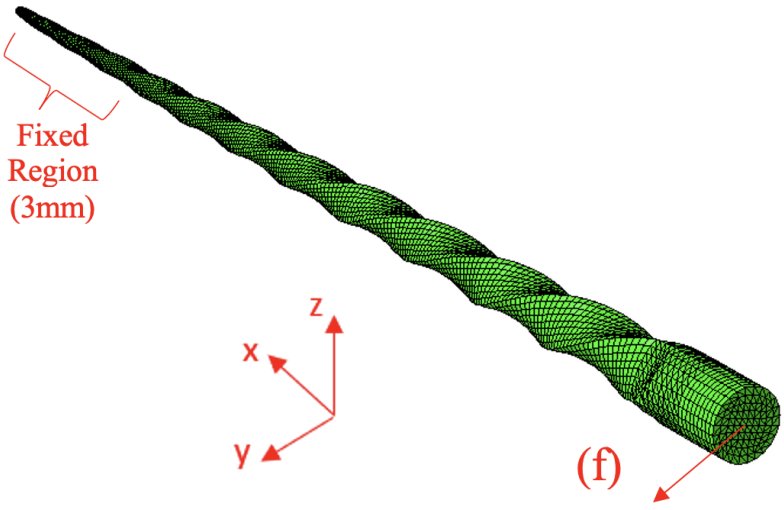

Figure 6.9. Bending test idealized model.

Regarding the boundary conditions for the high-definition model, all degrees of freedom for the surface nodes within 3 mm from the tip of the endodontic file are constrained. The pin is connected to the center of rotation, which is positioned 3 mm

from the tip of the file, via kinematic coupling [45]. Following the initial contact with the file handle the catch-pin is rotated 45 degrees around the rotation axis.

For the boundary conditions of the idealized model, in order to simulate the catch-pin replacement, a force is applied at the independent node of a kinematic coupling constraint located at the handle axis where the initial contact with the catch pin is observed. The force follows the nodal rotation until the rotation of the handle reaches 45 degrees when the simulation is ended.

6.3.2.2. ISO 3630-1 Torsion Test. The torsion test model consists only of the endodontic file as shown in Figure 6.10.

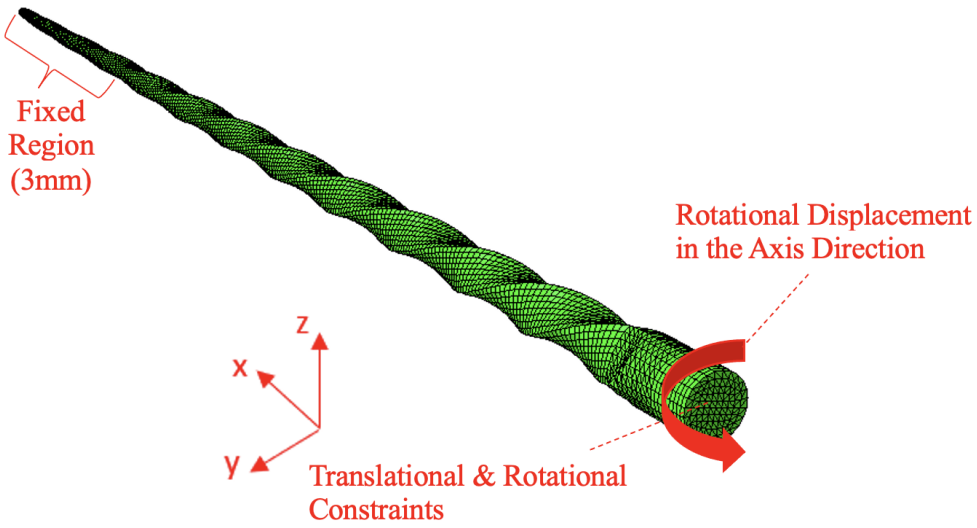

Figure 6.10. Torsion test high definition model.

Surface nodes of the endodontic file within 3 mm of the tip are fully constrained. Constraints are imposed on the handle section using kinematic coupling to restrict its translational and rotational degrees of freedom, except for the axial rotational direction, where rotational displacement is defined. Twisting motion on the handle is simulated by applying rotational displacement to the reference point defined for kinematic coupling constraint. This rotational displacement is applied until the twisting

moment reaches 3 Nmm, following the approach by de Arruda et al. [16].

Considering the boundary conditions for idealized model, the displacement constraints at the handle side are removed, allowing unrestricted movement of the handle in all directions.

6.3.2.3. Gambarini Test Apparatus and File. The high-definition model includes an endodontic file, jig part with 90 degrees curvature and 6 mm radius, and a cylinder part with a groove of 5 mm radius and 1.5 mm width as shown in Figure 6.11. Linear elastic material model for steel with 210 GPa Young's modulus and 0.3 Poisson's ratio is used for the jig and the cylinder. The cylinder and the jig are modeled with first order brick elements whereas the file is modeled as described in 6.3.1.2.

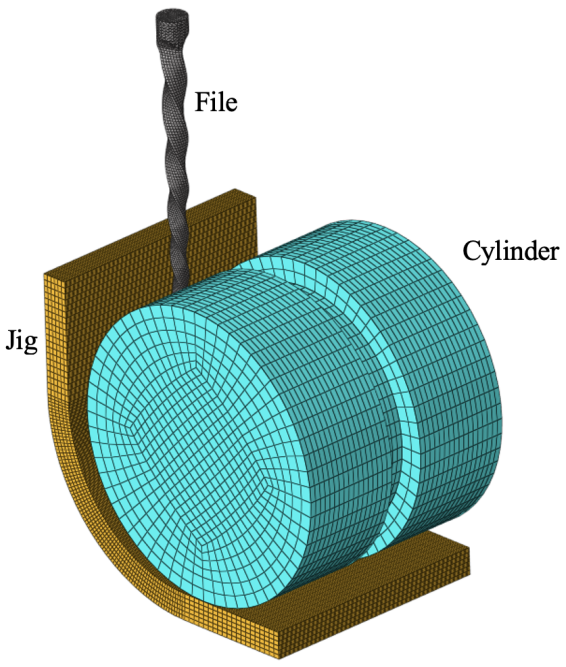

Figure 6.11. Gambarini test apparatus and endodontic file.

The prescribed displacement boundary conditions are applied to the endodontic file's end surface via kinematic coupling. The jig and the cylinder's outer surfaces are fixed.

Surface to surface contact with finite sliding is defined between the endodontic file and the jig as well as the endodontic file and the cylinder groove. Considering that the system is lubricated with oil during the test, the tangential behavior of the contact is defined as frictionless. The normal contact behavior is defined using pressure overclosure algorithm with linear constraint enforcement method with contact stiffness 10000 $N/mm/mm^2$.

For the the idealized model, considering that the test apparatus components (jig and cylinder) are made of steel, which is 5 times stiffer than NiTi, the deformation of the apparatus is estimated to be negligible as compared to that of the endodontic file. Consequently, the simulated canal formed by the apparatus geometry is developed by analytical rigid surfaces as depicted in Figure 6.12.

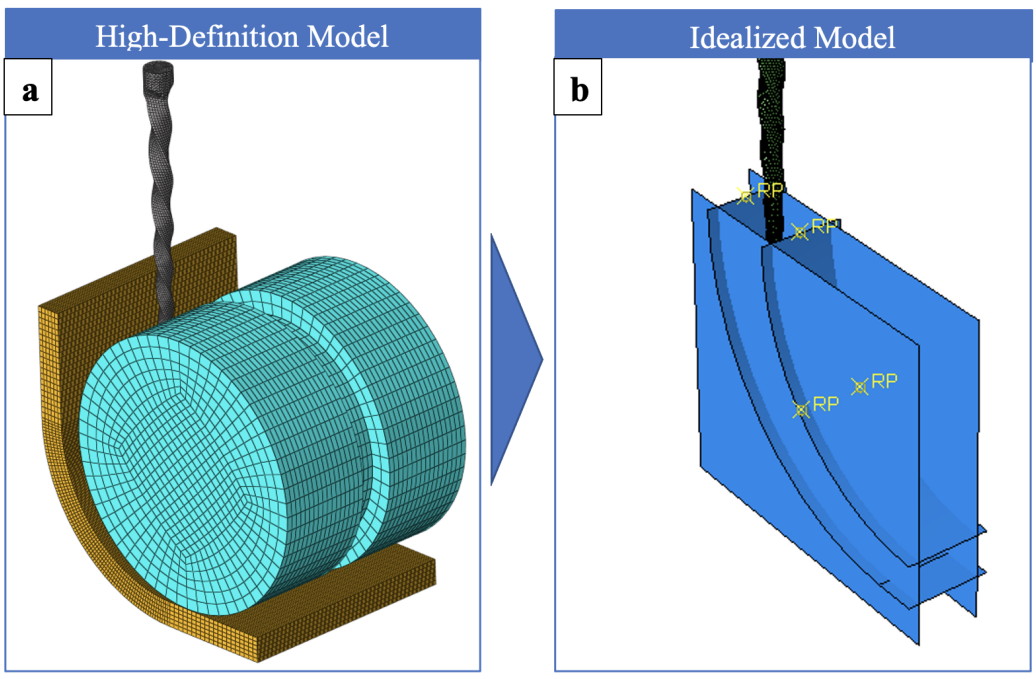

Figure 6.12. Cyclic fatigue test configuration model
(a) High-Definition model, (b) Idealized model .

The steps for the cyclic fatigue simulation, where the file is maintained in a fixed axial position and afterwards applying a pecking motion which is described in Section

3.1.2, are outlined as follows:

(i) Endodontic file insertion: The file is inserted to a depth of 22 mm from the top of the jig as parallel to the test configuration described in Section 4.2.

(ii) Endodontic file rotation: After insertion, the file's axial position is fixed, and it is rotated around its axis until the dissipated energy stabilize. This configuration represented the test conditions performed by Fife et al. [37].

(iii) Endodontic file rotation with pecking motion: The endodontic file was rotated for a total of 1500 degrees while performing one pecking cycle of 4 mm axial displacement. This configuration represented the test performed by Whipple et al. [38].

6.3.2.4. Molar Tooth and Endodontic File. To analyze the fatigue behavior of endodontic files subjected to bending caused by the realistic curvature of a tooth canal during root canal procedures, a model incorporating an actual molar tooth and the endodontic file has been developed.

The following components were included in the simulation as shown in Figure 6.13,

- Endodontic file utilizing Abaqus built-in constitutive model for shape memory alloy
- Dentin tissue, with material response defined by a linear elastic constitutive model
- Cementum layer, with material response defined by a linear elastic constitutive model
- Periodontal ligament (PDL) layer, with material response defined by a linear elastic constitutive model
- Bone, with material response defined by a linear elastic constitutive model

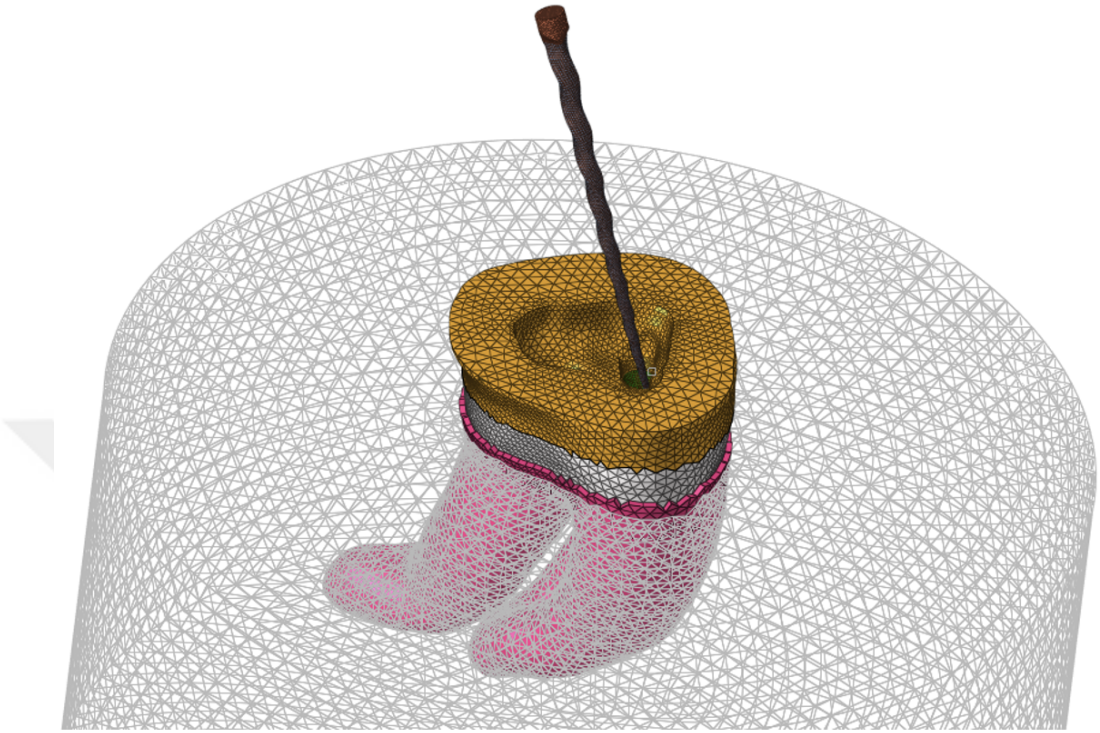

Figure 6.13. Finite element model of molar tooth and PTU F2 file.

Regarding the material properties of the tooth tissue, based on the literature review performed in section 6.2, the average Young's modulus values are utilized for the cyclic fatigue simulations as depicted in table Table 6.4.

Table 6.4. Tooth tissue material properties.

Material	**Young's Modulus (MPa)**	**Poisson's Ratio**
Dentin	20000	0.31
Cementum	2398	0.35
PDL	50	0.49
Bone	14000	0.15

Same contact conditions are utilized as described in section 6.3.2.3, assuming the file is not subjected to large amount cutting resistance. The contact was defined between the file and the dentin outer surfaces.

The steps for the cyclic fatigue simulation, where the file is maintained in a fixed axial position and afterwards a pecking motion is applied, are quite similar to the version where a Gambarini test configuration is utilized as described in Section 6.3.2.3, and can be outlined as follows:

(i) File insertion: The file was inserted 12 mm deep, which corresponded to the file tip being placed at the tooth apical section.

(ii) Rotation without axial displacement: After the file was inserted, the axial position of the file was maintained, and it is rotated around its axis until the dissipated energy stabilize. This configuration represented the test conditions performed by Fife et al. [37].

(iii) Endodontic file rotation with pecking motion: The endodontic file was rotated for a total of 1500 degrees while performing one pecking cycle of 4 mm axial displacement. This configuration represented the test performed by Whipple et al. [38]

The reciprocating motion, described in Section 3.2.1, is simulated using the real molar tooth model, which accommodates a canal geometry with an oval cross-section, as opposed to the Gambarini setup that features a rectangular cross-section.

Reciprocating motion with the following configuration is performed illustrated in Figure 6.14

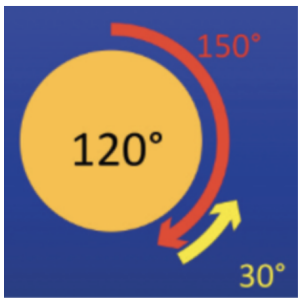

Figure 6.14. Reciprocating motion configuration.

Simulation steps can be presented as follows;

(i) File insertion: The file was inserted 12 mm deep, which corresponded to the file tip being placed at the tooth apical section.
(ii) Rotation without axial displacement: The approach was similar to Gambarini's test-bench simulation. After the file was inserted, the axial position of the file was maintained, and it is rotated around its axis until the dissipated energy stabilize.
(iii) Endodontic file reciprocating motion (Cutting motion): The endodontic file was rotated for a total of 150 degrees while the axial position is fixed.
(iv) Endodontic file reciprocating motion (Release motion): The endodontic file was rotated for a total of 30 degrees while the axial position is fixed.

6.4. Low Cycle Fatigue Approach

In evaluating the low-cycle fatigue life and behavior of NiTi alloys, the literature presents a range of methodologies which may be grouped into three categories: stress-based, strain-based, and energy-based approaches. Stress-based methods focus on the stresses experienced by the material under cyclic loading, while strain-based approaches consider the deformation the material undergoes. Energy-based methods, on the other hand, analyze the energy dissipated during the loading cycles. Each of these methods provides a unique lens through which the fatigue behavior of NiTi alloys can be understood, catering to different aspects of material response under cyclic stress and strain conditions. This comprehensive review highlights the diversity of techniques available for assessing the durability and performance of NiTi alloys, which are critical to their application in various engineering and medical fields.

Considering stress-based methods, Scattina et al. [26] have employed this traditional approach by conducting calibration and applying it to various file sets to estimate fatigue life and behavior, validating their findings with test data. On the other hand, Figueiredo et al. [69] notes that, while foundational, such methods may not fully encompass the unique properties and behaviors of Nitinol under multiaxial

loading conditions. The traditional approaches might not effectively capture the complex deformation mechanisms, including phase transformations, that are intrinsic to Nitinol's superelasticity and shape memory effects.

Strain-based methods are increasingly emphasized by researchers. Runciman et al. [70] focused on predicting the fatigue life of superelastic Nitinol medical devices under multiaxial loading conditions, encountered by devices like endovascular stents. Recognizing the limitations of traditional uniaxial loading-based methods in accurately forecasting device lifespan due to Nitinol's complex loading scenarios in actual use, their study contributes significantly to the field. By performing torsional fatigue tests on thin-walled Nitinol tubes and employing a strain-based, in particular equivalent strain/Coffin-Manson approach, they proposed a novel model for predicting life under multiaxial stress. While the method is effective for estimating the fatigue life of stents over thousands of cycles, its accuracy diminishes for endodontic files, which operate in a lower cycle regime.

Energy-based methods are a key approach in evaluating the low-cycle fatigue behavior of NiTi alloys. Moumni et al. asserted that the hysteresis energy per cycle holds significance in estimating the low cycle fatigue life of Shape Memory Alloys due to the stabilizing trend observed in the hysteresis curve after multiple cycles [71]. Specifically, in the case of uniaxial loading, the count of cycles until failure is determined by the dissipated energy, as measured from hysteresis curves. Moumni et al. [72] have validated this proposed approach in scenarios involving torsional loading. Furthermore, Gu et al. [48] have extended this methodology to cases of multiaxial loading.

Based on the findings from the reviewed literature, the dissipated energy proves to be a convenient parameter for assessing the fatigue life of endodontic files, which are commonly subjected to intricate loading patterns. It is important to note that different endodontic file sets are typically manufactured from various NiTi alloys and undergo different heat treatments. Hence, establishing a calibrated relationship between dissipated energy and fatigue life is necessary. The computed hysteresis energy can also be

used for comparison of different endodontic file designs made from the same material or evaluating various surgical techniques applied to an identical configuration.

In the current study the dissipated energy density, also referred to as hysteresis energy density, has been employed to predict the overall fatigue behavior of endodontic files manufactured from conventional alloys, and to identify the location of failure. Currently, the hysteresis energy is used for comparison purposes, while the calibration of the relationship between dissipated energy and fatigue life is not within the scope of this study.

7. RESULTS

7.1. ISO 3630-1 Simulations

The methodology for developing ISO test systems models is validated by examining the ProTaper Universal F1 and F2 files described in Section 1.3. The outcomes of these files are compared against one another. Moreover, a comparison between the results of idealized models and high-definition models is carried out to evaluate the effectiveness of the idealization approach for each test system. Ultimately, validation is based on the test data provided by Arruda et al. [16].

7.1.1. Bending Test

The following parameters were evaluated for the bending test results: the bending moment versus the cath-pin torque, the handle tip displacement during bending, the von Mises stress distribution on the file, and the overall bending stiffness of the file, which is the ratio bending moment applied to the resulting bending angle of an instrument.

High definition and idealized model deformed configurations of PTU F1 endodontic file are shown in Figure 7.1 and Figure 7.2, respectively. For PTU F1 and F2 endodontic files, tip displacement and von Mises stress distributions are summarized in Table 7.1 and Table 7.2.

For F1 endodontic file, the idealized model tip displacement is within 0.21% of that of the high definition model. Maximum von Mises stresses differ by about 0.9%. Bending moments are identical in both high definition and idealized models with excellent agreement with the test data reported in Arruda et al. [16] as compared in Figure 7.3.

A similar trend is observed for the F2 endodontic file. Bending moments match in both models with 7.85 Nmm at 45 degrees of bending angle. In the high definition model, the handle tip displacement is within 48% of that of the high definition model. Maximum von Mises stresses differ by about 2.4%.

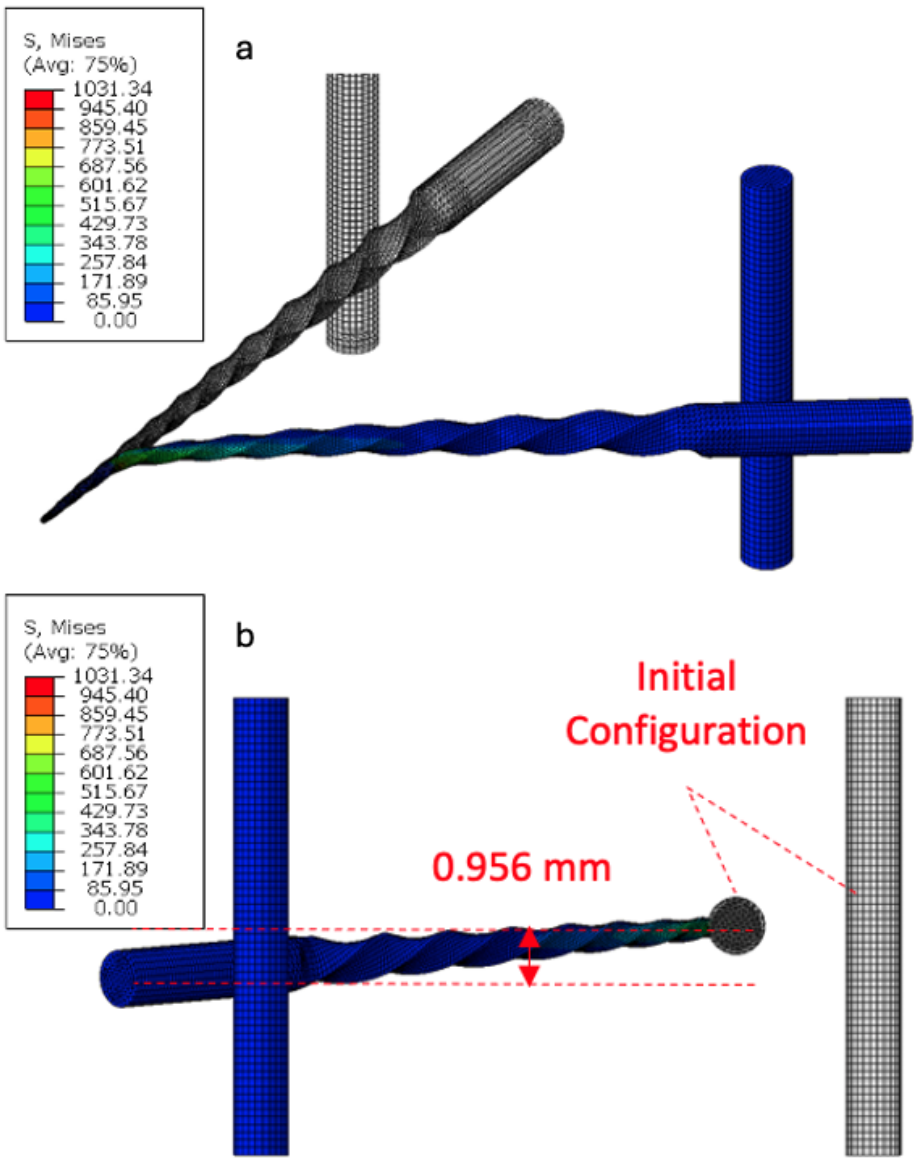

Figure 7.1. F1 endodontic file bending test high definition model results (a) Isometric View, (b) View in the axial direction .

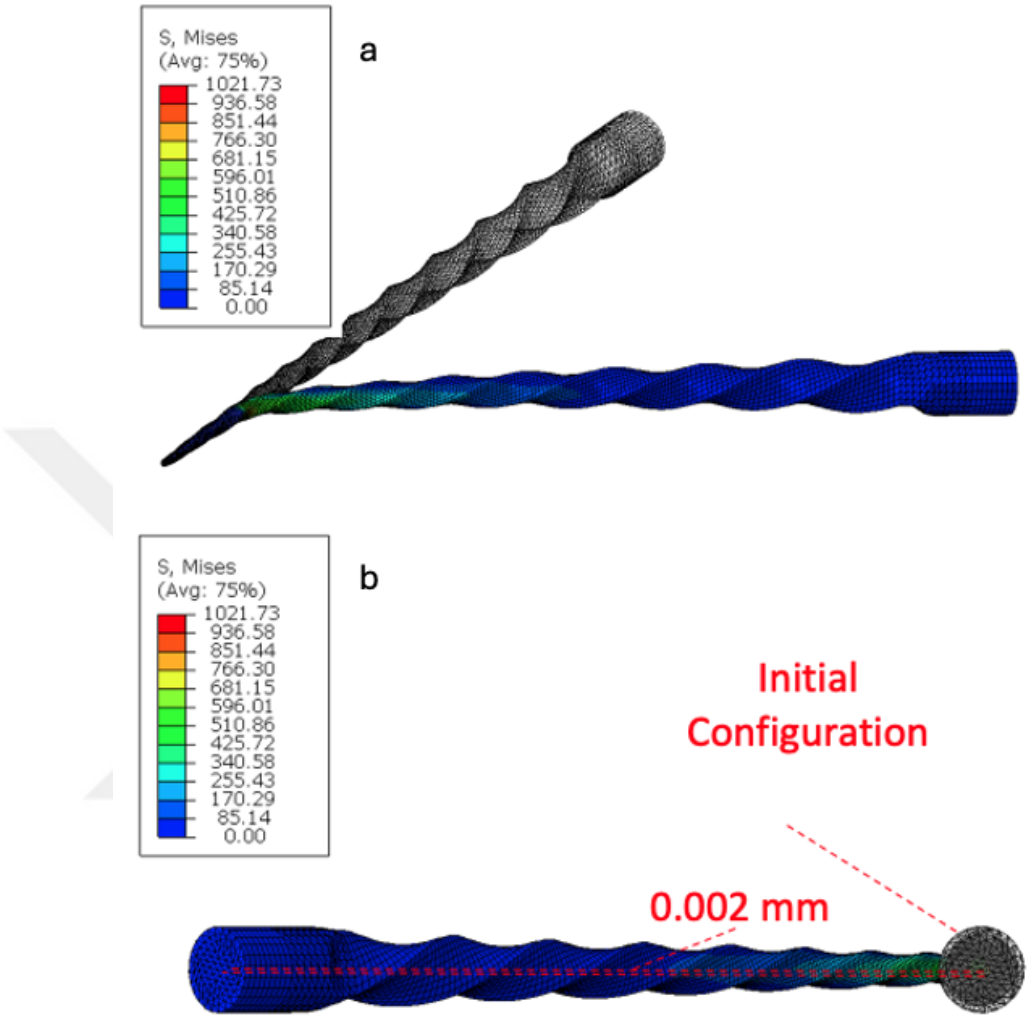

Figure 7.2. F1 endodontic file bending test idealized model results (a) Isometric view, (b) View in the axial direction.

Table 7.1. Comparison of maximum handle tip displacement between high definition and idealized models.

File	High Def. Model	Idealized Model	Difference (%)
PTU F1	0.956 mm	0.002 mm	0.21
PTU F2	0.473 mm	0.229 mm	48

Table 7.2. Comparison of maximum von Mises stress between high definition and idealized models.

File	High Def. Model	Idealized Model	Difference (%)
PTU F1	1031.34 MPa	1021.73 MPa	0.9
PTU F2	1211.20 MPa	1239.91 MPa	2.4

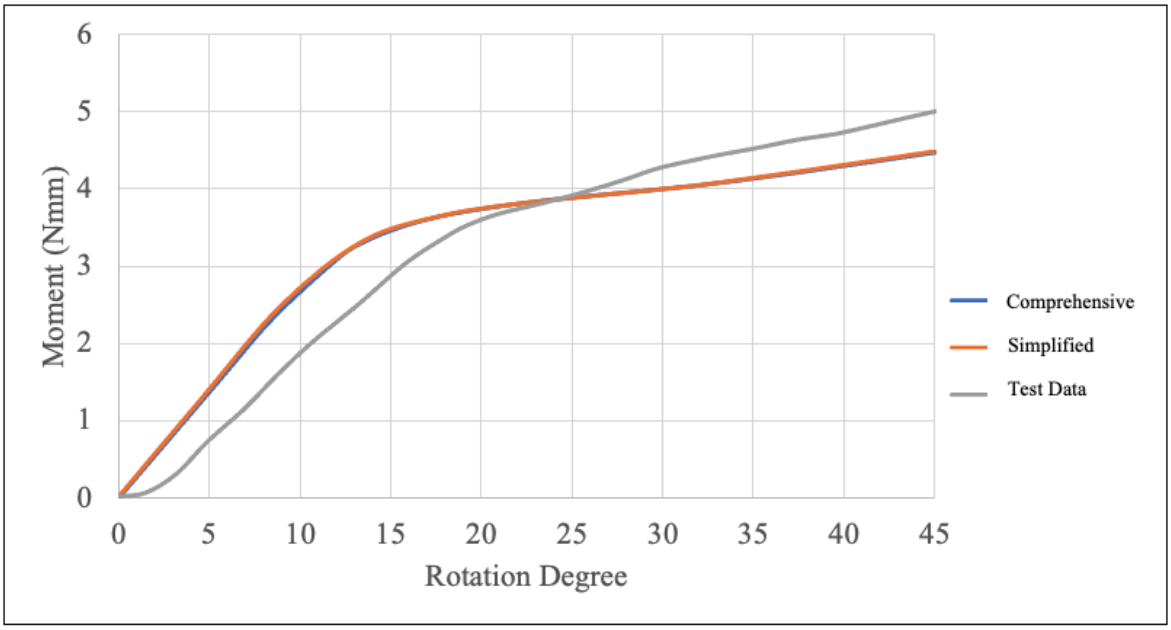

Figure 7.3. Bending moment for F1 endodontic file

7.1.2. Torsion Test

For the torsion test, the evaluated results are as follows: the handle rotation versus the applied torque, the von Mises stress distribution on the file, and the overall torsion stiffness of the file, which is the ratio of applied torque to the resulting angle of twist, using a torque testing apparatus.

It is observed that for PTU F1 and F2 endodontic files, the high-definition and idealized models provided identical results when the torque reached a value of 3 Nmm. Additionally, for the F1 endodontic file, the maximum von Mises stresses are 27% higher

than those for the F2 file, as shown in Figure 7.4. The handle rotation prediction for F1 endodontic files is in excellent agreement with the test data provided by Arruda et al. [16], as compared in Figure 7.5. It is also observed that by the end of the simulation, the F1 handle rotates 68% more than the F2 file handle, as shown in Table 7.3.

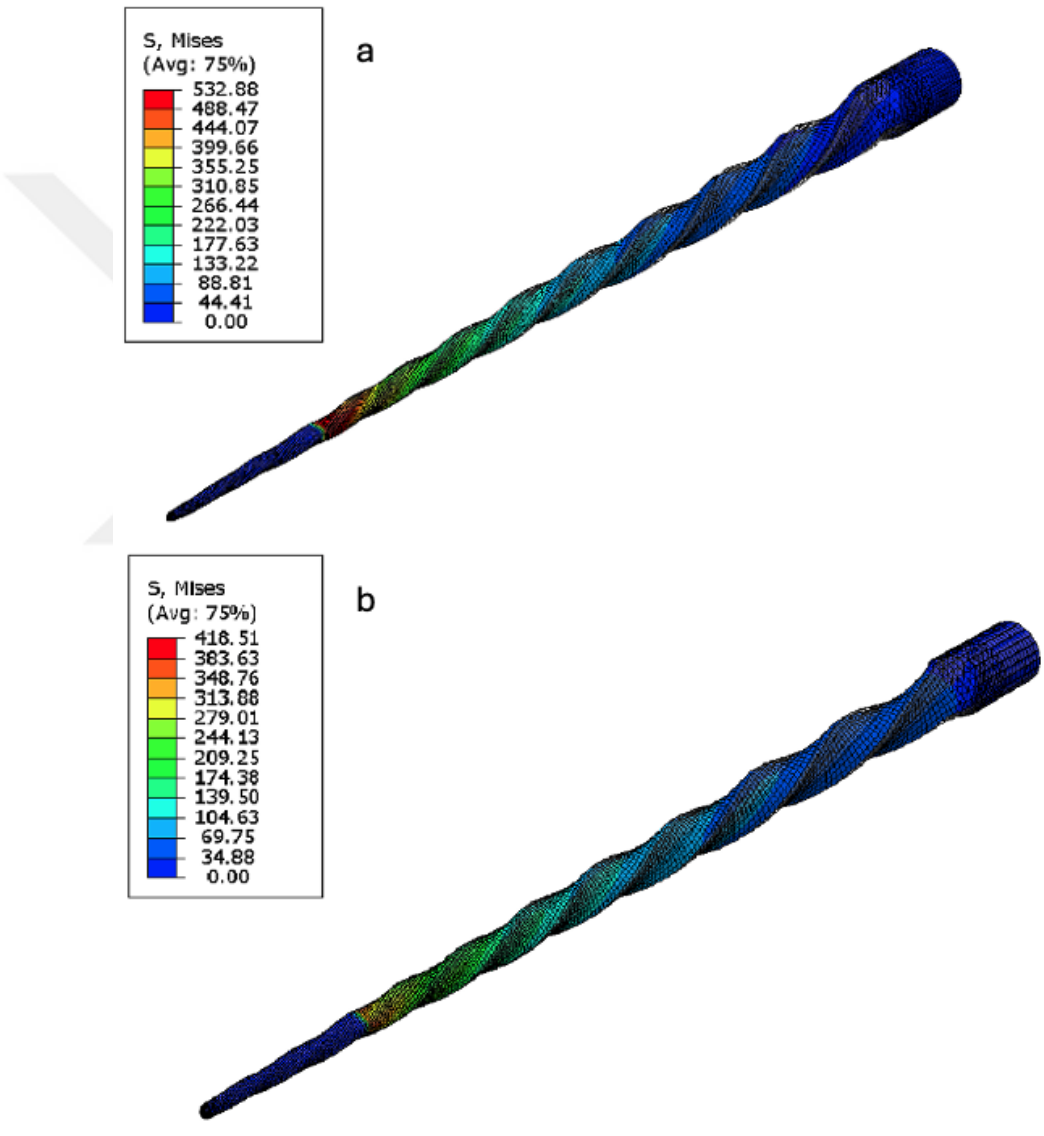

Figure 7.4. Torsion simulation results for F1 and F2 endodontic files (a) PTU F1, (b) PTU F2 .

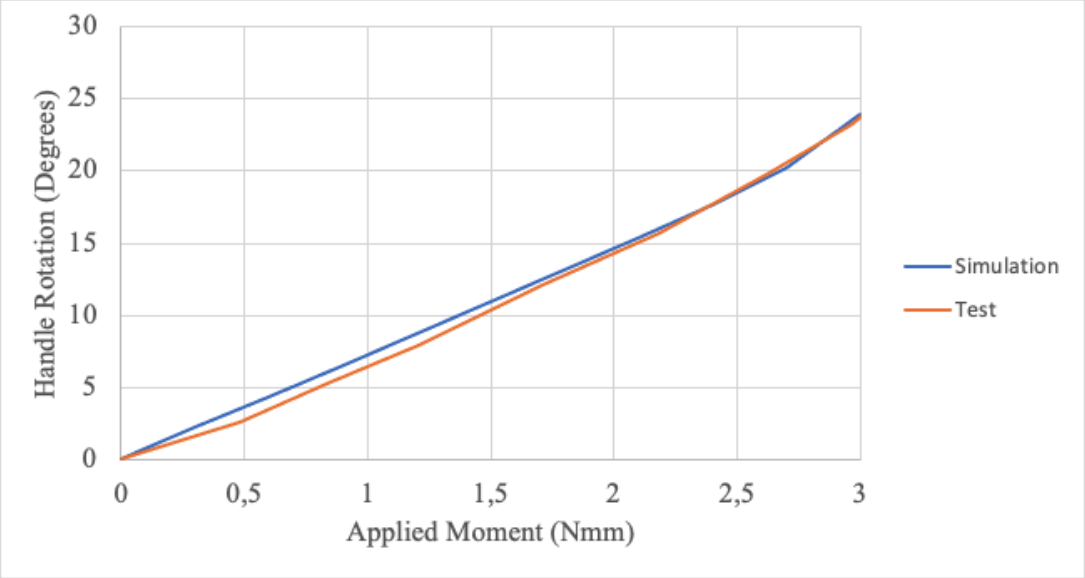

Figure 7.5. F1 endodontic file torsion simulation results .

Table 7.3. Comparison of handle tip rotation.

File	FEA Result
PTU F1	23.25°
PTU F2	15.81°

7.1.3. ISO 3630-1 Test Results Discussion

The high definition model described for the bending test demonstrates results that exhibit a reasonable correlation with the physical test outcomes reported by de Arruda et al. [16], particularly concerning the bending moment estimates for the F1 endodontic file. This agreement extends to the torsion tests, where the simulation outcomes closely align with the test results, reported by de Arruda et al. [16]. Furthermore, the simulation results confirm that the outcomes obtained from the idealized models show a high level of accuracy when compared to the results from the high-definition models. While the horizontal displacement of the handle due to the geometric stiffness of the file is underestimated by the idealized models, it does not impact the calculated bending moment results. In summary, this validation confirms that the proposed methodol-

ogy using high-definition models is suitable for assessing the structural stiffness of the endodontic files, and the suggested idealizations are indeed appropriate.

Another noteworthy result is that the F1 endodontic file has approximately 57% less torsional stiffness and 68% less bending stiffness in comparison to the F2 file. Again, these findings align with the test data presented by Camara et al. [17].

7.2. Cyclic Fatigue Simulations

Cyclic loading simulations were performed using both the Gambarini test Apparatus and a real molar tooth. The dissipated energy density results and their peak locations were evaluated to assess the low-cycle fatigue failure behavior and failure location, respectively.

In the Gambarini test configuration, ProTaper Universal F1 and F2 files are simulated in a fixed axial position. The outcomes are validated against test data from the literature, notably from Fife et al. [37] and Whipple et al. [38]. This validation targets the overall fatigue behavior, including both the failure location and the relative dissipated energy density. The effect of the pecking motion on the F2 file is also examined, with validation based on data from existing studies. Furthermore, the role of the NiTi alloy's stabilized material parameters on the hysteresis energy effect is scrutinized, with a focus on the F2 file. Similar to the ISO 3630-1 simulations, the appropriateness of the model simplifications is evaluated.

In the cyclic fatigue model involving an actual molar tooth, the ProTaper Universal F2 file is employed. The investigation focuses on the impact of both the pecking motion and the reciprocating motion from the electric motor on the dissipated energy density.

7.2.1. Gambarini Test Apparatus

7.2.1.1. Endodontic File in Fixed Position. The cyclic fatigue simulation, including the canal, shows similar deformation behavior for both endodontic files. At the end of the insertion step, the endodontic file's mid-section contacts the cylinder at point A, while the file's tip contacts the jig at point B, located where the jig's cylindrical and horizontal flat surfaces meet as illustrated in Figure 7.6.

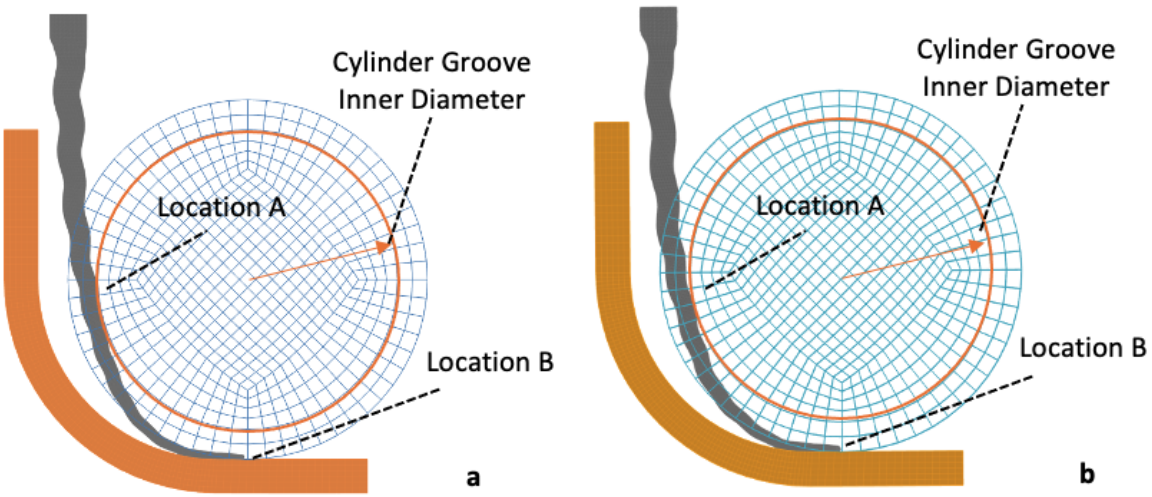

Figure 7.6. The deformed configuration of endodontic files in Gambarini's test apparatus at the end of Insertion Step (a) PTU F1, (b) PTU F2.

Maximum hysteresis energy densities are shown in Figures 7.7 and 7.8 for F1 and F2, respectively. The highest hysteresis energy density is observed at 4.1 mm from the tip of the PTU F1 endodontic file, as illustrated in Figure 7.7. For the PTU F2 file, the simulation results indicate a failure location at 3.48 mm from the tip, as shown in Figure 7.8. These findings align with the test results revealed by Fife et al. [37].

In terms of fatigue life estimation, a maximum dissipated energy density of 64.0 MJ/m^3 was computed for the F1 endodontic file shown in Figure 7.7, while for the F2, it was 68.5 MJ/m^3 depicted in Figure 7.8.

Overall, the idealized model, in which the simulated canal is created using analytical surfaces, yields identical results to the high definition model, confirming its validity.

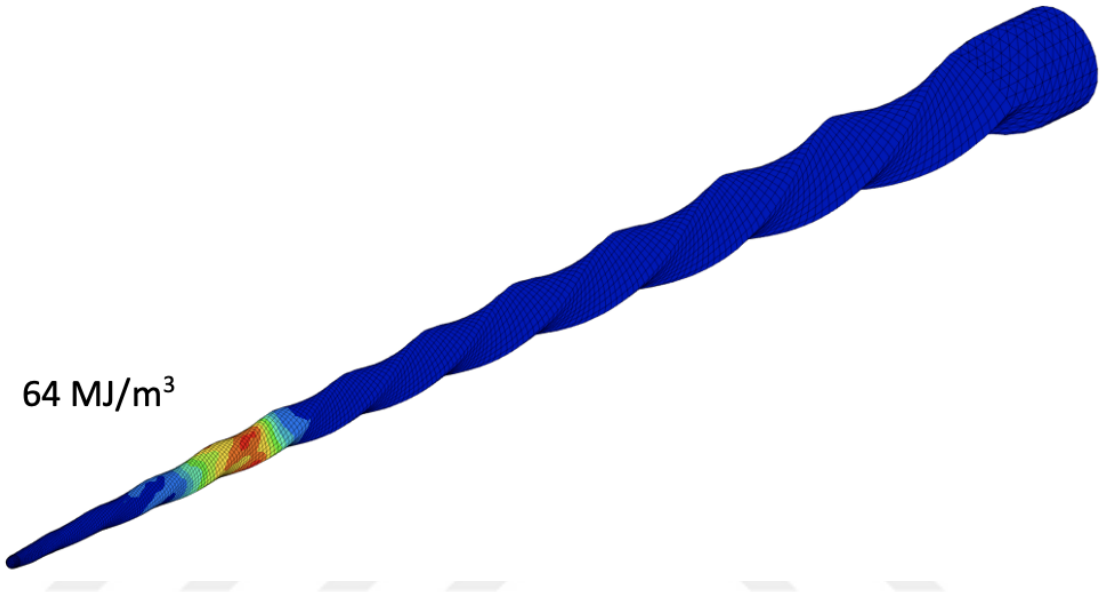

Figure 7.7. Maximum dissipated energy density in F1 file.

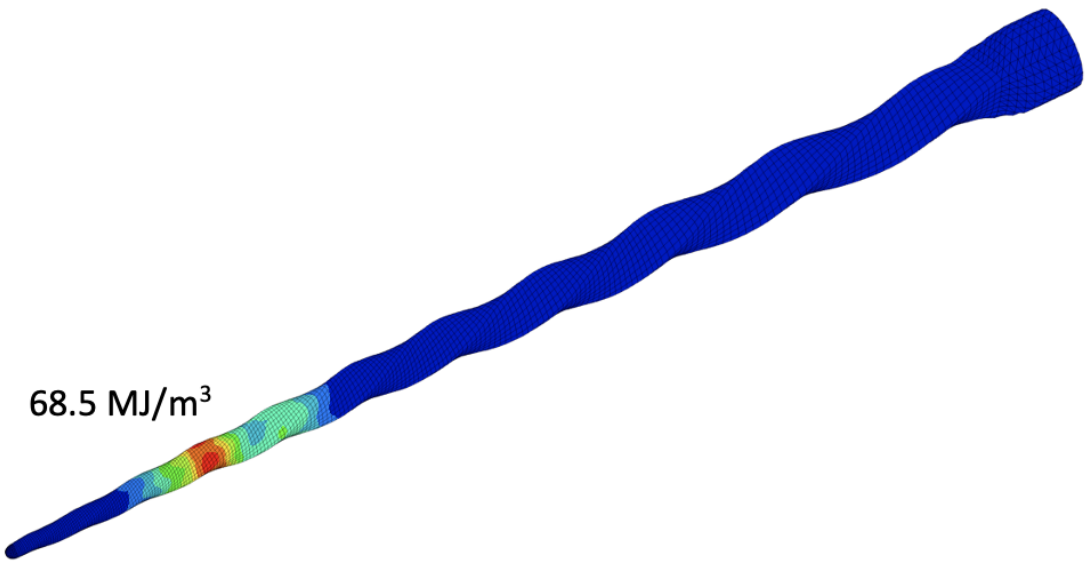

Figure 7.8. Maximum dissipated energy density in F2 file.

7.2.1.2. Effect of the Pecking Motion. The highest dissipated energy density for the configuration when the endodontic file is fixed in the axial direction, was computed as 68.5 MJ/m^3. In case a pecking motion is applied, the largest dissipated energy density is calculated as 34,9 MJ/m^3, as 50% of that calculated for the endodontic file in fixed position. The energy is distributed over a larger region of the file as compared to the case without the pecking motion as illustrated in Figure 7.9.

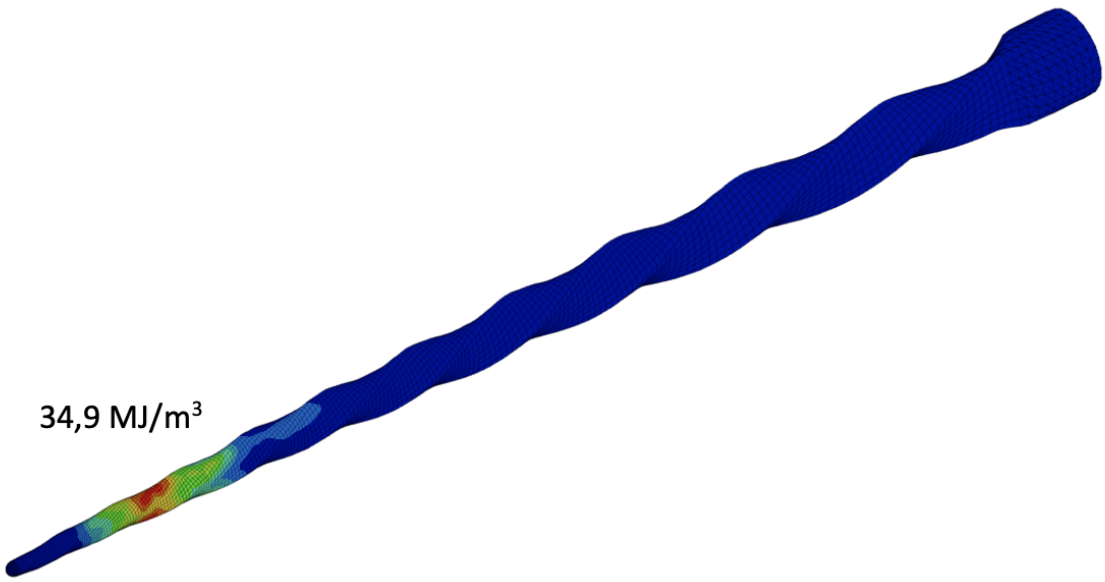

Figure 7.9. Dissipated energy density distribution over F2 endodontic file. Gambarini's test apparatus. Applied pecking motion.

7.2.1.3. Variation with Stabilized NiTi Material Parameters. The investigation reveals that hysteresis energy undergoes significant changes with stabilized material data. In the case of the stabilized material defined in Section 6.1, hysteresis energy for F2 endodontic file is calculated to be 55% lower compared to the model using material data obtained from monotonic tensile tests as seen in Figure 7.10.

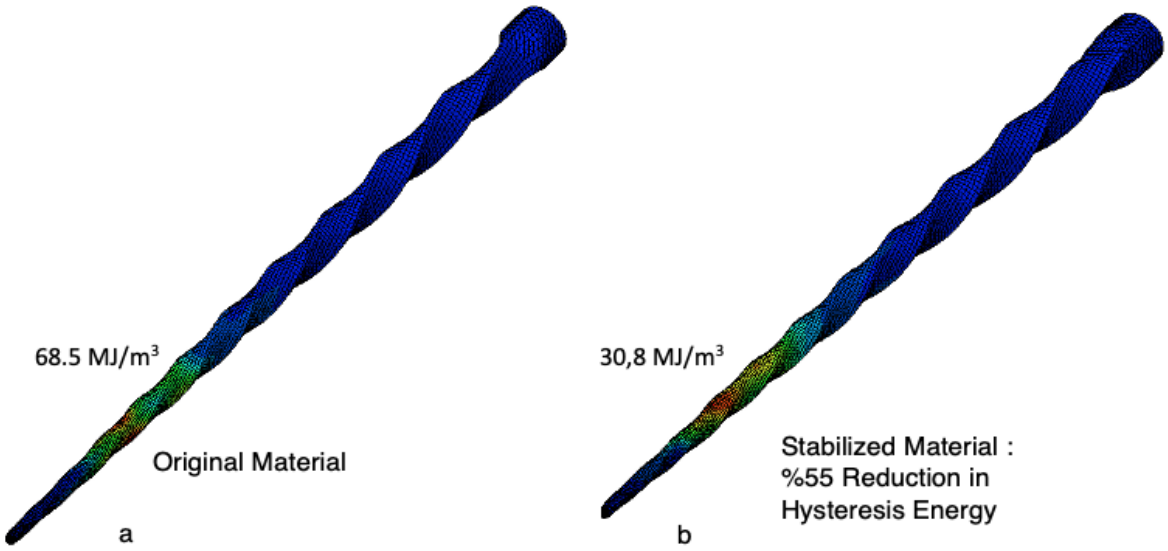

Figure 7.10. Hysteresis energy results with the original and stabilized material data comparison (a) Original (Quasi-Static) material results, (b) Stabilized (Cyclic) material results.

7.2.1.4. Gambarini Test Apparatus Results Discussion. The simulation results for the Gambarini test system indicate that during the insertion step, the mid-section of the file touches the cylinder, while the tip of the file contacts the jig's cylindrical and horizontal surfaces at their junction. This pattern is consistent with the observations made by Fife et al. [37]. In the same study, focusing on the F2 endodontic file, Fife has reported an average failure location of 3.5 mm from the file's tip. The present simulation predicts the highest dissipated energy density location of 3.48 mm from the tip, which corresponds to this test. For the F1 endodontic file, Fife reported a failure location between 4.0-5.8 mm, a range that matches the simulation's prediction of 4.1 mm from the tip.

For fatigue life estimation, Fife has recorded an average of 367 rotations for the F1 endodontic file and 320 rotations for the F2 endodontic file until failure. Simulation results indicate %8 higher dissipated energy for the F1 file compared to the F2 file in the most critical area, pointing to a longer fatigue life for endodontic file F1. The

validation further demonstrates that hysteresis energy serves as a reliable parameter for quantifying the fatigue behavior of Ni-Ti endodontic files.

Considering the effect of the pecking motion on the file durability, Fife et al. [37] reported an average of 320 rotations until failure whereas Whipple et al. [38] reported 501 rotations until failure when loading included the pecking motion. These results indicate that the pecking motion increases the fatigue life by 56%. Simulation results of this study shows a reduction of 50% of the dissipated strain energy density at the most critical location when a pecking motion is applied. This reduction could indicate fatigue life increase which is on par with these test results.

By utilizing the material parameters of stabilized NiTi under cyclic loading alters the dissipated energy density results by more than %50 compared to results with the material data from monotonic tests. Therefore, accurately estimating the number of cycles until failure, based on dissipated energy, necessitates precise calibration of the SMA material parameters to reflect the stabilized material response.

Variations in the maximum dissipated energy density, along with percentage comparisons relative to the results of the PTU F2 file operated in a fixed axial position, are presented in Table 7.4.

7.2.2. Molar Tooth Results

Cyclic fatigue simulations with the real molar tooth considers the ProTaper Universal F2 file. The effects of the pecking motion applied by the dentist as a clinical procedure, as well as the reciprocating motion actuated from the electric motor on the durability of the endodontic file are investigated. Although these aspects are investigated in detail, due to the absence of test data a quantitative validation based on test data has not been conducted. Instead, the deformation of the file and the locations of accumulated stresses on the dentin are evaluated for qualitative validation of the simulation results.

Table 7.4. Endodontic file maximum dissipated energy density results for the Gambarini test apparatus.

Simulation	**Maximum Dissipated Energy Density (MJ/m^3)**	**Difference (%)**
PTU F2 (Fixed Axial Position)	64	0
PTU F1 (Fixed Axial Position)	68.5	8 (↑)
PTU F2 (Pecking Motion)	34.9	50 (↓)
PTU F2 (Stabilized NiTi Material Parameters)	30.8	55 (↓)

7.2.2.1. Fixed Position . At the end of the insertion step, accumulated von Misses stresses are observed at the apical section of the dentin as seen in Figure 7.11. Considering that the design intent of ProTaper Universal F2 endodontic file, which is marketed for the shaping of the apical section of the root canal [73], is to increase stresses in that area, this result supports the validity of the simulation.

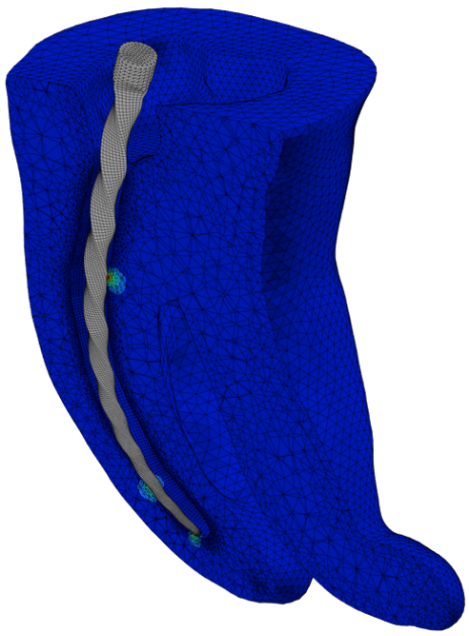

Figure 7.11. Stress distribution in the dentin tissue.

The largest dissipated energy density for the rotation step, where the endodontic file is not allowed to have an axial displacement is calculated as 38 MJ/m3 as illustrated in Figure 7.12

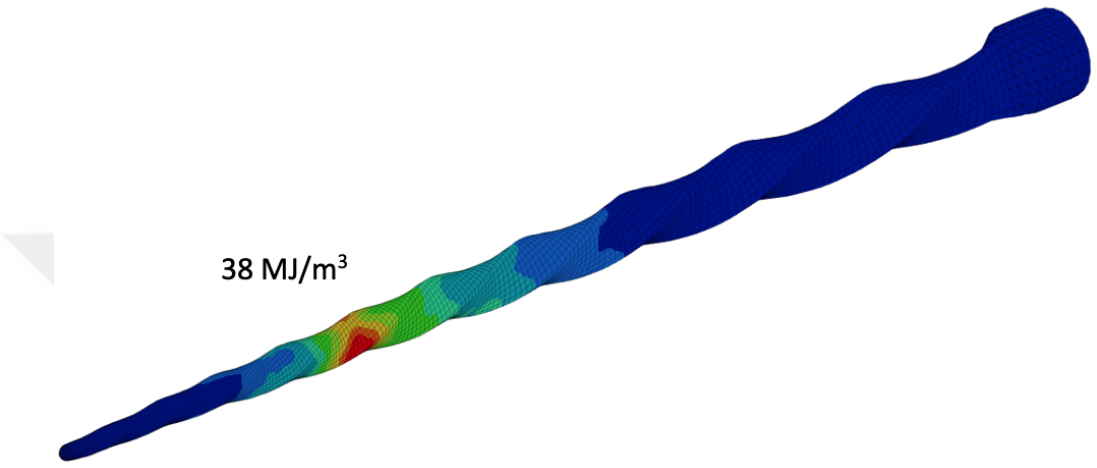

Figure 7.12. Dissipated energy density distribution in F2 endodontic file, for molar tooth canal and without pecking motion.

7.2.2.2. Pecking Motion. If a pecking motion is applied, the maximum dissipated energy density is 16 MJ/m3 which indicates around a %58 reduction compared to the case where the file is held at a stationary position. The energy is distributed on the working region more evenly as compared to the loading without pecking motion when there is localization in one area as shown in Figure 7.13.

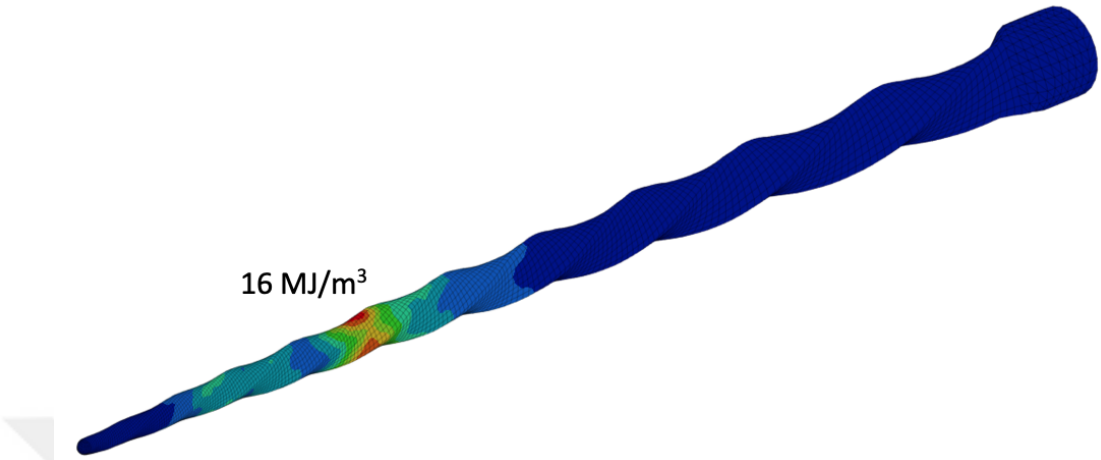

Figure 7.13. Dissipated energy density distribution in F2 endodontic file, for molar tooth canal and with pecking motion.

7.2.2.3. Reciprocating Motion. The cumulative dissipated energy density from a total of 1800 degrees of cutting motion is compared between reciprocating and continuous rotation modes. The hysteresis energy is found to be 9.1% lower in the reciprocating mode compared to that in the continuous rotation mode, aligning with statements in the literature [33], as seen in Figure 7.14.

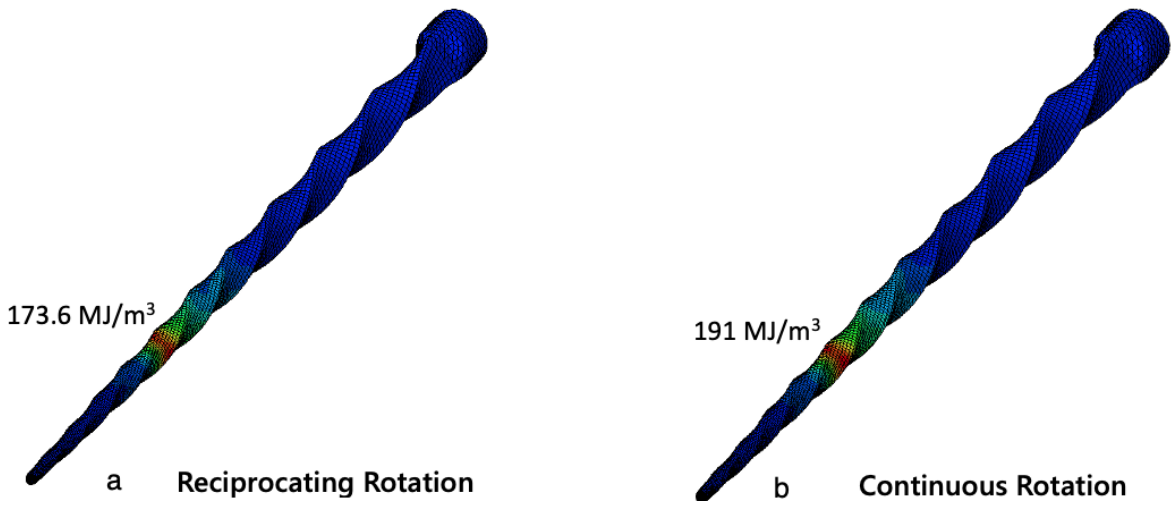

Figure 7.14. Dissipated energy results over 1800 degrees of cutting motion. (a) Results with reciprocating motion, (b) Results with continous rotation.

7.2.2.4. Molar Tooth Results Discussion. The simulations of endodontic procedure applied to a molar tooth result in much lower dissipated energy levels, about %44.5, as compared to those for the simulations of the Gambarini's test configuration. This might mean that, when the endodontic file rotates freely, without any misuse by the dentist or without being stuck in the dentin tissue, both of which are identified by Fife et al. [37] as critical scenarios affecting the prolonged reuse of the instrument, even for a very curved root canal geometry, a higher number of rotations until failure is expected compared to that measured in the Gambarini test configuration. The simulation also indicates that the pecking motion decreases the dissipated energy density, by %58, which leads to expectation that pecking motion increases the fatigue life of the endodontic file utilized in a real tooth' root canal geometry even more than that for a simulated root canal with 90 degrees of curvature. Regarding the reciprocating motion results, around %9.1 percent of reduction is observed in the dissipated energy results, indicating an improved fatigue life compared to the case where a continuous rotation mode is utilized. Variations in the maximum dissipated energy density, along with percentage comparisons relative to the results of the PTU F2 file operated in a fixed axial position, are presented in Table 7.5.The stress concentration at the apical section of the dentin for ProTaper Universal F2 file indicates the simulation correctly represents the endodontic procedure.

Table 7.5. Endodontic file maximum dissipated energy density results for the molar tooth.

Simulation	**Maximum Dissipated Energy Density (MJ/m^3)**	**Difference (%)**
PTU F2 (Fixed Axial Position)	38	0
PTU F2 (Pecking Motion)	16	58 (↓)
PTU F2 (Reciprocating Motion)	34	9.1 (↓)

7.3. Cutting Resistance Investigation

Effect of the cutting resistance, hence the twisting torque on the hysteresis energy was investigated. Cutting resistance was introduced in the simulation through the tangential contact behaviour as Coulomb friction. Root canal treatment procedure was performed on the real molar tooth according to:

- Initially, the insertion step was performed without any friction implementation.
- With the rotation steps, friction was introduced.
- Friction coefficient was altered for each rotation step.
- The motor torque was also recorded during the procedure.

It was observed that the cutting resistance may have significant effect on the file durability as shown in Figure 7.15. Due to complexity of material removal physics, there is still room for further research on the topic for modeling improvements and methodology validation.

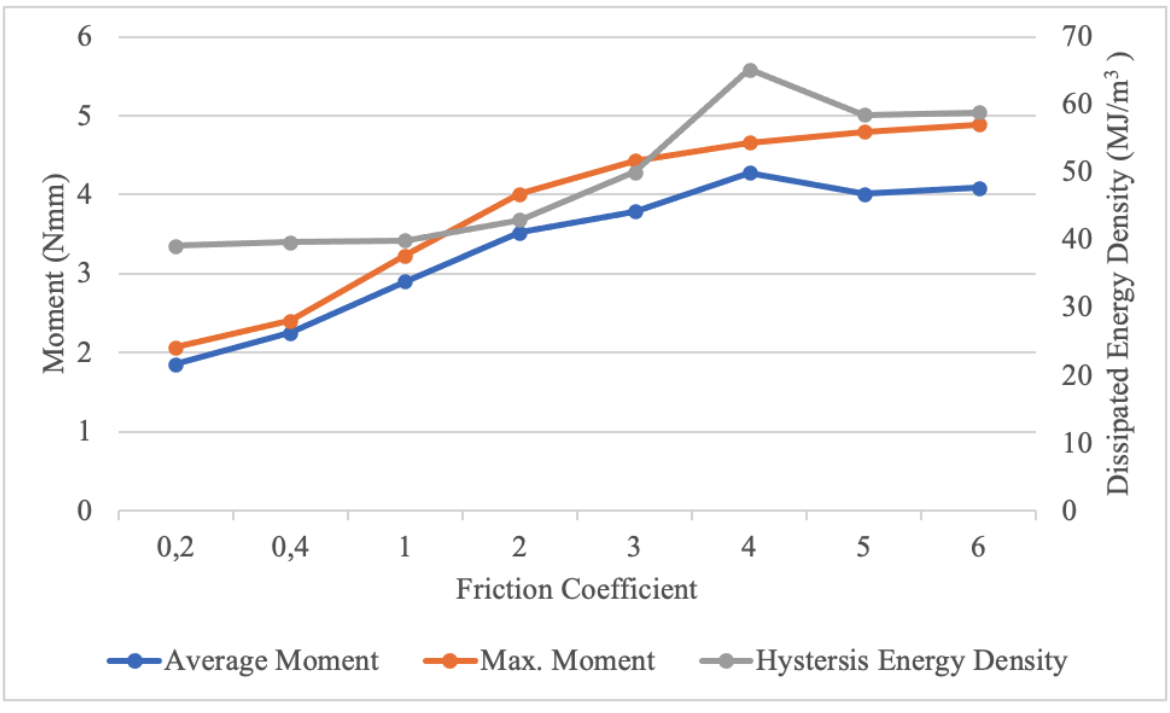

Figure 7.15. Dissipated energy and motor torque vs friction coefficient.

7.4. Sensitivity to Molar Tooth Material Parameters

Based on the tooth material model parameters matrix provided in Table 6.3, file insertion, cyclic fatigue with stationary file position and cyclic fatigue with the pecking motion simulations are performed with the real molar tooth model by utilizing the F2 file. For an easier understanding and interpretation, stress results for different parameter sets are normalized with respect to the results for the stiff model.

7.4.1. Endodontic File Results

The findings from the stiff model showed a maximum von Mises stress of 529.9 MPa, maximum principal stress of 530.5 MPa, and minimum principal stress of -620.2 MPa on the file structure after the endodontic file is fully inserted into the root canal. Additionally, variations in all Young's moduli of tooth tissues showed a minimal effect on the file fatigue life, altering by less than 5% as shown in Figure 7.16. Notably, employing an oscillating motion during the procedure was observed to enhance the file's fatigue life in actual tooth canals, a result attributed to the dissipated strain energy approach, as detailed in Figure 7.17.

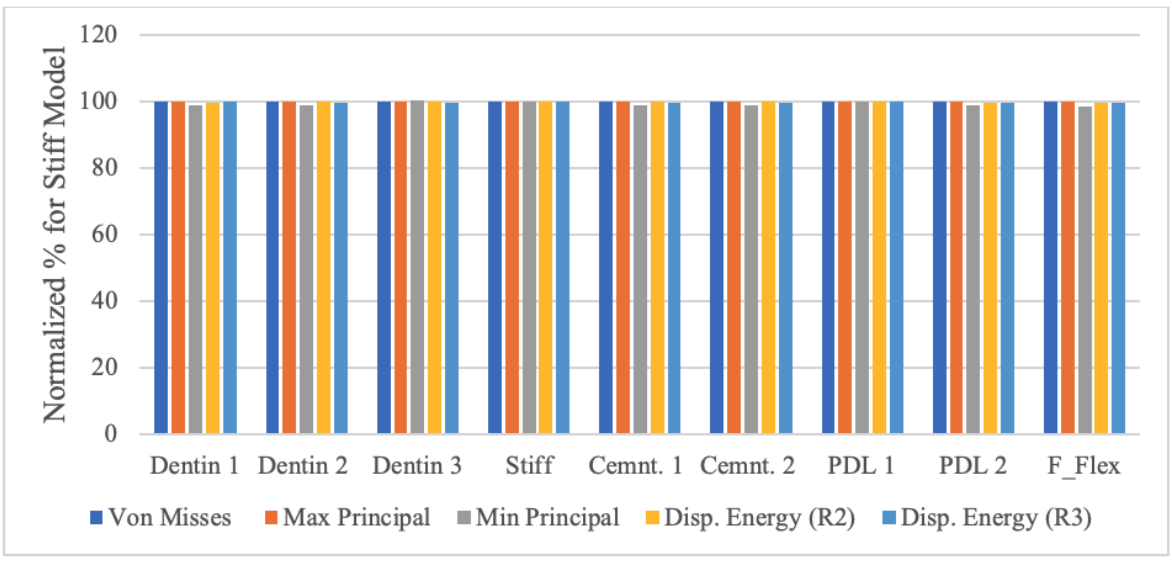

Figure 7.16. File results.

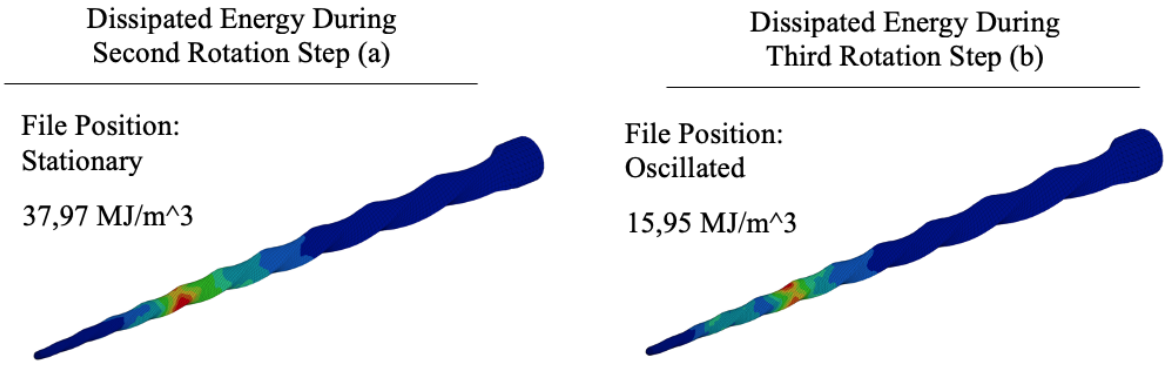

Figure 7.17. Dissipated energy during second rotation step (a) Dissipated energy during third rotation step (b).

7.4.2. Dentin Results

The results derived from the stiff model, specifically at the end of the insertion step, reveal a maximum von Mises stress of 81.34 MPa as shown in Figure 7.18, with the maximum principal stress recorded at 15.84 MPa and the minimum principal stress at -112.5 MPa. The analysis further highlights that variations in all of the tissues Young's Modulus exert a negligible impact on the dentin's maximum stress results, with changes amounting to less than 5% as illustrated in Figure 7.19. This suggests a relatively stable response in stress outcomes despite fluctuations in the mechanical properties of the surrounding tissue.

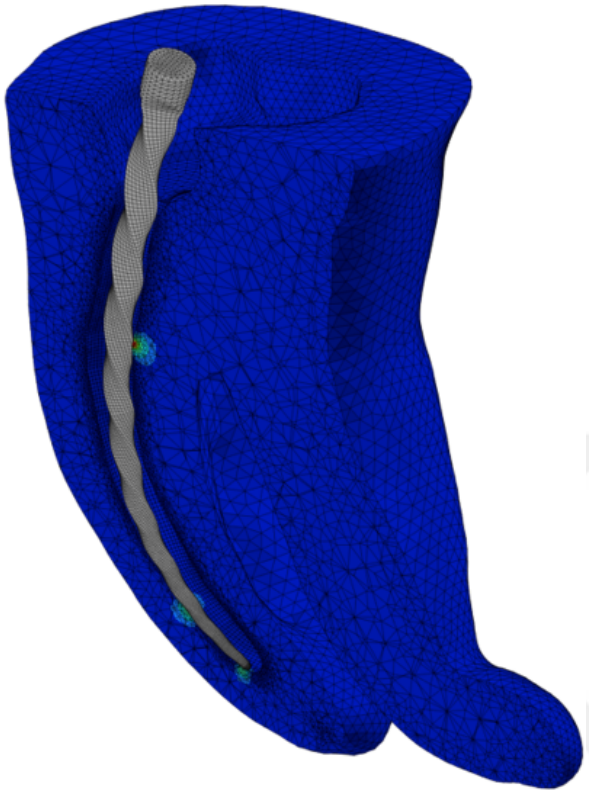

Figure 7.18. Dentin von Mises stress distribution at the end of insertion step.

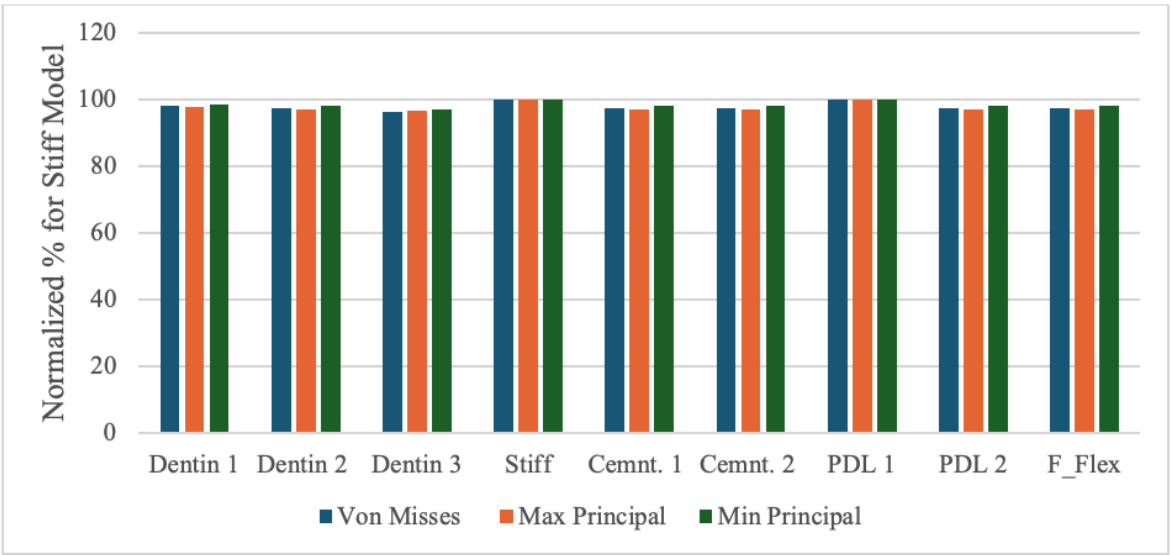

Figure 7.19. Stress data on dentin.

7.4.3. Cementum Results

The analysis of the stiff model, particularly following the insertion step, recorded markedly low stress levels, with von Mises stress at 0.251 MPa, maximum principal stress at 0.271 MPa, and minimum principal stress at -0.198 MPa as illustrated in Figure 7.21. These values are significantly lower then those observed in dentin tissue, which has a maximum von Mises stress of 81.34 MPa. Furthermore, variations in all the tissues Young's Modulus are found to have a considerable effect on the maximum stress results for cementum as depicted in Figure 7.20, contrasting with the negligible impact observed in other tissues. A comparative study between the stiff model and the full linear elastic model reveals that cementum stresses experience about 200% increase, underscoring the significant sensitivity of cementum to mechanical properties changes.

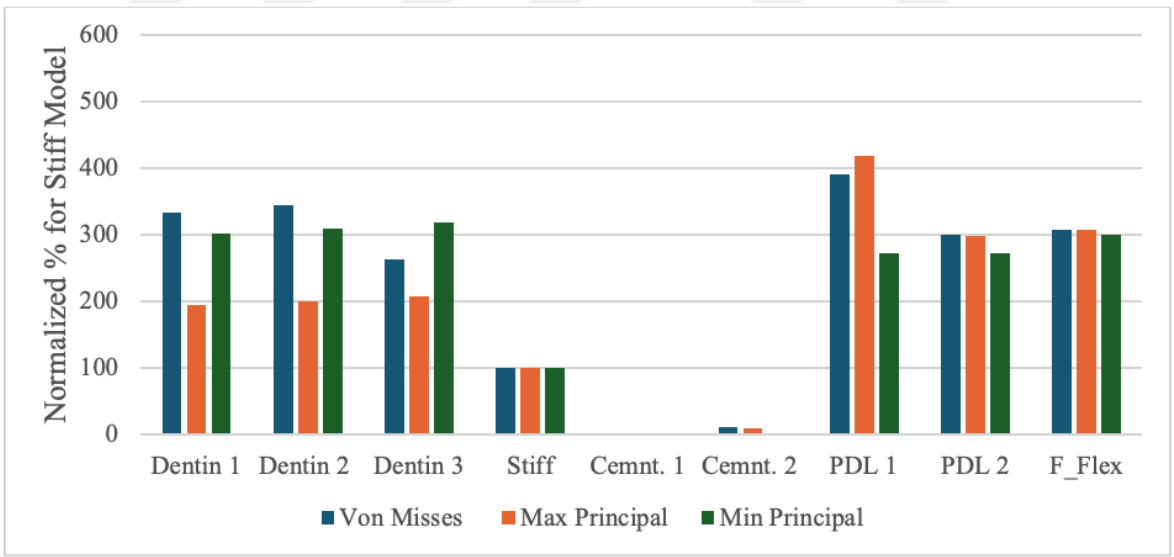

Figure 7.20. Stress data on cementum.

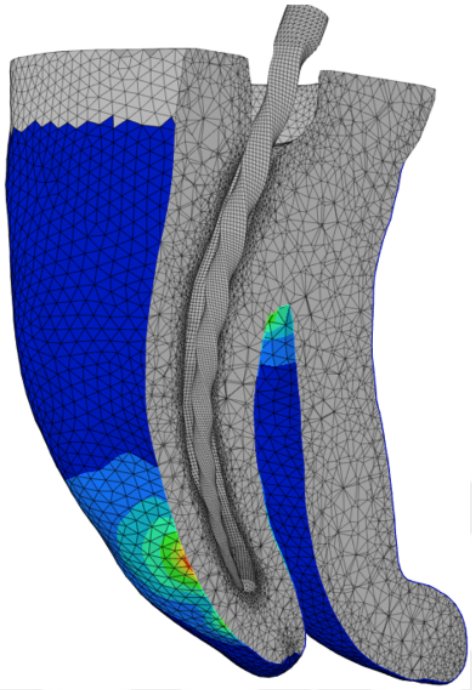

Figure 7.21. Cementum von Mises stress distribution at the end of insertion step.

7.4.4. PDL Results

The stiff model results at the end of the insertion step showed a maximum von Mises stress of 0.329 MPa, with the maximum principal stress reaching 0.697 MPa and the minimum principal stress at -1.172 MPa as depicted in Figure 7.22. These stress levels are significantly lower compared to those found in dentin tissue, which exhibits a maximum von Mises stress of 81.34 MPa. Furthermore, the investigation reveals that variations in all the tissues Young's Modulus have a profound impact on the maximum stress outcomes for the Periodontal Ligament (PDL), indicating a sensitivity to mechanical property changes as shown in Figure 7.23. A comparison between the stiff model and the full linear elastic model indicates a dramatic decrease in PDL stresses by approximately 95%. According to a literature review, such observed stress and strain levels in the full elastic model are within the range that would typically elicit a linear response, suggesting predictable behavior under the conditions tested.

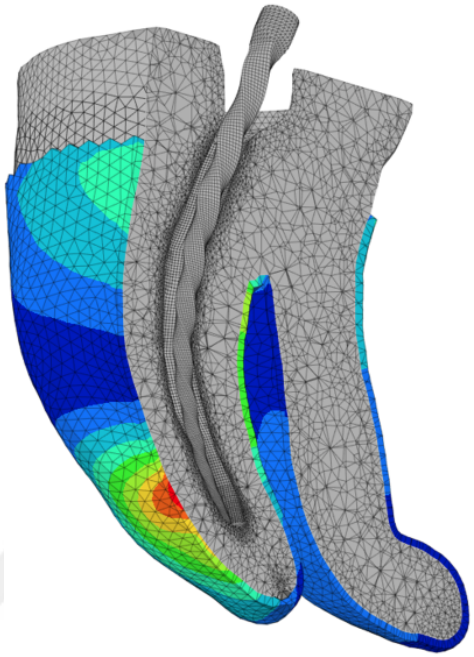

Figure 7.22. PDL von Mises stress distribution at the end of insertion step.

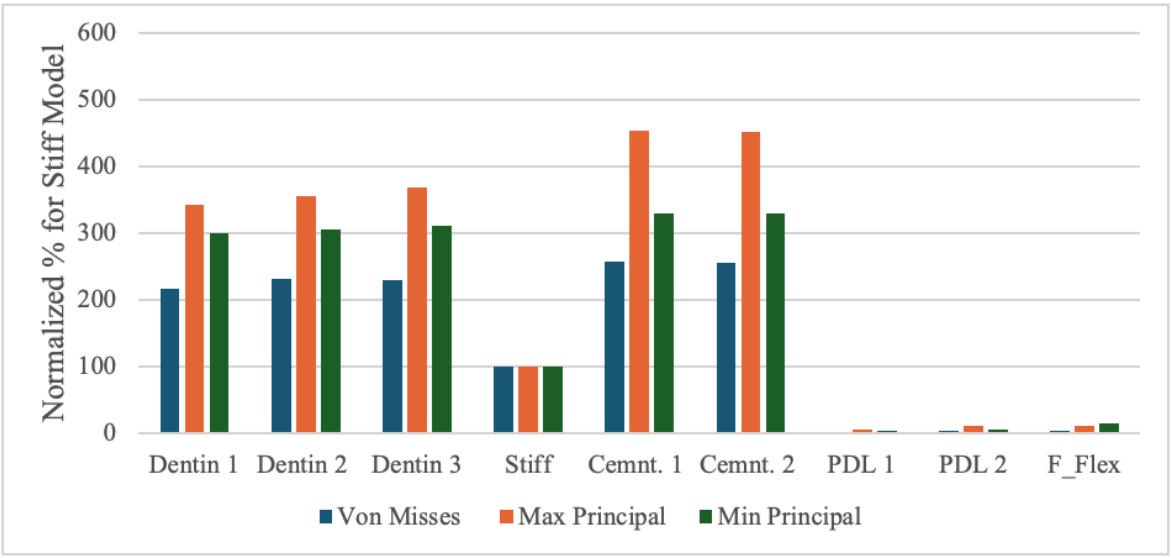

Figure 7.23. Stress data on PDL.

7.4.5. Bone Results

At the end of the insertion step, the stiff model results revealed von Mises stress at 0.308 MPa, maximum principal stress at 0.111 MPa, and minimum principal stress at -0.241 MPa as shown in Figure 7.24. These stress measurements are substantially lower than those observed in dentin tissue, which has a reported maximum von Mises stress of 81.34 MPa. The data indicates that variations in the tissue Young's Modulus significantly influence the maximum stress results for bone tissue according to Figure 7.25. When contrasting the stiff model with the full linear elastic model, a noteworthy decrease of about 60% in the stresses of the Periodontal Ligament (PDL) was observed, highlighting the impact of differing mechanical models on the stress outcomes within dental tissues.

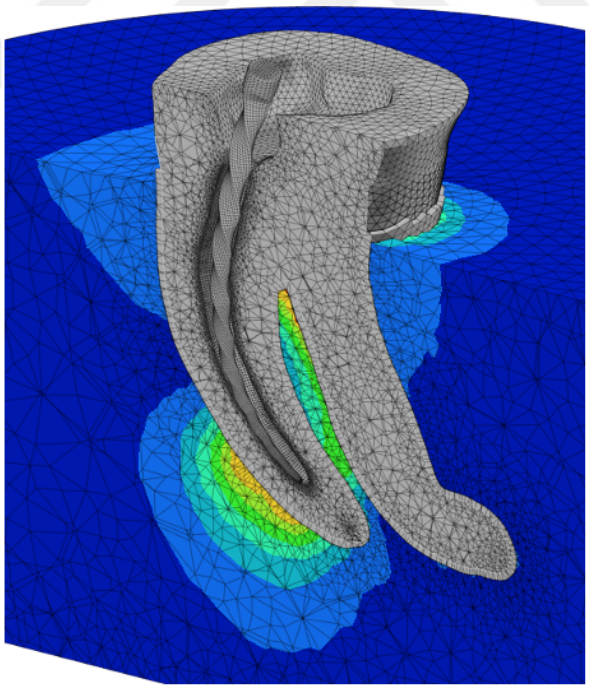

Figure 7.24. Bone von Mises stress distribution at the end of insertion step.

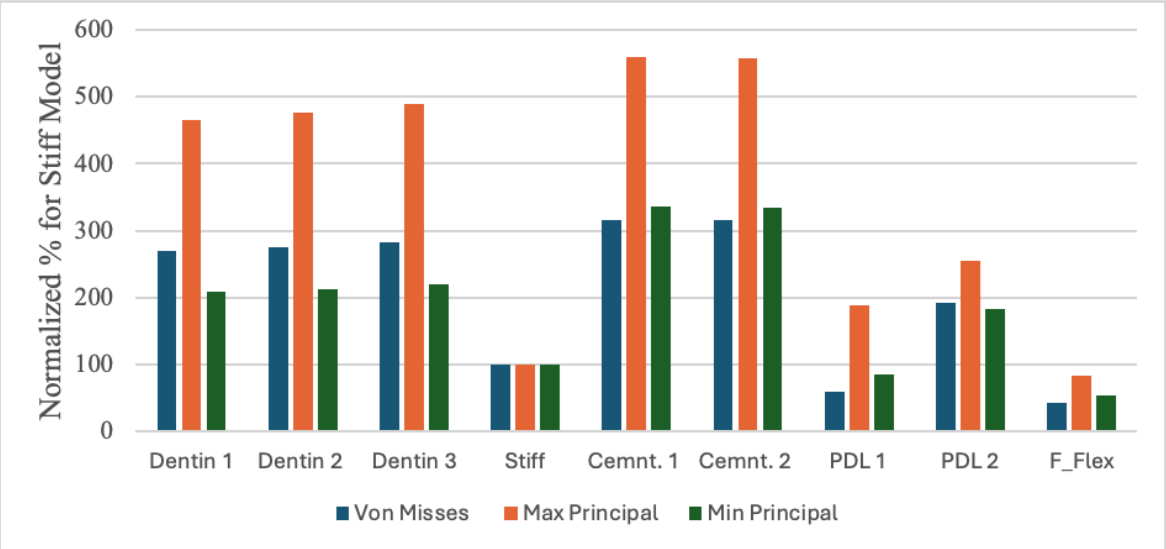

Figure 7.25. Stress data on bone.

7.5. Endodontic File Deformational Behavior Study

Utilizing the real molar tooth model, contact stresses on dentin tissue was investigated for different endodontic files of ProTaper Universal file set. It is observed, as expected, finishing files (F1, F2) work on the area closer to apical section of the root canal whereas shaping files (S1, S2) work on areas closer to the coronal section ares as illustrated in Figure 7.26. Deformational behaviourof endodontic files after the insertion aligns with the contact stress pattern on the dentin tissue depicted in Figure 7.27.

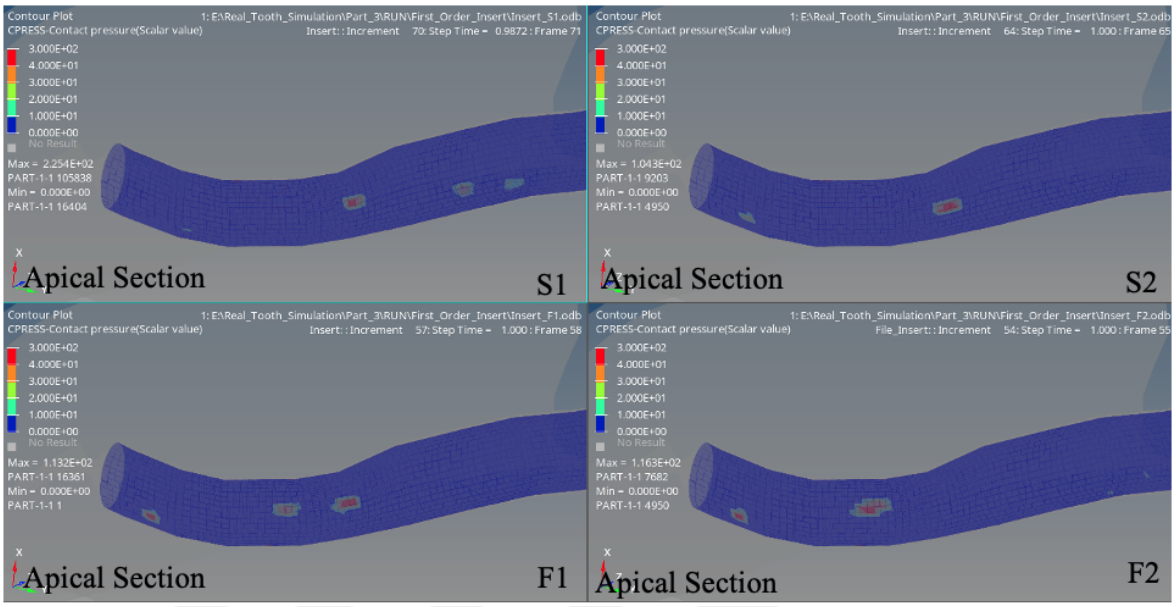

Figure 7.26. Contact stress distribution on dentin for S1, S2, F1, F2 endodontic files.

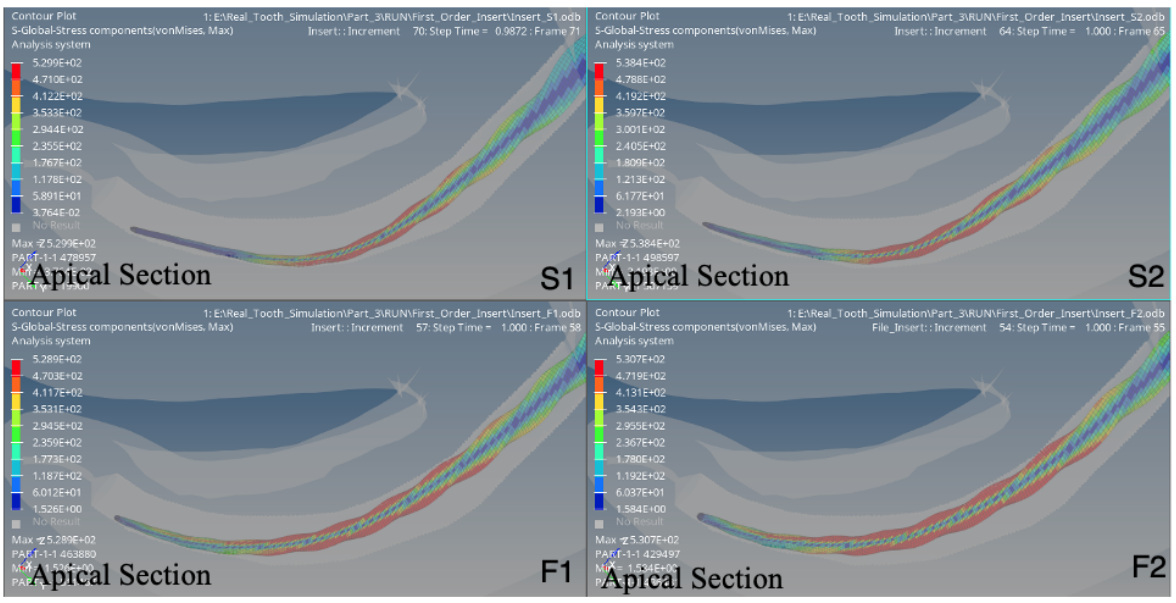

Figure 7.27. Deformational behaviour of S1, S2, F1, F2 endodontic files.

8. CONCLUSION

In this thesis, a Finite Element Analysis (FEA) methodology was developed within the Abaqus environment using the built-in shape memory alloy constitutive model. This methodology is designed for the structural assessment of rotary endodontic files manufactured from conventional austenitic Ni-Ti alloys. The primary objective was to understand and accurately capture the mechanical behavior and failure modes of these instruments under various operational conditions. Specifically, the study focused on the torsional and bending characteristics of endodontic files, as well as their fatigue behavior during different root canal procedures.

The methodology development involved performing bending and torsional test simulations as defined in the ISO 3630-1 standard [14] for assessing the torsional and bending behaviour of endodontic files. For the cyclic fatigue behavior assessment, the simulated root canal test configuration proposed by Gambarini was utilized. Additionally, the root canal treatment procedure was simulated for a molar tooth with significant root canal curvature to understand the influence of root canal curvature on the fatigue behavior of endodontic files.

The study began by exploring the fundamental design parameters and material properties of Ni-Ti endodontic files. Various root canal operation techniques were detailed. Given that the development was performed in the Abaqus environment, the built-in Shape Memory Alloy module was thoroughly investigated, and the implementation, based on the formulation by Auricchio, was explained in detail. Regarding the physical test systems, the configuration details and boundary conditions were presented. Furthermore, for modeling the molar tooth, a literature review was conducted to determine the tissue material properties, and a simulation matrix was constructed for sensitivity analysis to the tissue properties.

Specifically, the ProTaper Universal file set was chosen for the methodology development due to its widespread use in root canal treatments and the availability of available data in the literature. The geometry of the files and the molar tooth was acquired through 3D scanning. The geometry data for the physical tests, including the torsion and bending tests defined in ISO 3630-1, as well as the cyclic fatigue test proposed by Gambarini, were taken from the literature. The loading and fixation conditions for the ISO 3630-1 tests were taken from the standards, and the operational conditions for the cyclic fatigue test performed on the simulated canal were acquired as defined by Gambarini. Regarding the molar tooth FEA model, similar fixation and loading conditions were applied as in the simulated root canal. The cyclic fatigue behavior of the endodontic instruments under various operational techniques, specifically with the pecking motion and with the reciprocating motion, was investigated by utilizing the simulated canal and the molar tooth FEA models. For all the developed models, comprehensive and simplified versions were created, and the results were validated with the literature for model and methodology verification.

One of the contributions of this work was the application of the dissipated energy method for the fatigue life estimation of endodontic files manufactured from conventional Ni-Ti alloys. The hysteresis energy approach for assessing fatigue behavior appears to be suitable for dynamic cyclic fatigue tests, where pecking motion or reciprocating motion was applied. This stood in contrast to static tests, where the endodontic file was rotated at a constant speed and held at the same axial position. In terms of file durability, the hysteresis energy was used to compare different loading scenarios and to understand the fatigue behavior of the ProTaper Universal endodontic file set. It is important to note that different endodontic file sets are generally manufactured from various Ni-Ti alloys and undergo different heat treatments. Consequently, calibrating the relationship between dissipated energy and fatigue life is necessary to accurately calculate the number of cycles until failure. Such calibration was not within the scope of this study. Additionally, the energy dissipation approach relies on the fatigue mechanism from the phase transformation in Ni-Ti alloys. Thus, this approach is applicable to a wide range of austenitic endodontic files that exhibit super-elastic behavior during

the root canal treatment procedure.

The simulation results for the ISO 3630-1 test systems and the cyclic fatigue simulations showed a reasonable correlation with the physical test data from the literature. Regarding the ISO 3630-1 torsion and bending simulations, the structural stiffness calculations were consistent with the results from the literature. For the cyclic fatigue simulations, the file deformational behavior and the failure locations of the endodontic files matched the physical test data from the literature. Additionally, the application of pecking motion and reciprocating motion increased the fatigue life of endodontic files, as indicated in the reviewed literature. In the sensitivity analysis for the material parameters used in the molar tooth FEA model, it was observed that, while material data variation had minimal impact on the file results, it significantly affected the results for the tissues themselves. This underscores the importance of accurate material respresentation when the focus is on tissue results. Furthermore, during the root canal procedure, the principal stresses in the tooth tissue remained within the elastic range, indicating that the linear elastic material implementation was appropriate for the root canal simulations. Lastly, it was observed that the proposed simplifications for the simulation model were appropriate.

The future research topics could not only address certain limitations of the proposed methodology but also provide improvements in the field.

One limitation of the methodology presented in this thesis arises from the built-in Shape Memory Alloy constitutive model of the Abaqus software. While this constitutive model worked well for this study, primarily due to its capacity to capture the inner loop effect, it employs a symmetric approach that treats tension and compression equally. Adopting an asymmetric implementation would likely yield a more realistic simulation. However, such an implementation would require the development of a UMAT (User Material) subroutine and the availability of comprehensive material data for calibration. Additionally, the model cannot account for temperature variations, which were originally incorporated by Auricchio in his formulation. Incorporating the

temperature influence into the Abaqus constitutive model could be an important contribution and improvement which would also enhance the current methodology to capture the shape memory behaviour of endodontic files manufactured from conventional NiTi alloys.

Another possible research topic relates to the calibration of the number of cycles and hysteresis energy for various file sets manufactured from austenitic Ni-Ti alloys. In this thesis, hysteresis energy is utilized for comparing different loading scenarios and understanding general fatigue behavior. However, calibration is essential for directly computing fatigue life based on dissipated energy. This work would require a significant amount of test data for various file sets and loading conditions.

A further limitation of the current methodology is related to cutting resistance during the dentin removal process. Presently, a simplified approach is implemented by applying friction at the contact between the dentin and the file, and calibrating the friction coefficient to match test data. However, incorporating material removal mechanism into the model could significantly increase accuracy, making this an important research topic.

Although not a modeling limitation, a study on the geometry optimization of a file set by considering fatigue life, structural stiffness, and cutting efficiency would be an interesting application of the proposed methodology.

Finally, other than the basic approach where the endodontic file is held at the same axial position and rotated with constant speed, the current methodology was utilized for pecking motion operation technique and also utilized for reciprocating motion. However, there are a significantly wider range of techniques and application procedures for endodontic files. Consequently, applying the methodology to other techniques, as well as variations of the currently investigated techniques, such as reciprocating motion with different rotation configurations or pecking motion with different brushing amplitudes, would demonstrate the potential of the developed methodology and provide a

better understanding of file response for various use cases.

REFERENCES

1. WebMD, "The Teeth," https://www.webmd.com/oral-health/teeth-and-gum-care, accessed on June 15, 2021.

2. A. Flores and A. Pastenes, "Evolution of instruments in endodontics - literature review," *International Journal of Dentistry and Oral Health*, vol. 5, no. 6, pp. 1–5, 2019.

3. J. Zupanc, N. Vahdat-Pajouh, and E. Schäfer, "New Thermomechanically Treated NiTi Alloys-A Review," *International Endodontic Journal*, vol. 51, no. 10, pp. 1088–1103, 2018.

4. G. C. Sevencan, S. Tazegül-Kocak, B. C. Sağlam, and M. M. Koçak, "Evaluation of Nickel Titanium Instruments on Apical Debris Extrusion in Curved Canals," *Uluslararası Diş Hekimliği Bilimleri Dergisi*, vol. 7, no. 3, pp. 46–50, 2021.

5. "Government Advises Single Use of Endodontic Instruments," *British Dental Journal*, vol. 202, no. 8, pp. 442–442, 2007.

6. M. Sharma, B. Paul, M. Shivkumar, K. Dube, C. Kapur, P. Sinha, and S. Mehta, "Recent Advances in Endodontic Instruments - A Literature Review," *Journal of Population Therapeutics and Clinical Pharmacology*, vol. 31, no. 1, pp. 1080–1087, 2024.

7. A. M. Media, "Root Canal Treatment," https://www.alilamedicalmedia.com/, accessed on May 13, 2024.

8. L. d. A. Santos, P. D. Resende, M. G. d. A. Bahia, and V. T. L. Buono, "Effects of R-Phase on Mechanical Responses of a Nickel-Titanium Endodontic Instrument: Structural Characterization and Finite Element Analysis," *The Scientific World Journal*, vol. 2016, no. 1, p. 7617493, 2016.

9. D. Sirona, “ProTaper Universal File Set,” https://www.dentsplysirona.com/, accessed on June 15, 2021.

10. D. Rokaya, V. Srimaneepong, S. Hiran-us, and Z. Khurshid, “6 - Alloys for Endodontic Files and Hand Instruments,” in *Biomaterials in Endodontics*, ser. Woodhead Publishing Series in Biomaterials, Z. Khurshid, M. S. Zafar, and S. Najeeb, Eds. Woodhead Publishing, 2022, pp. 131–168.

11. D. S. Instruments, “ProTaper Next File Set,” https://dentalstall.com, accessed on June 15, 2021.

12. H. E. Özdiler, “Kök Kanal Şekillendirmesi Esnasında Oluşan Streslerin Sonlu Elemanlar Analizi Yöntemi ile Değerlendirilmesi,” Ph.D. dissertation, İstanbul Üniversitesi, 2016.

13. A.-S. Boscornea-Pușcu, L. Orel, O.-A. Velea-Barta, R. M. Horhat, M.-L. Negruțiu, L. M. Nica, V.-F. Duma, D. I. Stoia, C. Opriș, and C. Sinescu, “Experimental Study of the Effects of Torsional Loading on Three Types of Nickel-Titanium Endodontic Instruments,” *Applied Sciences*, vol. 11, no. 16, p. 7224, 2021.

14. D. C. Instruments—Part, “1: General Requirements and Test Methods,” *Geneva, Switzerland: International Organization for Standardization*, pp. 3630–1, 2008.

15. F. Lo Savio, G. La Rosa, M. Bonfanti, D. Alizzio, E. Rapisarda, and E. Pedullà, “Novel Cyclic Fatigue Testing Machine for Endodontic Files,” *Experimental Techniques*, vol. 44, pp. 649–665, 2020.

16. L. de Arruda Santos, J. B. López, E. B. de Las Casas, M. G. de Azevedo Bahia, and V. T. L. Buono, “Mechanical Behavior of Three Nickel-Titanium Rotary Files: A Comparison of Numerical Simulation with Bending and Torsion Tests,” *Materials Science and Engineering: C*, vol. 37, pp. 258–263, 2014.

17. A. S. Câmara, R. de Castro Martins, A. C. D. Viana, R. de Toledo Leonardo,

V. T. L. Buono, and M. G. de Azevedo Bahia, "Flexibility and Torsional Strength of ProTaper and ProTaper Universal Rotary Instruments Assessed by Mechanical Tests," *Journal of Endodontics*, vol. 35, no. 1, pp. 113–116, 2009.

18. M. I. El-Anwar, S. A. Yousief, E. M. Kataia, and T. M. A. El-Wahab, "Finite Element Study on Continuous Rotating versus Reciprocating Nickel-Titanium Instruments," *Brazilian Dental Journal*, vol. 27, pp. 436–441, 2016.

19. M. Prados-Privado, R. Rojo, C. Ivorra, and J. C. Prados-Frutos, "Finite Element Analysis Comparing WaveOne, WaveOne Gold, Reciproc and Reciproc Blue Responses with Bending and Torsion Tests," *Journal of the Mechanical Behavior of Biomedical Materials*, vol. 90, pp. 165–172, 2019.

20. S. C. S. Martins, P. R. Garcia, A. C. D. Viana, V. T. L. Buono, and L. A. Santos, "Off-Centered Geometry and Influence on NiTi Endodontic File Performance Evaluated by Finite Element Analysis," *Journal of Materials Engineering and Performance*, vol. 29, pp. 2095–2102, 2020.

21. N. Bonessio, E. Pereira, G. Lomiento, A. Arias, M. Bahia, V. T. L. Buono, and O. A. Peters, "Validated Finite Element Analyses of WaveOne Endodontic Instruments: A Comparison Between M-Wire and NiTi Alloys," *International Endodontic Journal*, vol. 48, no. 5, pp. 441–450, 2015.

22. V. Chevalier, R. Arbab-Chirani, S. Arbab-Chirani, and S. Calloch, "An Improved Model of 3-Dimensional finite Element Analysis of Mechanical Behavior of Endodontic Instruments," *Oral Surgery, Oral Medicine, Oral Pathology, Oral Radiology, and Endodontology*, vol. 109, no. 3, pp. e111–e121, 2010.

23. R. Arbab-Chirani, V. Chevalier, S. Arbab-Chirani, and S. Calloch, "Comparative Analysis of Torsional and Bending Behavior Through Finite-Element Models of 5 Ni-Ti Endodontic Instruments," *Oral Surgery, Oral Medicine, Oral Pathology, Oral Radiology, and Endodontology*, vol. 111, no. 1, pp. 115–121, 2011.

24. M.-H. Lee, A. Versluis, B.-M. Kim, C.-J. Lee, B. Hur, and H.-C. Kim, "Correlation Between Experimental Cyclic Fatigue Resistance and Numerical Stress Analysis for Nickel-Titanium Rotary Files," *Journal of endodontics*, vol. 37, no. 8, pp. 1152–1157, 2011.

25. H. Kim, H. Kim, C. Lee, B. Kim, J. Park, and A. Versluis, "Mechanical Response of Nickel-Titanium Instruments with Different Cross-Sectional Designs During Shaping of Simulated Curved Canals," *International Endodontic Journal*, vol. 42, no. 7, pp. 593–602, 2009.

26. A. Scattina, M. Alovisi, D. S. Paolino, D. Pasqualini, N. Scotti, G. Chiandussi, and E. Berutti, "Prediction of Cyclic Fatigue Life of Nickel-Titanium Rotary Files by Virtual Modeling and Finite Elements Analysis," *Journal of Endodontics*, vol. 41, no. 11, pp. 1867–1870, 2015.

27. L. H. Berman and K. M. Hargreaves, *Cohen's Pathways of the Pulp: Cohen's Pathways of the Pulp-E-Book*, Eleventh Edition, Elsevier Health Sciences, Missouri, 2020.

28. S. Morakul, S. Hiran-us, and P. Singhatanadgid, "Finite Element Analysis of the Mechanical Behaviors of Endodontic Nickel–Titanium Rotary Files: A Review," *Engineering Journal*, vol. 27, no. 8, pp. 29–49, 2023.

29. S. Agarwal, R. Nagpal, and U. Singh, "NiTi Endodontics: Contemporary Views Reviewed," *Austin Journal of Dentistry*, vol. 5, no. 4, p. 1112, 2018.

30. G. Gambarini, R. Gerosa, M. De Luca, M. Garala, and L. Testarelli, "Mechanical Properties of a New and Improved Nickel-Titanium Alloy for Endodontic Use: An Evaluation of File Flexibility," *Oral Surgery, Oral Medicine, Oral Pathology, Oral Radiology, and Endodontology*, vol. 105, no. 6, pp. 798–800, 2008.

31. A. Cladera, B. Weber, C. Leinenbach, C. Czaderski, M. Shahverdi, and M. Mo-

tavalli, “Iron-Based Shape Memory Alloys for Civil Engineering Structures: An Overview,” *Construction and Building Materials*, vol. 63, pp. 281–293, 2014.

32. W. Zaki and Z. Moumni, “A Three-Dimensional Model of the Thermomechanical Behavior of Shape Memory Alloys,” *Journal of the Mechanics and Physics of Solids*, vol. 55, no. 11, pp. 2455–2490, 2007.

33. A. C. Topuz, “Farklı Resiprokal Döner Alet Sistemlerinin Çalışması Sırasında Ortaya Çıkan Kuvvetlerin Sonlu Elemanlar Analizi Yöntemi ile Değerlendirilmesi,” Ph.D. dissertation, İstanbul Üniversitesi, 2019.

34. J. Ha, G. Cheung, A. Versluis, C. Lee, S. Kwak, and H. Kim, “Screw-In Tendency of Rotary Nickel-Titanium Files Due to Design Geometry,” *International Endodontic Journal*, vol. 48, no. 7, pp. 666–672, 2015.

35. L. Wang, R. Lin, H. Chen, Z. Li, F. R. Tay, and L. Gu, “Influence of the Number of Pecking Motions at Working Length on the Shaping Ability of Single-File Systems in Long Oval-Shaped Curved Canals,” *Journal of Endodontics*, vol. 48, no. 4, pp. 548–554, 2022.

36. G. Gambarini, “Rationale for the Use of Low-Torque Endodontic Motors in Root Canal Instrumentation,” *Dental Traumatology: Review Article*, vol. 16, no. 3, pp. 95–100, 2000.

37. D. Fife, G. Gambarini, and L. Britto, “Cyclic Fatigue Testing of ProTaper NiTi Rotary Instruments After Clinical Use,” *Oral Surgery, Oral Medicine, Oral Pathology, Oral Radiology, and Endodontology*, vol. 97, no. 2, pp. 251–256, 2004.

38. S. J. Whipple, T. C. Kirkpatrick, and R. E. Rutledge, “Cyclic Fatigue Resistance of Two Variable-Taper Rotary File Systems: ProTaper Universal and V-Taper,” *Journal of Endodontics*, vol. 35, no. 4, pp. 555–558, 2009.

39. G. R. M. La Rosa, V. Shumakova, G. Isola, F. Indelicato, C. Bugea, and E. Pedullà,

"Evaluation of the Cyclic Fatigue of Two Single Files at Body and Room Temperature With Different Radii of Curvature," *Materials*, vol. 14, no. 9, p. 2256, 2021.

40. G. Gambarini, "Cyclic Fatigue of Nickel-Titanium Rotary Instruments After Clinical Use with Low-and High-Torque Endodontic Motors," *Journal of Endodontics*, vol. 27, no. 12, pp. 772–774, 2001.

41. C. Peng, W. Hui, L. Wang, H. Xin, S. Deng, C. Li, and L. Zhang, "Cyclic Fatigue Resistance of Two Nickel-Titanium Instruments in Different Curving Angles: A Comparative Study," *Brazilian Oral Research*, vol. 29, pp. 1–7, 2015.

42. O. A. Peters, P. Y.-H. Chien, K. Armitt, J. C. Macorra, and A. Arias, "Testing Cyclic Fatigue Resistance of Nickel Titanium Rotary Endodontic Instruments: A Validation Study for a Minimum Quality Criterion in a Standardized Environment," *Frontiers in Dental Medicine*, vol. 2, p. 744809, 2021.

43. F. Auricchio and R. L. Taylor, "Shape-Memory Alloys: Modelling and Numerical Simulations of the Finite-Strain Superelastic Behavior," *Computer Methods in Applied Mechanics and Engineering*, vol. 143, no. 1-2, pp. 175–194, 1997.

44. F. Auricchio, R. L. Taylor, J. Lubliner *et al.*, "Shape-Memory Alloys: Macromodelling and Numerical Simulations of the Superelastic Behavior," *Computer methods in applied mechanics and engineering*, vol. 146, no. 3-4, pp. 281–312, 1997.

45. *ABAQUS/Standard User's Manual*, Dassault Systèmes Simulia Corp, United States, 2021.

46. R. Brodie, "Characterization of Superelastic Nitinol Wire for Application to Aortic Stent Graft Design," Ph.D. dissertation, 2018.

47. Micro-Photonics, "NRecon Reconstruction Software," https://www. microphotonics.com, accessed on June 15, 2021.

48. X. Gu, Y. Cao, J. Zhu, J. Wang, W. Zhang, and Z. Moumni, "Shape Optimization of SMA Structures with Respect to Fatigue," *Materials & Design*, vol. 189, p. 108456, 2020.

49. S. Seyedkavoosi and I. Sevostianov, "Micromechanics of Dentin," *Reviews on Advanced Materials and Technologies*, vol. 1, no. 1, pp. 1–26, 2019.

50. K. J. Chun, H. Choi, and J.-Y. Lee, "Comparison of Mechanical Property and Role Between Enamel and Dentin in the Human Teeth," *Journal of Dental Biomechanics*, vol. 5, no. 6, pp. 1–5, 2014.

51. C.-F. Han, B.-H. Wu, C.-J. Chung, S.-F. Chuang, W.-L. Li, and J.-F. Lin, "Stress-Strain Analysis for Evaluating the Effect of the Orientation of Dentin Tubules on their Mechanical Properties and Deformation Behavior," *Journal of the Mechanical Behavior of Biomedical Materials*, vol. 12, pp. 1–8, 2012.

52. B. Rundquist and A. Versluis, "How Does Canal Taper Affect Root Stresses?" *International Endodontic Journal*, vol. 39, no. 3, pp. 226–237, 2006.

53. I. Ichim, D. Kuzmanovic, and R. Love, "A Finite Element Analysis of Ferrule Design on Restoration Resistance and Distribution of Stress within a Root," *International Endodontic Journal*, vol. 39, no. 6, pp. 443–452, 2006.

54. R. Cheng, X.-D. Zhou, Z. Liu, H. Yang, Q.-H. Gao, and T. Hu, "Finite Element Analysis of the Effects of Three Preparation Techniques on Stresses within Roots Having Curved Canals," *International Endodontic Journal*, vol. 42, no. 3, pp. 220–226, 2009.

55. R. Cheng, X.-D. Zhou, Z. Liu, and T. Hu, "Development of a Finite Element Analysis Model with Curved Canal and Stress Analysis," *Journal of Endodontics*, vol. 33, no. 6, pp. 727–731, 2007.

56. L. W. Boushell and J. R. Sturdevant, "Clinical Significance of Dental Anatomy,

Histology, Physiology, and Occlusion," *Sturdevant's Art & Science of Operative Dentistry,*, pp. 1–40, 2019.

57. Y. Delin, N. Haiying, G. Yikang, and C. Xing, "Elastic Modulus of Human Cementum," *Applied Mathematics and Mechanics*, vol. 20, pp. 1134–1141, 1999.

58. S. P. Ho, P. Senkyrikova, G. W. Marshall, W. Yun, Y. Wang, K. Karan, C. Li, and S. J. Marshall, "Structure, Chemical Composition and Mechanical Properties of Coronal Cementum in Human Deciduous Molars," *Dental Materials*, vol. 25, no. 10, pp. 1195–1204, 2009.

59. P. Kamposiora, G. Papavasilious, S. C. Bayne, and D. A. Felton, "Finite Element Analysis Estimates of Cement Microfracture Under Complete Veneer Crowns," *The Journal of Prosthetic Dentistry*, vol. 71, no. 5, pp. 435–441, 1994.

60. A. N. Natali, E. L. Carniel, P. G. Pavan, F. G. Sander, C. Dorow, and M. Geiger, "A Visco-Hyperelastic-Damage Constitutive Model for the Analysis of the Biomechanical Response of the Periodontal Ligament," *Journal of Biomechanical Engineering*, vol. 130, no. 3, p. 031004, 2008.

61. M. Pini, H. Wiskott, S. Scherrer, J. Botsis, and U. Belser, "Mechanical Characterization of Bovine Periodontal Ligament," *Journal of Periodontal Research*, vol. 37, no. 4, pp. 237–244, 2002.

62. A. N. Natali, *Dental Biomechanics*, First Edition, CRC Press, Florida, 2003.

63. A. Fedorov, R. Beichel, J. Kalpathy-Cramer, J. Finet, J.-C. Fillion-Robin, S. Pujol, C. Bauer, D. Jennings, F. Fennessy, M. Sonka *et al.*, "3D Slicer as an Image Computing Platform for the Quantitative Imaging Network," *Magnetic Resonance Imaging*, vol. 30, no. 9, pp. 1323–1341, 2012.

64. AutoDesk, "Fusion 360," https://www.autodesk.com/products/fusion360/overview, accessed on June 15, 2021.

65. J. Martos, G. H. Tatsch, A. C. Tatsch, L. F. M. Silveira, and C. M. Ferrer-Luque, "Anatomical Evaluation of the Root Canal Diameter and Root Thickness on the Apical Third of Mesial Roots of Molars," *Anatomical Science International*, vol. 86, pp. 146–150, 2011.

66. S. Razumova, A. Brago, A. Howijieh, H. Barakat, A. Manvelyan, and Y. Kozlova, "An in Vitro Evaluation Study of the Geometric Changes of Root Canal Preparation and the Quality of Endodontic Treatment," *International Journal of Dentistry*, vol. 2020, no. 1, p. 8883704, 2020.

67. I. Štamfelj, G. Vidmar, E. Cvetko, and D. Gašperšič, "Cementum Thickness in Multirooted Human Molars: A Histometric Study by Light Microscopy," *Annals of Anatomy-Anatomischer Anzeiger*, vol. 190, no. 2, pp. 129–139, 2008.

68. M. Gupta, K. Madhok, R. Kulshrestha, S. Chain, H. Kaur, and A. Yadav, "Determination of Stress Distribution on Periodontal Ligament and Alveolar Bone by Various Tooth Movements - A 3D FEM study," *Journal of Oral Biology and Craniofacial Research*, vol. 10, no. 4, pp. 758–763, 2020.

69. A. M. Figueiredo, P. Modenesi, and V. Buono, "Low-Cycle Fatigue Life of Superelastic NiTi Wires," *International Journal of Fatigue*, vol. 31, no. 4, pp. 751–758, 2009.

70. A. Runciman, D. Xu, A. R. Pelton, and R. O. Ritchie, "An Equivalent Strain/Coffin-Manson Approach to Multiaxial Fatigue and Life Prediction in Superelastic Nitinol Medical Devices," *Biomaterials*, vol. 32, no. 22, pp. 4987–4993, 2011.

71. Z. Moumni, A. Van Herpen, and P. Riberty, "Fatigue Analysis of Shape Memory Alloys: Energy Approach," *Smart Materials and Structures*, vol. 14, no. 5, p. S287, 2005.

72. Z. Moumni, C. Morin, and W. Zaki, "Cyclic Behaviour and Fatigue Design of Shape Memory Alloy Devices," in *Proceedings of the SMST*, California, USA, 2010.

73. C. J. Ruddle, "Finishing the Apical One Third: Endodontic Considerations," *Dentistry Today*, vol. 21, no. 5, pp. 66–73, 2002.

APPENDIX A: PERMISSIONS

The images included in this dissertation without references in their captions were created by myself as part of this research. For images I created that were used in published articles during this research, the journals allow authors to reuse them without permission. In the official web page of Australian Endodontic Journal, it is explicitly stated as "If you wish to reuse your own article in a new publication of which you are the author, editor or co-editor, prior permission is not required". The Applied Sciences journal is open access and permits everyone to use the materials published in it, as explicitly stated by the journal, "All articles published by MDPI are made immediately available worldwide under an open access license. No special permission is required to reuse all or part of the article published by MDPI, including figures and tables. For articles published under an open access Creative Common CC BY license, any part of the article may be reused without permission provided that the original article is clearly cited.". Consequently, the images generated during this thesis study and whose copyrights have been transferred to the publisher have been used in the dissertation in accordance with the 'publication policy regarding the reuse of the author's own writings and graphics' available on the publisher's page. For republished materials from other publications referenced in this work, citations are provided in the captions, and permissions for their reuse are documented in this section.